STOCHASTIC GEOMETRY-BASED PERFORMANCE ANALYSIS OF IRS-AIDED MMWAVE NETWORKS

IRS-DESTEKLİ MİLİMETRE DALGA AĞLARININ STOKASTİK GEOMETRİ-TABANLI PERFORMANS ANALİZİ

ABDULLAH YASİN ETCİBAŞI

PROF. DR. EMRE AKTAŞ

Supervisor

Submitted to

Graduate School of Science and Engineering of Hacettepe University

as a Partial Fulfillment to the Requirements

for the Award of the Degree of Master of Science

in Electrical and Electronics Engineering

June 2022

ABSTRACT

STOCHASTIC GEOMETRY-BASED PERFORMANCE ANALYSIS OF IRS-AIDED MMWAVE NETWORKS

Abdullah Yasin Etcibaşı

Master of Science, Electrical and Electronics Engineering

Supervisor: Prof. Dr. Emre Aktaş

June 2022, 96 pages

Wireless communication society aims for higher frequency bands for the unused bandwidths. However higher frequency comes with its drawbacks such as the high penetration loss. The concept of intelligent reflecting surfaces (IRSs) has recently become a popular topic for various use cases including coverage enhancement. Through reflecting signals in the desired and programmed direction, coverage holes may be eliminated. In previous works, coverage analysis of IRS-aided networks was done for several different channel and system model assumptions. However, most of the works do not address the blockage effect, and those that address use an unpractical path loss (PL) model for the indirect link which is the sum-distance PL model. It is envisioned that the primary benefit of IRS would be to aid mmWave communication in the presence of blockages. In this thesis, we consider a stochastic geometry (SG)-based network to model the locations of two-dimensional blockages (typically buildings), base stations (BSs), and IRSs. We also consider the the product-distance PL model, which is a more suitable PL model for the far-field as opposed to the commonly used sum-distance model. First, we propose a gamma approximation for the nearest distance distributions and derive a closed-form expression for the distribution of the product-distance of the indirect link. We investigate the coverage probability for the line-of-sight (LoS) dependent network. In the numerical results, we compare our proposed analytical approximations with simulations. We also investigate the coverage gains of

IRS-aided systems. We observed that up to a 45% boost in the coverage probability can be obtained with the use of the IRS.

Keywords: Millimeter-wave (mmWave), Intelligent Reflecting Surface (IRS), signal-to-noise ratio (SNR), coverage, stochastic geometry (SG)

ÖZET

IRS-DESTEKLİ MİLİMETRE DALGA AĞLARININ STOKASTİK GEOMETRİ-TABANLI PERFORMANS ANALİZİ

Abdullah Yasin Etcibaşı

Yüksek Lisans, Elektrik-Elektronik Mühendisliği

Danışman: Prof. Dr. Emre Aktaş

Haziran 2022, 96 sayfa

Kablosuz iletişim topluluğu, kullanılmayan bant genişlikleri için daha yüksek frekans bantları hedeflemektedir. Bununla birlikte, daha yüksek frekans, yüksek penetrasyon kayıpları gibi dezavantajları beraberinde getirir. Akıllı yansıtıcı yüzeyler (IRS'ler) kavramı, son zamanlarda kapsama alanı geliştirme dahil olmak üzere çeşitli kullanım durumları için popüler bir konu haline gelmiştir. Sinyalleri istenilen ve programlanan yönde yansıtarak kapsama alanı boşlukları ortadan kaldırılabilir. Literatürdeki önceki çalışmalarda farklı sistem ve kanal modelleri için IRS destekli ağların kapsama analizi yapılmıştır. Ne var ki, çalışmaların çoğu blokaj etkisine değinmemektedir ve değinenler de IRS'ler için pratik olmayan bir yol kaybı (PL) modeli olan toplam mesafeli PL modelini kullanmışlardır. IRS'nin birincil yararının, engellerin varlığında mmwave iletişimine yardımcı olacağı öngörülmektedir. Bu tezde, iki boyutlu blokajların (tipik olarak binalar), baz istasyonlarının (BS) ve IRS'lerin konumlarını modellemek için stokastik geometri (SG) tabanlı bir ağı ele alıyoruz. Ayrıca uzak-alan durumları için daha uygun olan PL modelini (çarpım-mesafesi PL modeli) ele alacağız. İlk olarak, en yakın mesafe dağılımları için bir gamma yaklaşımı önereceğiz ve endirekt bağlantının çarpım mesafesi dağılımı için de bir kapalı-form ifade türeteceğiz. LoS bağımlı ağ için kapsama alanı olasılığını inceleyeceğiz. Simülasyon sonuçlarında ise, önerilen analitik yaklaşımlarımızı simülasyonlarla karşılaştırdık. Ayrıca

IRS destekli sistemlerin kapsama kazanımlarını da araştırdık. Sonuç olarak ise IRS'nin kullanılmasıyla birlikte kapsama alanı olasılığında %45'e varan bir artış elde edilebileceğini gözlemledik.

Keywords: Milimetre-dalge (mmWave), Akıllı Yansıtıcı Yüzeyler (IRS), sinyal-gürültü oranı (SNR), kapsama alanı, stokastik geometri (SG)

ACKNOWLEDGEMENTS

This study has been supported by TÜRK TELEKOM within the framework of 5G and Beyond Joint Graduate Support Programme coordinated by Information and Communication Technologies Authority.

I would like to express my special thanks of gratitude to my advisor, Prof. Dr. Emre Aktaş, who always stood by me and guided me during my master's degree journey. I also would like to thank to my family, especially my father, Turgay Etcibaşı, for their special support.

Last but not least, I would like to express my sincere gratitude to all who make this 5G and Beyond Joint Graduate Support Programme happen in the Information and Communication Technologies Authority (BTK) and Türk Telekom for providing me this incredible opportunity of research.

Abdullah Yasin Etcibaşı
June 2022, Ankara

CONTENTS

Page

ABSTRACT i
ÖZET iii
ACKNOWLEDGEMENTS v
CONTENTS vi
TABLES vii
FIGURES viii
ABBREVIATIONS xi
1. INTRODUCTION 1
1.1. Scope Of The Thesis 2
1.2. Contributions 2
1.3. Organization 3
2. BACKGROUND 4
2.1. Propagation in MmWave Systems 4
2.2. Intelligent Reflecting Surfaces (IRSs) 9
2.3. Preliminaries On SG 16
3. RELATED WORKS 22
4. COVERAGE ANALYSIS 23
4.1. System Model 24
4.2. Method 27
4.2.1. Distributions of the Distances 29
4.2.2. Gamma Approximation of The Nearest-LoS Neighbor Distance Distributions 31
4.2.3. Feasible BSs 40
4.2.4. Indirect LoS link's Product-Distance Distribution 44
4.2.5. Conditional Distribution of Nearest Distances 47
4.2.6. Conditional SNR Coverage Probabilities 55
5. NUMERICAL RESULTS 59
6. CONCLUSION 71

TABLES

Page

Table 2.1 Penetration losses for different building materials at 28 GHz [1]..... 5

Table 5.1 Simulation parameters 60

FIGURES

Page

Figure 2.1 UMi 142 GHz directional PL scatter plot and fitted PL models [2]. Red crosses and the magenta circles represent the LoS and NLoS measurements, respectively. The blue diamonds represent the maximum measured power for each location. The black dotted lines are the free-space PL model for the given PLEs. The solid lines are the best-fit outdoor directional CI PL models for both LoS and NLoS scenarios. 6

Figure 2.2 (a) Spatial consistency measurement locations. (b) 142 GHz PL variations over 34 RX locations. 6

Figure 2.3 (a) Foliage penetration loss vs. frequency. (b) Rain attenuation loss vs. frequency [3]..... 7

Figure 2.4 (a) System model of 256x32 large scale antenna system. (b) Measurement configurations. (c) The receiver model [4]. 8

Figure 2.5 Specific absorption rates of 4G and 5G antenna systems [4]..... 8

Figure 2.6 Physical architecture of an IRS [5]. 10

Figure 2.7 Electromagnetic functions of IRS [6]. 11

Figure 2.8 Network functions of IRS [7]. 12

Figure 2.9 (a) RE design using PIN diode at 60 GHz [8]. (b) at 11 GHz [9]..... 13

Figure 2.10 RE design using varactor diodes at 5.8 GHz. (a) Perspective view. (b) Top view. (c) Side view [10]. 13

Figure 2.11 RE design using biased diode at 8.6 GHz. (a) Perspective view. (b) Phase response [11]. 14

Figure 2.12 Fabricated IRS at 60 GHz [8]. 14

Figure 2.13 Fabricated IRS at 11 GHz. (a) Proposed IRS constructed by 5 identical sub-IRSs. (b) FPGA control board and sub-IRSs. (c) Local zoom of front face of the sub-IRS. (d) Back face of the IRS. (e),(f) Measurement setup [9]. 15

Figure 2.14 Measurement results of beamforming performance of IRS at 11 GHz for the functions. (a) Broad beam. (b) Cosecant shaped beam. (c) Triple-beam [9]. 15
Figure 2.15 Fabricated IRS at 5.8 GHz [10]. 16
Figure 2.16 Outdoor measurements for the IRS at 5.8 GHz [10]. 17
Figure 2.17 Random network model with PPP distributed BSs and their Voronoi tessellations [12]. 18
Figure 2.18 Real BS deployment in a relatively flat area and their Voronoi tessellations [12]. 18
Figure 2.19 Tendency toward regularity or clustering of PPs [13]. 20
Figure 4.1 UE Association. 25
Figure 4.2 Maclaurin expansion, eqn.(22). 33
Figure 4.3 Kullback–Leibler divergence of (12) and (18) with (25). 37
Figure 4.4 Kullback–Leibler divergence of (13) and (18) with (26). 37
Figure 4.5 Kullback–Leibler divergence of (14) and (18) with (27). 38
Figure 4.6 PDFs of (12) and (18) with (25) for ρ=1. 38
Figure 4.7 PDFs of (13) and (18) with (26) for $\mu = 0.89$ and $\rho = 0.7$. 39
Figure 4.8 PDFs of (14) and (18) with (27) for $\mu = 0.3$ and $\rho = 0.98$. 39
Figure 4.9 Comparing the performance of the LoS ball approximation [14] with our model. 40
Figure 4.10 Auxiliary figures for the analysis of feasible BSs: (a) The map, the circle which the TUE is located, and 8 different regions which the TUE and BSs can be located. (b) Angle of the regions and related arc lengths. (c) The angle φ_1 for the region 1. (d) The angle φ_2 for the region 3. 41
Figure 4.11 Comparison of (17) and (45) for $\mu = 0.3$ and $\rho = 0.26$. 48
Figure 5.1 Null probabilities for (a) UE-BS link, (b) Indirect link, (c) Joint UE-BS and Indirect link. 61
Figure 5.2 Performance of the simulation with λ_{BS} = 7/km^2, ρ = 0.26, μ = 0.2, and $L_I = 1\ m$. 62
Figure 5.3 All components of the coverage for λ_{BS} = 7/km^2, ρ = 0.26 μ = 0.2, and $L_I = 1\ m$. 62

Figure 5.4 The difference between the values of coverage probabilities with and without IRS at $SNR = 0\ dB$ for $L_I = 1\ m$, varying ρ, μ, and (a) λ_{BS} = 3/km^2, (b) λ_{BS} = 7/km^2, (c) λ_{BS} = 11/km^2, (d) λ_{BS} = 15/km^2. . 63
Figure 5.5 The coverage probability for the parameters gives the maximum difference in Fig. 5.4 (c). 64
Figure 5.6 Coverage probabilities for various IRS lengths, λ_{BS} = 7/km^2, ρ = 0.35, and μ = 0.3..... 65
Figure 5.7 The ratio of the difference between coverage probabilities with and without IRS at $SNR = 0\ dB$ to the coverage probability without IRS at $SNR = 0\ dB$ for $L_I = 1\ m$, varying ρ, μ, and (a) λ_{BS} = 3/km^2, (b) λ_{BS} = 7/km^2, (c) λ_{BS} = 11/km^2, (d) λ_{BS} = 15/km^2..... 66
Figure 5.8 Coverage probabilities for various constant θ_i values, λ_{BS} = 7/km^2, ρ = 0.26, μ = 0.2, and $L_I = 1\ m$ 67
Figure 5.9 Sample coverage probabilities for different constant θ_i values showing the performance of coverage probabilities with fixed θ_i, best fit can be obtained with θ_i = 0.35π. 68
Figure 5.10 Comparing the model proposed in [15] and [16] (line Boolean scheme with sum-distance PL model for the indirect link) with the model proposed in this study (rectangular Boolean scheme with product-distance PL model)..... 69
Figure 5.11 Performance analysis of the proposed model with the random deployment of IRSs into the one facade of buildings (difference between the total probability and the probability of No IRS case at $SNR = 0\ dB$). 70
Figure 5.12 Performance analysis of the proposed model with the random deployment of IRSs into the one facade of buildings (ratio of the difference between the total probability and the probability of No IRS case to the CP without IRS at $SNR = 0\ dB$)..... 71

ABBREVIATIONS

AoA	:	**A**ngle-**o**f-**A**rrival
AS	:	**A**ngular **S**pread
BS	:	**B**ase **S**tation
CP	:	**C**overage **P**robability
DL	:	**D**own**L**ink
DS	:	**D**elay **S**pread
EHF	:	**E**xtremely **H**igh **F**requency
EM	:	**E**lectro**M**agnetic
FCC	:	**F**ederal **C**ommunications **C**ommission
HPPP	:	**H**omogeneous **P**oisson **P**oint **P**rocess
IPPP	:	**I**nhomogeneous **P**oisson **P**oint **P**rocess
IoT	:	**I**nternet-**o**f-**T**hings
IRS	:	**I**ntelligent **R**eclecting **S**urface
LoS	:	**L**ine-**o**f-**S**ight
mmWave	:	**m**illi**m**eter-**W**ave
MCS	:	**M**onte **C**arlo **S**imulation
MIMO	:	**M**ultiple **I**nput **M**ultiple **O**utput
MPC	:	**M**ulti**P**ath **C**omponent
NLoS	:	**N**on-**L**ine-**o**f-**S**igth
OAM	:	**O**rbital **A**ngular **M**omentum
OP	:	**O**utage **P**robability
PL	:	**P**ath **L**oss
PLE	:	**P**ath **L**oss **E**xponent
PP	:	**P**oint **P**rocess
RCM	:	**R**eflection **C**oefficient **M**atrix
RE	:	**R**eflecting **E**lement
Rx	:	**R**eceiver
RMS	:	**R**oot-**M**ean-**S**quare

SG	:	**S**tochastic **G**eometry
SHF	:	**S**uper **H**igh **F**requency
SINR	:	**S**ignal-to-**I**nterference and **N**oise **R**atio
SIR	:	**S**ignal-to-**I**nterference **R**atio
SNR	:	**S**ignal-to-**N**oise **R**atio
TUE	:	**T**ypical **U**ser **E**quipment
Tx	:	**T**ransmitter
UE	:	**U**ser **E**quipment
UMi	:	**U**rban **Mi**cro

1. INTRODUCTION

The need for higher data rates and connectivity grows each year. Especially in the period of the pandemic COVID-19, we want to be connected anywhere all the time. According to Ericsson's research, the mobile data traffic has increased 300 times in the last 11 years [17]. Smartphones contribute 97% of mobile data traffic in the world, and it is foreseen that the monthly global average usage per smartphone will reach 41 GB by the end of 2027. To meet this demand, we need more spectrum which is available at higher frequencies. In the SHF and EHF bands (the 3-30 GHz and 30-300 GHz range, respectively), there are approximately 252 GHz suitable for mobile broadband [3]. For instance, the FCC, an American independent agency that regulates the communication, already opened 21 GHz in the 95-300 GHz band for the research purposes [18].

Although we can use a large amount of bandwidth in the high-frequency bands, there is a price to pay, which is the high penetration loss. The building penetration loss can be as high as 40 dB for buildings with infrared reflecting (IRR) glass [19]. In [19], the authors mention that a person who blocks the LoS link can cause an attenuation of around 20 dB. They also point out that the outage probability (OP) can be higher at mmWave frequencies due to the various path loss exponents (PLEs) of different streets. In [3], the authors plot the foliage penetration loss and the rain attenuation versus frequency. We can observe that the losses become severe at higher frequencies due to the environmental effects. However, If the antenna aperture is kept constant, the antenna gain will be higher at higher frequencies [3], [19], [20]. Hence we can compensate for the high free-space PL by using a large number of antenna elements. It has been suggested that atmospheric attenuation will not contribute more than a few dB to the PL for the cell sizes around 200m [3], [19]. To test this statement, some studies conducted field measurements that aim to measure the maximum distance of LoS links at high frequency by using beamforming. In [21], the authors claim that they achieved 2.148 Gbps of throughput at 1.8 km and at 39 GHz of operating frequency when the user equipment (UE) is stationary. In [20], 1.7 km of a range is achieved at 39 GHz in the LoS scenario. However, they point out that there are some coverage holes in non-line-of-sight (NLoS) locations. Specifically, they say that a range of around 200 m is achieved in the NLoS case. Combating this problem, the IRSs has emerged as a possible solution in the last 4 years.

The programmable nature of IRSs allows us to create LoS links around the buildings, and it brings a new concept to the wireless context called the smart radio environment [22]. Also, the low cost, low energy consumption, and programmable nature of IRSs make them a candidate technology for enabling 6G [18], [23]. Researches foresee IRSs as a possible solution to coverage problems at high frequencies [24]. There have been some contributions to investigate the coverage probability for IRS-aided networks. However, these works consider sum-distance PL and the line Boolean model which is not practical as product-distance PL model and rectangular Boolean scheme.

1.1. Scope Of The Thesis

This thesis mainly focuses on the coverage probability analysis of an IRS-aided SG-based mmWave network. We follow an stochastic geometry (SG) based approach where the multiple BSs, blockages, IRSs, and UEs are distributed according to a homogeneous Poisson point process (HPPP). We assume that coverage is line of sight (LoS) only, as in [15], where fully LoS dependent coverage is considered.

1.2. Contributions

In this thesis, we analyze the coverage probability from a practical perspective. The main contributions of this study can be summarized as follows:

- Since the pdf of the nearest LoS neighbor distance in an SG-based network is cumbersome for analytical tractability, we purpose a gamma approximation to this pdf, which is more suitable for theoretical analyses.
- Unlike most of the previous works, we consider a much more realistic scenario where the PL model of the SNR expression of the indirect link is the product distance model. In addition, the blockages are model with a rectangular Boolean scheme, as opposed to previous works where line Boolean model were used.
- For the first time, we derive the pdf of the product of the distance between the typical UE (TUE) and nearest IRS, and the distance between nearest IRS and the nearest BS

relative to the IRS. We name this product as the *product distance*. Then we derive the probability of feasible BSs, which are the BSs that can be reached through the nearest IRS. Since, some of the BSs fall behind the buildings which are not reachable from the IRS.

- The analytical derivations of coverage probability are validated by the simulation results. The numerical results show that the coverage gains due to IRS depends on parameters such as blockage and BS density, IRS deployment ratio. It is shown that coverage probability gains of up to 45% are possible. There is an optimal IRS deployment ratio that gives maximum coverage for each BS density, and the effect of the IRS length into the network coverage is limited after 1.2m. Moreover, we show that the line Boolean sum-distance PL model is too optimistic for coverage analysis.

1.3. Organization

The organization of the thesis is as follows:

- Chapter 1 presents our motivation, contributions, and the scope of the thesis.
- Chapter 2 provides background information regarding the propagation characteristics of mmWave channels, IRSs, and stochastic geometry (SG). For the mmWave channel characteristics, we give some details about the penetration losses, path loss exponent, and spatial consistency in the mmWave. For the IRSs, we discuss the main network functions, building blocks, fundamental properties, and some implementations of IRSs. Then we give some preliminaries about the SG-based networks.
- Chapter 3 mentions the work that our study builds upon, and the works related to our system model.
- Chapter 4 introduces the method that we used to solve the SNR coverage probability problem, which includes the gamma approximation of nearest neighbor distances, pdf of the product distance, and the probability of feasible BSs.
- Chapter 5 demonstrates the numerical results of our solution and related Monte-Carlo simulations (MCSs) including the coverage plots for various densities of blockages

and BSs, the contribution of IRSs into the network coverage for different system parameters, investigation of the optimal length of the IRS, and the comparison of our model with the line Boolean sum-distance model.

- Chapter 6 states the summary of the thesis and possible future directions.

2. BACKGROUND

In this section, we will present the propagation characteristics of mmWave channels, the general properties of IRSs, and provide some SG preliminaries. The propagation characteristics of mmWave are examined in the sense that how the building materials affect the propagation, what is the effect of the foliage and atmospheric conditions, and what is the small scale model, angular spread, and correlation distance in mmWave channels. Then, we will give some implementations regarding the mmWave systems. Secondly, we will talk about the main functions of IRSs, use case scenarios, their working principle, and the experimental models. Finally, we will touch upon the fundamental theorems and definitions in SG based networks for our derivations given in Chapter 4.

2.1. Propagation in MmWave Systems

As we climb up in the frequency spectrum, we can find a vast amount of available bandwidth. In order to effectively utilize these large large frequency bands, we need to first know about the propagation characteristics in these frequencies. In order to investigate the theoretical gains, we need mathematical models of these channels. In this section, we will discuss the penetration losses of different materials, path loss exponent, spatial consistency, correlation distance, foliage losses, angle of arrivals - angle of departures, and small-scale fading in mmWave channels. Finally, we will give some experimental results of high-frequency systems, and briefly touch upon their health aspects.

One of the main properties of the mmWave is its high dependence on blockage. There is a sharp difference between LoS and NLoS scenarios. Especially in the NLoS case, the attenuation is much more severe than conventional frequencies. In [25], the authors mention that the building penetration loss can be as high as 40-80 dB so the outdoor-to-indoor

coverage may not be possible. Even the human body itself has an average penetration loss of 20 dB, especially in the direction of the head or torso [19], [25]. On the positive side, this loss applies to the interfering signals so that the interference will be limited in mmWave systems. The penetration loss of different building materials at 28 GHz can be seen in Table 2.1 [1]. It can be observed that the penetration losses of outdoor materials are markedly high so that they may not allow the waves to penetrate inside. However, on the indoor materials side, clear glass and drywall have acceptable penetration losses. Although the penetration losses are higher in the mmWave range than in the microwave, the PLE of LoS channels is the same. It is around 1.6 and 2.1 [19]. However, for the NLoS scenarios, the PLE is noticeably dependent on the environment. It ranges from 2.5 to 5. In Fig. 2.1, it can be observed that the LoS PLE fitted to the measurement points is approximately equal to two, and the variance of NLoS measurement data (red crosses) is quite high [2]. This high blockage-dependent nature of mmWave links makes the correlation distance low.

Environment	**Material**	**Thickness (cm)**	**Penetration Loss (dB)**
Outdoor	Tinted Glass	3.8	40.1
	Brick	185.4	28.3
Indoor	Clear Glass	$<$1.3	3.9
	Tinted Glass	$<$1.3	24.5
	Drywall	38.1	6.8

Table 2.1 Penetration losses for different building materials at 28 GHz [1]

In [26], authors investigated the spatial consistency at 140GHz. Spatial consistency is related to the spatial correlation of the channel. If two channel gains corresponding to locations separated by a distance d are highly correlated, then it is said that channel is spatial consistent for distance d. They form a rectangular route in which they conducted measurements in the intervals of 3 meters. The rectangular route they used and the receiver location indexes can be seen in Fig. 2.2 (a). The PL values for these measurement locations are given in the 2.2 (b). It can be observed from this plot that if an object intersects with the LoS link, there is a sharp increase in the PL value. Since the receiver locations RX6 and the RX22 are the LoS-NLoS crossing positions, there is a 33 dB and 13 dB instant variations in the PL value around RX6 and RX22. The major cause of these variations is the trees which can be seen

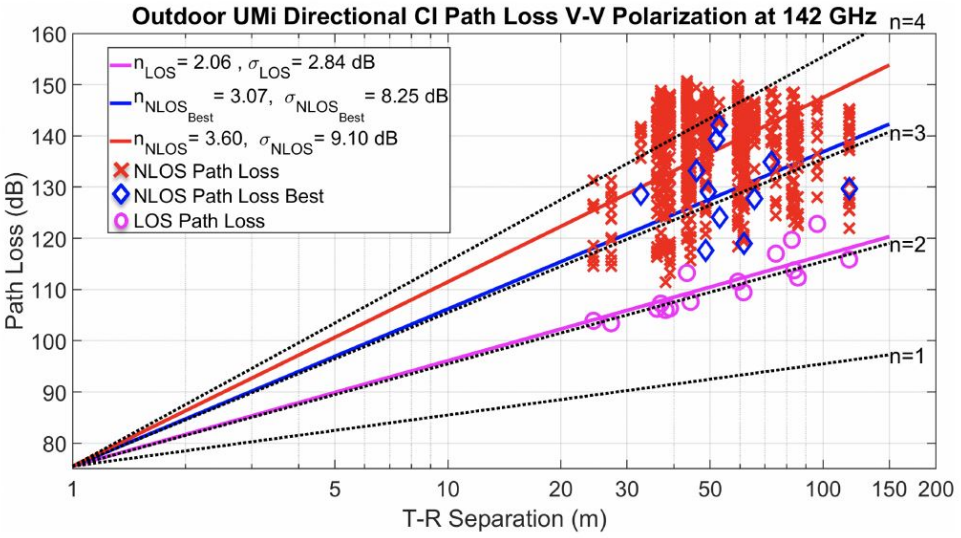

Figure 2.1 UMi 142 GHz directional PL scatter plot and fitted PL models [2]. Red crosses and the magenta circles represent the LoS and NLoS measurements, respectively. The blue diamonds represent the maximum measured power for each location. The black dotted lines are the free-space PL model for the given PLEs. The solid lines are the best-fit outdoor directional CI PL models for both LoS and NLoS scenarios.

in Fig.2.2 (a). The authors also show that the correlation distance is around 3.8 m in this experiment.

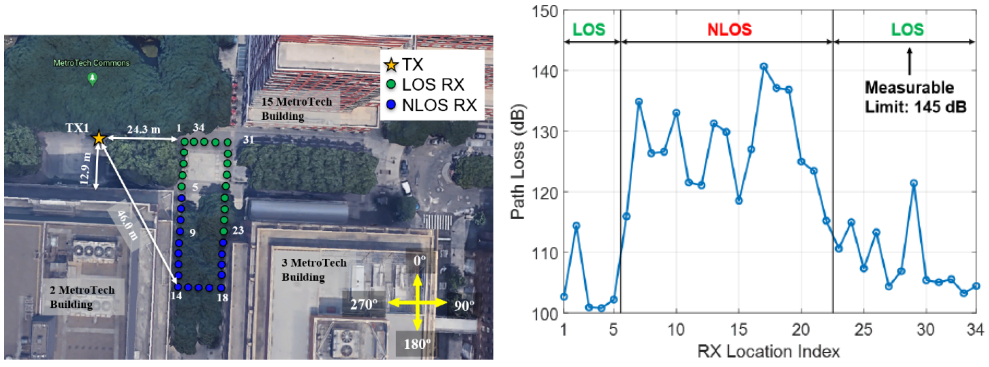

(a) (b)

Figure 2.2 (a) Spatial consistency measurement locations. (b) 142 GHz PL variations over 34 RX locations.

Another loss that we should consider in mmWave networks is the foliage loss. Although the attenuation increases with the foliage depth, it saturates for long distances [19]. The foliage attenuation for four different foliage depths versus frequency can be seen in the Fig. 2.3 (a) [3]. As we can observe, the attenuation increases by 10 dB, on average, as the depth increases at 60 GHz, and the difference becomes greater in the higher frequency bands. Also the rain

attenuation becomes severe in mmWave bands (Fig. 2.3 (b)). The reason for this increase in attenuation is that the wavelength is much smaller than the raindrops in these bands. Hence they scatter the radio signals [3]. If we back to the foliage loss, the PL of some streets can be different for different seasons, especially if they have deciduous trees (these trees shed their leaves every fall) [27]. The authors also mention that the leafy streets have an extra 23 dB of attenuation for above 200 meters of Rx-Tx distance.

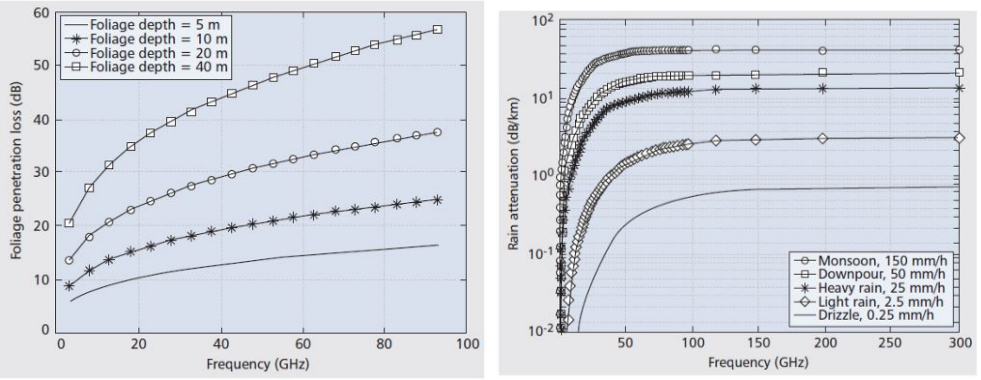

(a) (b)

Figure 2.3 (a) Foliage penetration loss vs. frequency. (b) Rain attenuation loss vs. frequency [3].

The mmWave bands are sparse in the angular domain, and the delay spread is much less than the microwave frequencies [25]. In [28], the root-mean-square (RMS) delay spread (DS) and angular spread (AS) are investigated for the frequencies of 28, 38, 73, and 142 GHz and they observed that the PLE is almost the same for all these frequencies but the DS and AS decreases as the frequency increases. For instance, if a threshold is set to the 20 dB below relative to the peak multipath component (MPC), the number of angle-of-arrivals (AoA) for the LoS case is 1.7 on average and it is 2.8 for the NLoS case at 142 GHz. As for the DS, the mean value of LoS DS is 1-2 ns from 28 to 142 GHz. It means that for the directional antennas pointing boresight direction, the only dominant path will be the LoS MPC [28]. Hence, we assumed that the only link can be made through the LoS MPC in a mmWave directional network as in our thesis because of the aforementioned reasons and the high penetration losses.

For the small-scale fading, there is not much measurement campaign done in the literature. In [29], authors use a linear track of 33λ length to get small-scale measurements with $\lambda/2$

(0.5 cm) steps at 28 GHz. They found out that the measurement results fit well for the Rician fading with 9 dB of K-factor.

Finally, we will discuss some prototypes and field measurements of mmWave systems. The antenna radiation pattern and the health aspects of large-scale mmWave 5G cellular systems are investigated in [4]. The system model of this study can be seen in Fig. 2.4 (a). The mobile phone is 6 meters away from the BS, and the downlink (DL) signal of 528 Mb/s data rate is sent at 28 GHz. The BS is equipped with 256 element antenna array with 24 dBi gain, and the Rx has a 16x2 antenna array with 10 dBi gain. According to their anechoic chamber measurements, the Rx has 12° of beamwidth and it has nearly a spherical coverage with two antenna sets. The authors also investigated the specific absorption rates of this system. In the mmWave bands, the electromagnetic (EM) absorption spreads to the entire human head but in the mmWave frequencies absorption is confined in the epidermis, see Fig. 2.5.

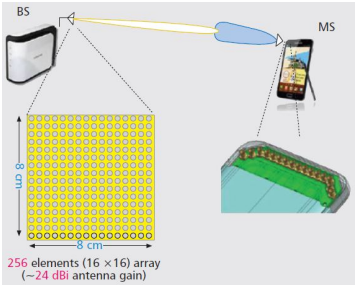

(a)

Carrier frequency	27.925 GHz
Bandwidth/duplexing	520 MHz / TDD
TX/RX configuration	TX: base station (BS) ant. RX: mesh-grid array (MS)
Channel coding	LDPC
Modulation	QPSK/16-QAM

(b)

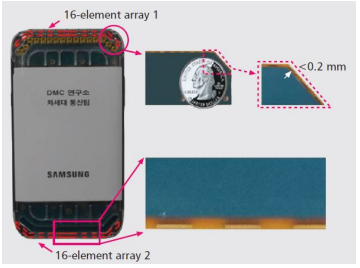

(c)

Figure 2.4 (a) System model of 256x32 large scale antenna system. (b) Measurement configurations. (c) The receiver model [4].

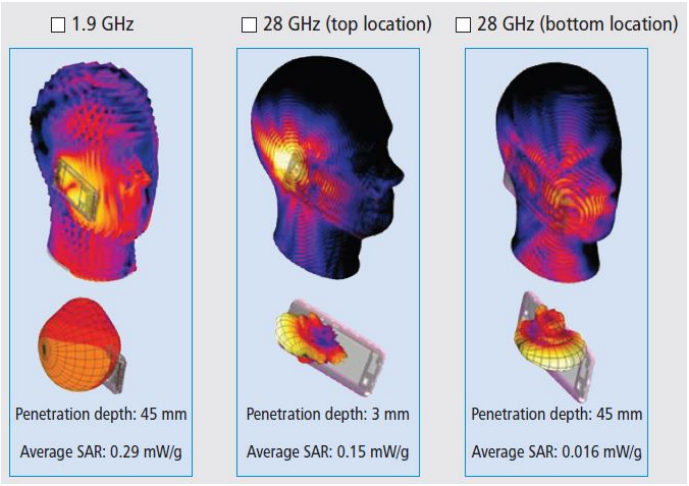

Figure 2.5 Specific absorption rates of 4G and 5G antenna systems [4].

In the link budget perspective, there is a detailed analysis in [3]. This analysis is for the carrier frequency of 28 and 72 GHz, distance of 1 and 0.5 km, and 1 GHz of bandwidth. They state that communication with a 2.77 Gbps data rate at 28 GHz and 1 km distance is possible. Authors in [20] design a 8x4 MIMO system at 28 GHz. The overall beamforming gain they got is 18 dBi, and 1.7 km of a range is reached in the LoS link. However, in the NLoS scenario, roughly 200 m of a range is measured and they point out that there are some coverage holes. Hence, IRSs can be a possible solution for this coverage problem in the mmWave networks.

2.2. Intelligent Reflecting Surfaces (IRSs)

IRSs are the surfaces that can manipulate the incoming wave for multiple use cases via its nearly passive reflecting elements (REs, or meta-atoms). The programmable nature of IRSs makes them an exciting concept in the wireless communication environment, and it is a relatively new area. In the literature, there are different names for IRSs including metasurfaces, metamaterials, large intelligent surfaces, and reflectarrays but the most well-known are IRSs and reconfigurable intelligent surfaces (RISs). Throughout this thesis, they will be named IRSs. The technology behind the IRS originated from the radar context. In the 2000s the core of this technology was created as metamaterials. These are called meta-materials because they are three-dimensional objects whose reflection characteristics are designed and fabricated with specific use cases. In other words, they were fixed (non-reconfigurable) and application-specific devices [30]. They were used mainly to decrease the radar cross-section. The real value of this technology for wireless communication networks was realized when they become electrically controllable. One of the earliest implementations of IRSs can be found in [8]. ın [8] a large intelligent surface with 160x160 elements at 60 GHz was designed. Another early study investigated their theoretical foundation in the reflection and refraction perspective in the well-known paper [31].

Wireless networks are evolving to a fully software-defined and agile to environmental changes. However, the channel itself is one of the biggest bottlenecks and fully uncontrollable and random phenomenon in wireless communication [30]. IRSs bring a new concept into the wireless environment called smart radio environment [22] which

can design the physical layer of the network in real-time. In the sequel, we will briefly discuss the different use cases and EM functions of IRSs, their internal structure, and several implementations.

The physical architecture of an IRS can be given as in Fig. 2.6 [5]. The internet-of-things (IoT) gateway is the interface of the IRS with the network. It can be called the controller in different works because it programs the reflection elements in real-time with the need of the network. The control layer is the configurable part of the IRS. This reconfigurable nature can be created with diodes, varactors, or embedded control agents called meta-atoms or REs. The size of these elements is important to reflect the EM wave in the desired direction and the desired way. Hence these elements generally have the size of $\lambda/10$ to $\lambda/5$ (we will give further details about these elements in the following parts). The switch configuration determines the EM function of IRS. Mathematically it is called the reflection coefficient matrix (RCM), and it is an N-dimensional diagonal matrix. An efficient and fast way to design this RCM is an open research problem, some studies can be found in [32], [33], [34], and [35]. In the end, with all these layers we can create a specific EM function on the surface of IRS.

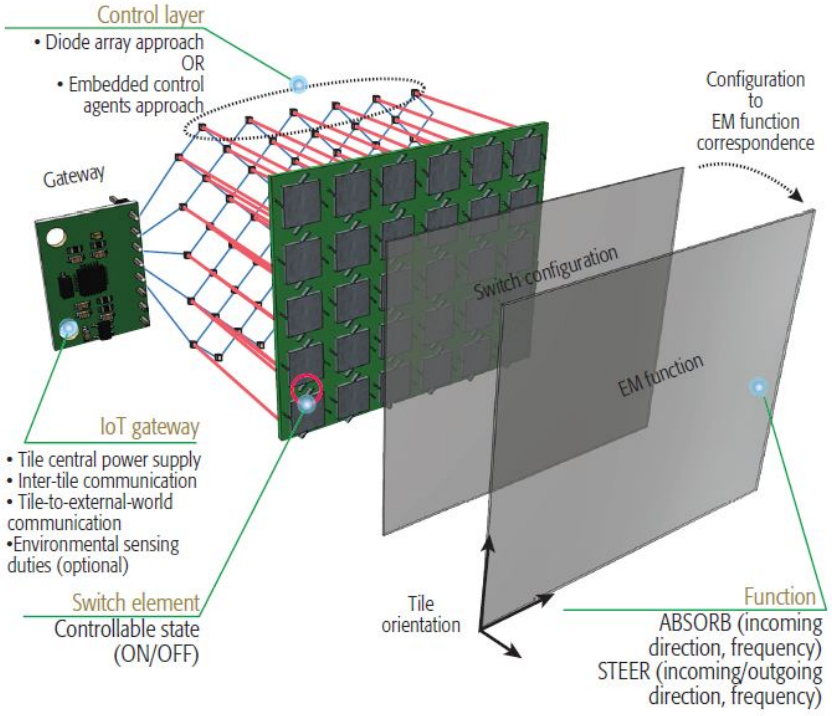

Figure 2.6 Physical architecture of an IRS [5].

Eight different EM functions can be created as shown in Fig. 2.7. The most common functions are reflection, focusing, and splitting. The specular reflection can only be created for the near-field scenarios because the IRS has a finite area. The splitting function can be used for spatial multiplexing, and the spectral efficiency can be increased via this function. The polarization control function can be used to adjust the phase of MPCs to increase the received power or it can be used for orbital angular momentum (OAM) modulation. Very high data rates and multiplexing gains can be obtained via OAM modulation (up to 2.5 Tb/s rate with 95.7 bps/Hz spectral efficiency [23], [36]). However, this concept is in its early phases and its communication range is quite limited. Analog processing can be used in backscattering communication. In the backscattering communication, a feeder creates an unmodulated signal and a backscatter device (in our case, it is the IRS) modulates the signal. This method relaxes the front-end and it can be advantageous for small IoT devices. Finally, the absorption function can be used for absorbing unwanted signals such as the one arriving at a malicious user.

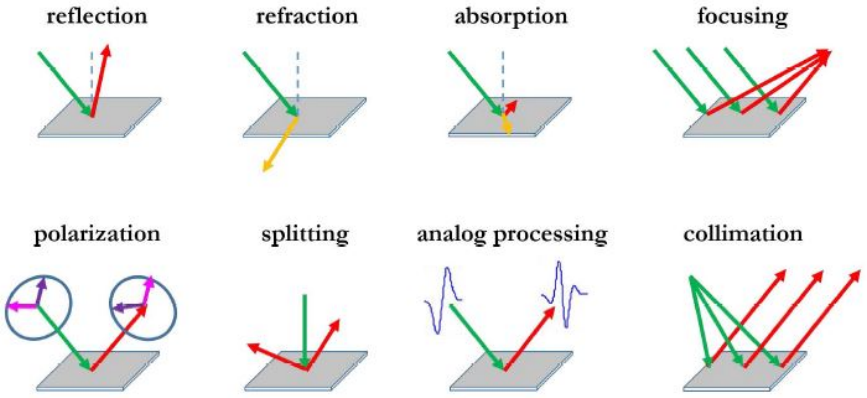

Figure 2.7 Electromagnetic functions of IRS [6].

IRSs can be used for various cases in the wireless networks. Some of the use cases can be found in the Fig. 2.8 [7]. In our study, we investigated the function given in the top-left corner of the figure which is creating an indirect path for users at the dead zone. The very first idea for the use case of IRSs comes to mind is the coverage enhancement function. In the literature, it is stated that the IRS increases the coverage but to the best of our knowledge, there is not any practical study that analyzes the coverage probability in the presence of IRSs. Studies about this problem consider unpractical assumptions such as sum distance PL or the line Boolean models for blockages. IRSs can also be used for physical layer security by

canceling the unwanted signal arriving at the eavesdropper, and massive device-to-device communication via creating extra paths between devices as given in the Fig. 2.8. More detailed information about IRS use scenarios can be found in [22].

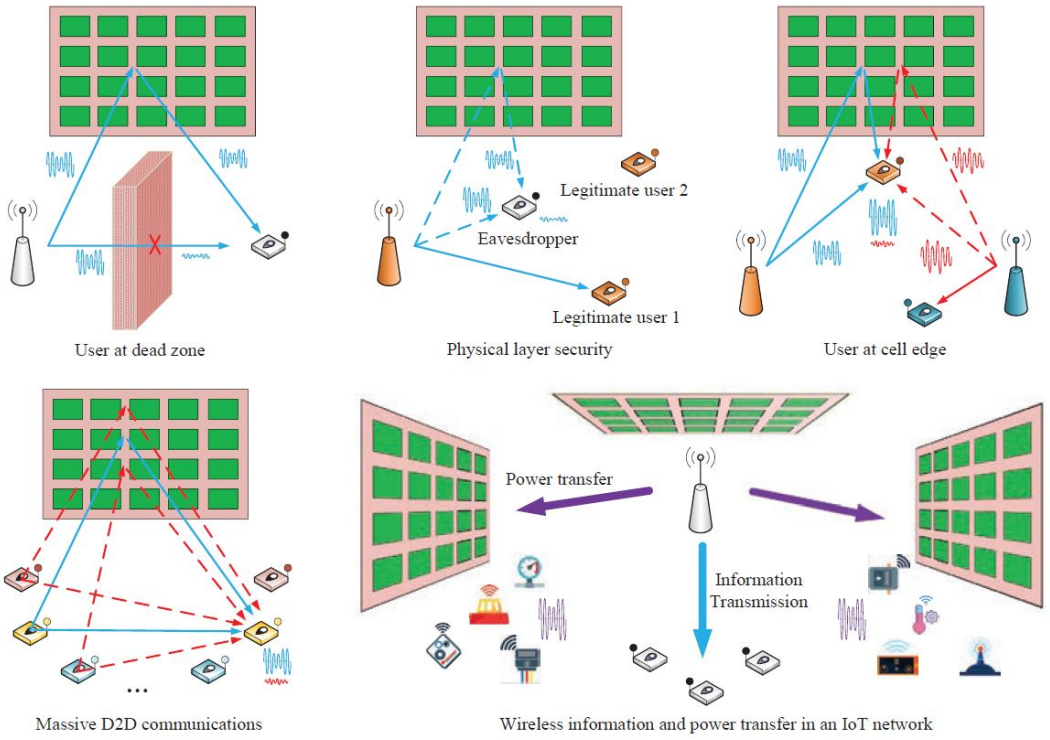

Figure 2.8 Network functions of IRS [7].

There are many ways to design the meta-atoms of IRSs. The most common method is to use pin diodes to control the different states of REs [8], [9]. In Fig. 2.9, meta-atom designs with pin diodes and their equivalent circuits can be seen. The Fig. 2.9 (a) represents the design at 60 GHz and the (b) shows the design at 11 GHz. One of the most advantageous properties of IRSs is that they can be manufactured by using simple electronic elements as shown in Fig. 2.9. Another example of RE design given in the Fig. 2.10 [10], where the authors used varactor diodes in their design at 5.8 GHz. Note that the operating frequency of each RE determines its size, and the phase response is set according to the frequency.

An example of a phase response of one RE given in the Fig. 2.11 (b) [11]. Since the authors aim for the 8.6 GHz of operating frequency, they designed a RE in a way that it gives $180°$ of phase difference at 8.6 GHz (red curve in Fig. 2.11 (b)). Since the RE is designed with a biased diode that has two states, the phase difference between the ON and OFF states have to be $180°$. Hence, we look for the phase difference of $180°$ in Fig. 2.11 (a). However, IRS

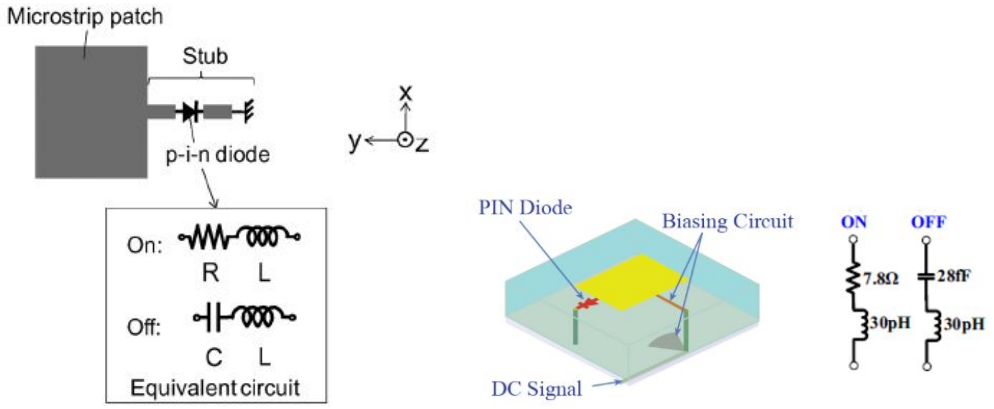

(a) (b)

Figure 2.9 (a) RE design using PIN diode at 60 GHz [8]. (b) at 11 GHz [9].

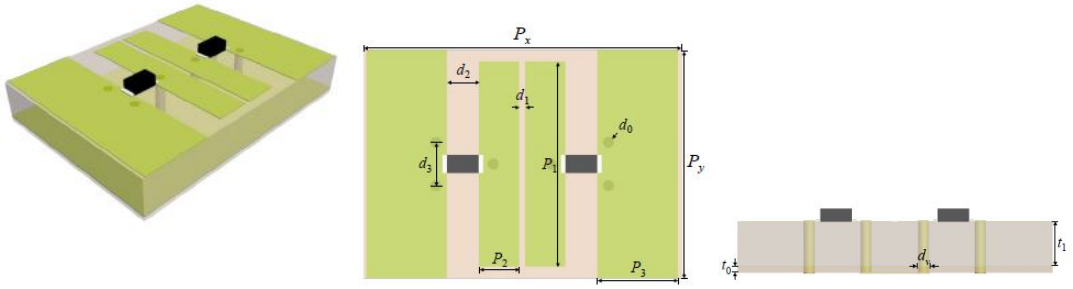

(a) (b) (c)

Figure 2.10 RE design using varactor diodes at 5.8 GHz. (a) Perspective view. (b) Top view. (c) Side view [10].

designs for large bandwidth applications is an open research problem, which is largely due to the fact that the phase response of a typical RE varies over. In [11], it was shown that the phase response can remain constant for only 0.6 GHz of bandwidth. a large bandwidth. It can be considered as constant just for 0.6 GHz of bandwidth. Now, let us have a look at some implementations and measurement results of IRSs.

In [8], the authors designed 160x160 IRS with 16 40x40 pieces. The total length of the IRS is 57.5 cm. In this thesis, we use this design as a reference for our RE size in the analytical calculations. The authors in [8] investigate the array gain and reflection pattern of IRS for 10 dBm peak power. The fabricated IRS and the system setup for measurement can be seen in Fig. 2.12. As a result, the antenna gain of the IRS in the far-field is 42 dBi, and the reflected beam has the 0.55° of beamwidth. In [11], authors claim that they represent the concept of coding metamaterials for the first time. Authors design a fixed metasurface to analyze the

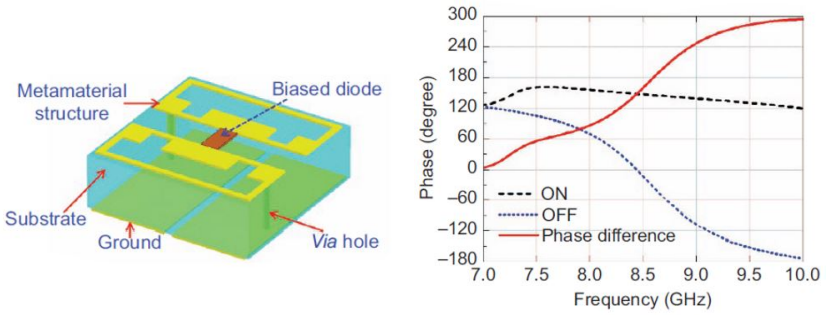

(a) (b)

Figure 2.11 RE design using biased diode at 8.6 GHz. (a) Perspective view. (b) Phase response [11].

different RCM configurations of the IRS with one-bit REs. The main function of this fixed IRS is to reduce the radar cross-section of an object by scattering the incoming wave equally. Then a programmable 30x30 metasurface at 8.6 GHz is designed. They simulated the design with four different RCM configurations which are beam splitting and beamforming.

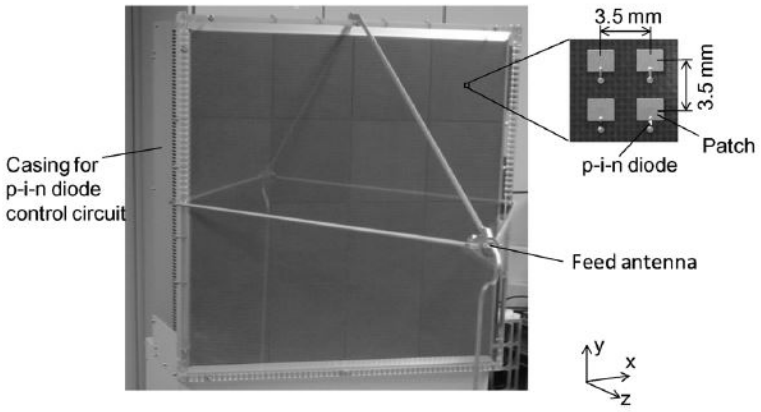

Figure 2.12 Fabricated IRS at 60 GHz [8].

A multiple function IRS is designed in [9]. Each unit cell (RE) has one-bit control via pin diodes and an FPGA is used for the controller. The authors proposed an RCM design algorithm and it is implemented as shown in the Fig. 2.13. The low-cost nature and scalability of IRSs can be observed from that figure. The authors bring 5 sub-surfaces to create one large IRS. The measurement results of this experiment are given in the Fig. 2.14 for three different functions including broad beam and beam splitting.

Although there are not many outdoor trials in the IRS literature, a 1100-element IRS operating at 5.8 GHz is given in [10]. The authors proposed an IRS configuration algorithm and designed 20x55 IRS including REs of 1-bit phase-shifting capability. The total size of

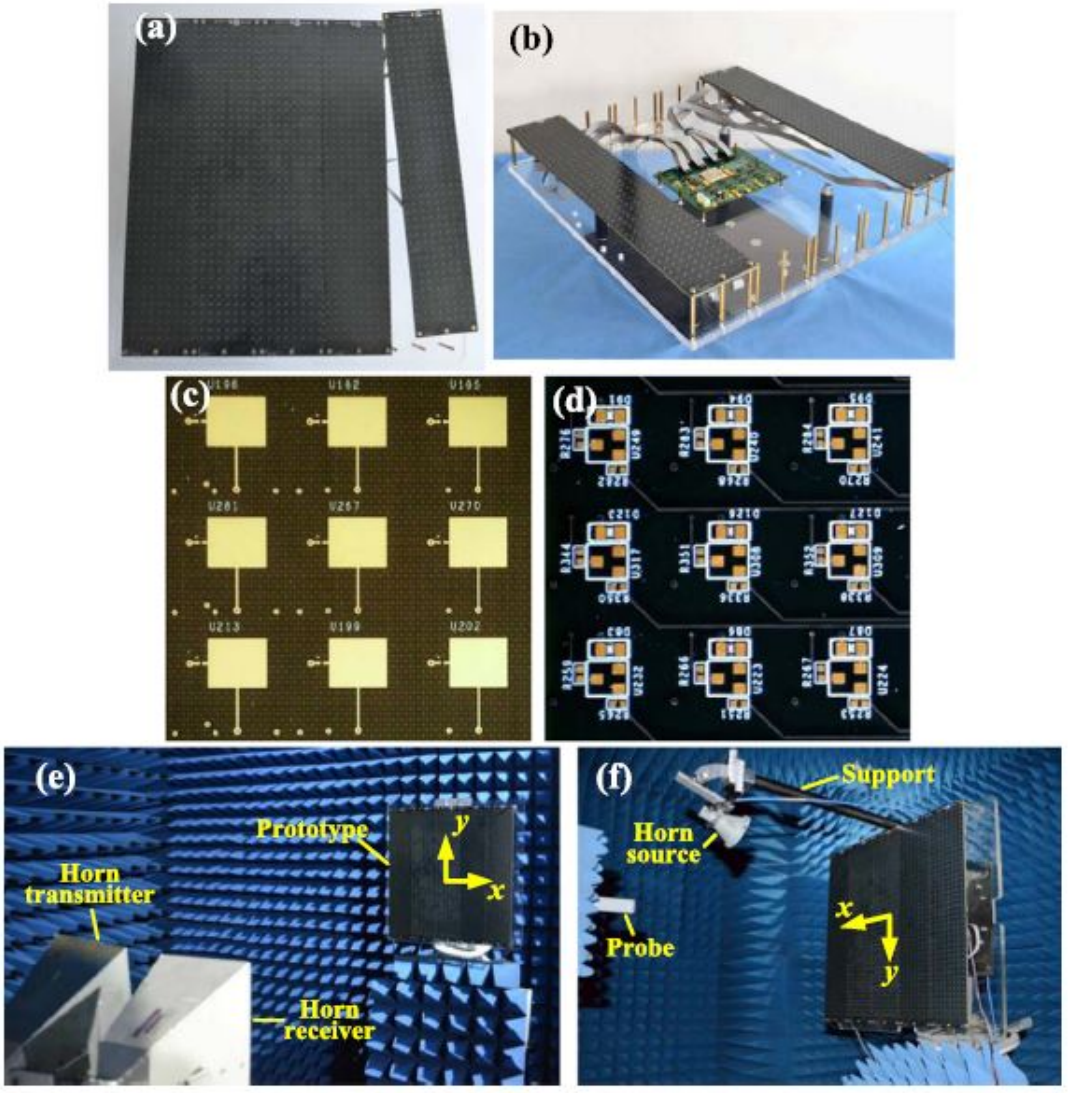

Figure 2.13 Fabricated IRS at 11 GHz. (a) Proposed IRS constructed by 5 identical sub-IRSs. (b) FPGA control board and sub-IRSs. (c) Local zoom of front face of the sub-IRS. (d) Back face of the IRS. (e),(f) Measurement setup [9].

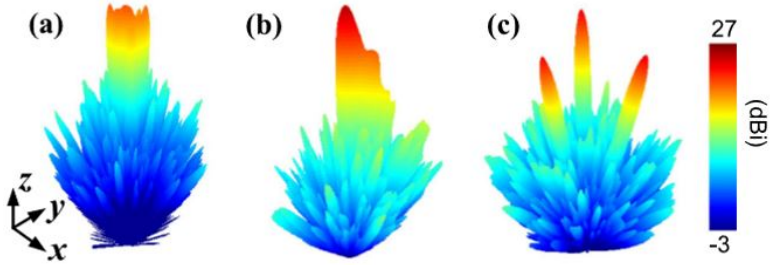

Figure 2.14 Measurement results of beamforming performance of IRS at 11 GHz for the functions. (a) Broad beam. (b) Cosecant shaped beam. (c) Triple-beam [9].

this design is 80x31 cm. They conducted both the indoor and outdoor measurements but we will discuss the outdoor trial only. The IRS is configured in a way that it reflects the incoming

signal to the 30° in azimuth direction. For the outdoor trial, they used to transmit power of 23 dBm to communicate for 500 meters, see Fig. 2.16. Compared to the case with a copper plate in place of the IRS, the IRS provided a 14 dB of gain. The authors state that because of the complexity of the channel (MPCs), IRS might become frequency-selective. If higher frequency bands had been used, higher gains might have been obtained, since the MPCs are much less in the higher frequency range.

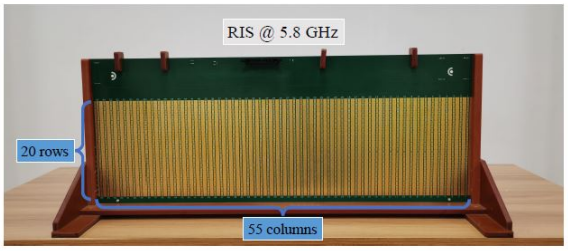

Figure 2.15 Fabricated IRS at 5.8 GHz [10].

In order to analyze the coverage of an IRS aided system, we need to model the PL of an IRS aided communication link. Authors in [37] investigated the PL model of IRSs experimentally. They demonstrate the difference in PL laws of IRS in the near-field and far-field scenarios. Specifically, while the sum-distance PL model is appropriate for the near-field case, the product-distance model is more suitable for the far-field scenario. Wu et al. also mention this point in their tutorial paper [38]. On the other hand, the N^2 gain in the link budget of the link through IRS is obtained in [39] experimentally. More detailed information about the PL model of IRSs given in the Section 4.1.

2.3. Preliminaries On SG

As we mentioned in the Section 2.1. the mmWave networks are highly dependent on the environment. Hence, we need the locations of Tx and Rx to fully evaluate the network performance [13]. SG-based models are a close fit to the practical network architecture and they can result in analytically tractable approaches. Throughout this study, we deal with point processes (PP), specifically we adopt Poisson point processes (PPP), which is the typical mathematical model considered in many SG based wireless network analyses.

Although the PPP does not match perfectly with the real-world scenarios, it is the most suitable PP because of its analytical tractability [13]. An example of a random network model

Figure 2.16 Outdoor measurements for the IRS at 5.8 GHz [10].

with PPP distributed BSs and their related cell boundaries forming a Voronoi tessellation can be seen in the Fig. 2.17 [12]. As we can observe from this figure, some of the BSs are quite close to each other but their cell size is relatively large. On the other hand, an example of a real 4G network BS deployment for in a 40x40 km^2 area and their Voronoi tessellations is given in the Fig. 2.18. As can be seen, cell boundaries are very similar for the random network and the real network. However, as we pointed out, some of the BSs

are somewhat close to each other. Hence, the PPP model creates a lower bound for network analysis [12]. We can form more accurate networks and get more accurate results with the other PP models but the analytical tractability undergoes a huge loss. In the sequel, we will discuss some fundamental concepts of the PP theory that plays a crucial role in SG (more detailed information can be found in [13]).

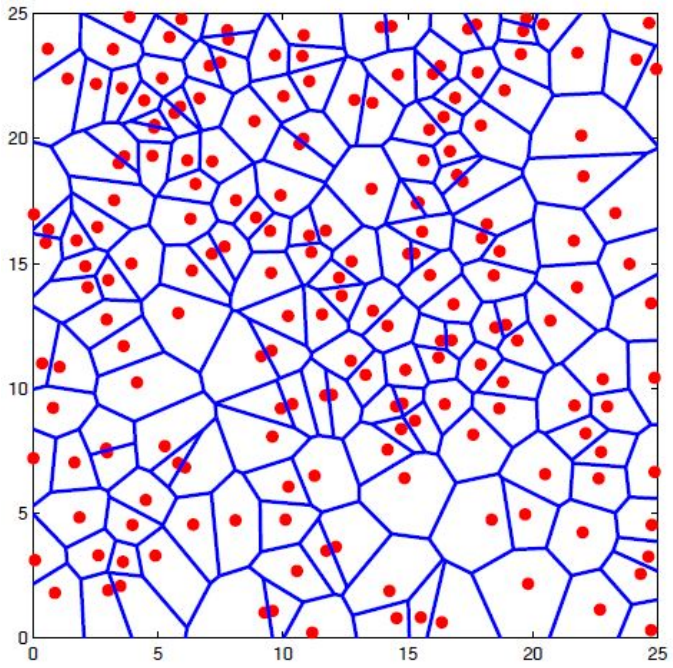

Figure 2.17 Random network model with PPP distributed BSs and their Voronoi tessellations [12].

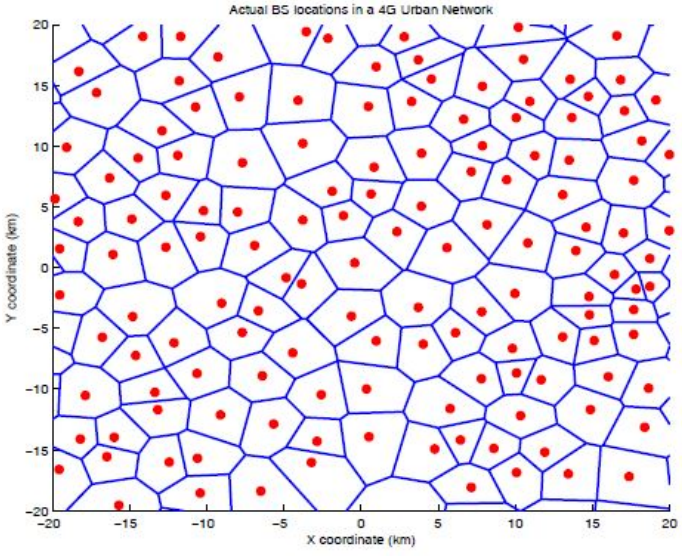

Figure 2.18 Real BS deployment in a relatively flat area and their Voronoi tessellations [12].

We can consider the spatial PPs as a cumulative counting process. Let's consider a spatial PP Ψ defined for a bounded set $B \subset \mathbb{R}^2$ as the number of points x_i falling into B [13] is given by

$$\Psi(B) = \sum_{x_i \in \Psi(B)} \mathbb{1}_B(x_i) \tag{1}$$

One of the most important metrics in PPs is the nearest neighbor distance and the contact distribution. To understand the nearest neighbor distance distribution, we need to know the null or the void probability. The probability that there will be exactly n number of points inside B is defined as $\mathbb{P}(N(B) = n)$. Hence, the void probability is defined as $void(B) = \mathbb{P}(N(B) = 0)$. If there is exactly one point inside a ball with center y and radius r (the point y itself), it means that the distance between y and the closest point of Ψ is greater than r. Therefore, we can find the nearest neighbor distance distribution $G_y(.)$ using the probability $\mathbb{P}(N(B) = 1)$ in the ball of radius r and centered at y ($b(y, r)$). $G_y(.)$ defined as the distribution of the distance between y and the nearest point of Ψ excluding y, $\Psi \backslash \{y\}$ [13], and can be given by

$$\begin{aligned} G_y(r) &= \mathbb{P}\left(d(y, \Psi \backslash \{y\}) \leq r | y \in \Psi\right) \\ &= \mathbb{P}\left(N\left(b(y, r) \backslash \{y\}\right) > 0 | y \in \Psi\right) \\ &= 1 - \mathbb{P}\left(N(b(y, r)) = 1 | y \in \Psi\right) \end{aligned} \tag{2}$$

where $d(y, \Psi \backslash \{y\})$ is the distance between the location y and the nearest point of Ψ except y.

If the ball we surveyed contains no point (in other words the point y is not a member of Ψ), then we can find the contact distribution $F_y(.)$ that represents the smallest radius necessary for the $b(y, r)$ to contact a point in Ψ using the void probability as given below [13].

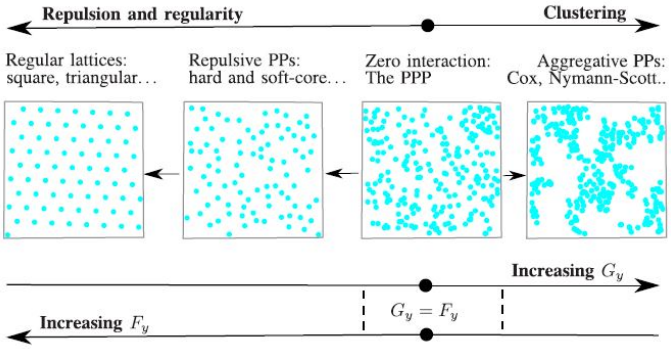

Figure 2.19 Tendency toward regularity or clustering of PPs [13].

$$\begin{aligned} F_y(r) &= \mathbb{P}\left(d(y,\Psi) \leq r\right) \\ &= 1 - void(b(y,r)) \\ &= 1 - \mathbb{P}\left(N(b(y,r)) = 0\right) \end{aligned} \tag{3}$$

In other words, the nearest neighbor distance determines how close the points are to each other, and it also shows the clustering. On the other hand, the conduct distance determines how regularly distributed the points are on the map. In the totally random PPs, such as the PPP, they are equal, $F = G$, while $G > F$ for clustered PPs and $G < F$ for regular PPs as illustrated in Fig. 2.19 [13].

If we condition to a point in the space of PP, the distribution of the PP might change. However, if we are dealing with the PPPs, conditioning does not change the distribution of the PPP. This theorem is called Slivnyak-Mecke theorem and to understand this we need to have a look at the reduced Palm probability. Let's consider the point y from a stationary PP Ψ and shift Ψ such that the y lies at the point o (origin). For a given set $B = b(y,r)$, reduced Palm probability is the ratio between the mean number of points in B except y (this is called the reduced Campbell measure) and the mean number of points inside B (notice that the point y shifted to the origin so the ball becomes $b(0,r)$) [13]. Formally,

$$\mathbb{P}_o^!(\Psi \in \mathcal{A}) = \frac{1}{\lambda\, \nu(B)} \mathbb{E}\left(\sum_{y \in \Psi \cap B} \mathbb{1}_{\mathcal{A}}(\Psi_{-y} \backslash \{y\}) \right) \tag{4}$$

where in the $\mathbb{P}_o^!$, the index o and superscript ! represents the shifting Ψ towards the origin and excluding y, respectively. The $\mathcal{A}$ is the event that the number of points inside the shifted ball excluding y is not zero ($N(b(y,r)\backslash\{y\}) > 0$, Ψ_{-y} is the shifted PP, $\nu(B)$ is the Lebesgue measure (area of B in two-dimensions), and $\lambda\nu(B)$ represents the average number of points inside B.

Coming back to the Slivnyak-Mecke theorem again, for an HPPP with density λ, the number of points falling in disjoint sets is independent. Therefore, the points in an HPPP are independent, and conditioning to a point in the map does not affect the statistics of the PP. This also means that the reduced Palm probability equals the original distribution counting y for the Slivnyak-Mecke theorem.

$$\mathbb{P}_y^!(\Psi \in .) = \mathbb{P}(\Psi \in .) \tag{5}$$

As we recall the nearest neighbor distance and the conduct distance distributions, the only difference is the inclusion of the point y or not. Hence, for an HPPP, the nearest neighbor distance distribution and the conduct distance distribution will be equal to each other by the Slivnyak-Mecke theorem.

To simulate the PPP with the density λ, we need to generate n number of points in the given area $|B|$ ($\lambda|B|$). Then, we randomly scatter the points on the map. If the density of points depends on their locations, this PP is called inhomogeneous PPP (IPPP). On the other hand, if we randomly and independently select points from the primary PPP Ψ according to a probability $p(x)$, we are left with the PP Ψ^p. This process preserves the Poisson law and is called independent thinning of Ψ, in other words, Ψ^p is also a PPP but its intensity will be equal to $\int_{\mathbb{R}^2} p(x)\Lambda(dx)$ (it is an IPPP). However, if the probability $p(x)$ is a constant ratio ($p(x) = p$), then this type of thinning is called p-thinning and it also preserves the homogeneity, e.g. if the primer PPP is an HPPP, then resulting PPP will also be an HPPP.

3. RELATED WORKS

Coverage analysis of SG based networks examined for various system models in the literature. However, there is a limited number of works that consider IRSs in their network models.

In [40], authors investigated an SG-based IRS-assisted network for the ergodic capacity, energy efficiency, and OP. However, the blockages are not considered. Instead, the fraction of the BSs contributes to the direct and indirect communication modeled with a constant value. In our work, we explicitly model the location of blockages and find the ratio of indirect and direct links which gives the contribution of IRSs to network coverage.

Ghatak et al. use the Poisson line process to model the BSs and blockages in a typical street in [41]. The authors assumed that two IRSs are deployed on either side of the BSs at a constant distance and the TUE can only use LoS links for DL communications. With these assumptions, the coverage probability is investigated. However, in this thesis, we take a two-dimensional map rather than a street to measure the coverage probability and we assumed that the IRSs are deployed into buildings independently with a constant ratio.

The very first study which considers the effect of the blockage for the coverage analysis in an SG-based mmWave network is [14]. The authors assumed that the TUE at the origin can communicate with a LoS or NLoS BS according to its PL value. The Nakagami-m fading is used for each channel and the SNR expression is derived for both LoS and NLoS paths. Furthermore, the LoS probability expression is approximated with a LoS ball model, which assumes that the LoS probability is a step function whose value is zero after a certain distance. However, IRSs are not considered in this work, since its a relatively new concept.

In the SG-based mmWave network context, studies which takes IRSs into consideration in their network models for the coverage analysis can be listed as [15, 16, 42–44]. Authors in [42] assume a DL communication between the TUE and BSs through the direct link or the indirect link through an IRS. The coverage probability is derived with the SIR expression which assumes the interference is created with just the direct BSs and the small scale fading as an exponentially distributed random variable. The authors take the PL model of indirect link as a product-distance model. However, the blockages does nor considered in [42].

Lyu et al. considers both the IRS and SG-based network model to model the locations of BSs and IRSs in their study [44]. First, the channel power distribution is derived then the signal and interference power distributions are obtained to find the coverage probability. However, the authors also do not consider the blockage effect in their network model.

In [43], the OP and ergodic rate of an IRS-aided SG based network is analyzed. However, they assume that there is only one BS and one IRS in the system, and their locations are fixed. Only the positions of UEs are randomly chosen according to the HPPP. The BS serves m UEs through the IRS, and they assume that the direct links between BS and UEs are blocked, e.g. NLoS. UEs can only communicate through IRS and these links are LoS. Furthermore, they give an RCM and combiner design in their study.

Authors in both [15] and [16] insert a line Boolean model, which assumes that the buildings have zero width, e.g. lines, of blockages whose centers are distributed with HPPP. They both take the sum distance model for the PL expression of indirect link, which is not a practical assumption for the far-field scenario. They both assume that the indirect link can only be created with LoS link but authors in [43] assume either LoS or NLoS case for the direct link. On the other hand, in [15], a fully LoS dependent network is considered. The TUE is associated with a BS according to minimum PL criteria which compares the PL of direct and indirect links and chooses the minimum for communication. Authors in [43] derive the coverage probability with the SINR expression but in [15], they use blind-spot analysis.

4. COVERAGE ANALYSIS

In this section, we will discuss the SNR coverage probability of SG-based mmWave networks. First, we give the system model that we used in our analysis including the UE association, PL models of direct and indirect links, SG-based network parameters, received signals, and the SNR expressions. Then we present our method to reach a closed-form expression for the coverage probability. In this subsection, we will discuss about the various cases for coverage, distance distributions given in the previous works, our approximation for these distributions and validity of this approach, the closed-form expression for the

distribution of the product distance, the ratio of feasible BSs, and finally the SNR coverage probabilities.

4.1. System Model

We consider that the locations of base stations (BSs) form an HPPP Φ_{BS} with density λ_{BS} on the R^2 plane, and all the BSs have the same transmit power P_t. Blockages, typically buildings, form a Boolean scheme of rectangles [45] whose centers follow HPPP with density λ_b. We assume that the blockage distribution is stationary and isotropic, which means that the distribution is invariant to the motions of translation and rotation. We define a blockage with three parameters which are its length, width, and orientation. The expected value of the length and the width of blockages are defined as $\mathbb{E}[L]$ and $\mathbb{E}[W]$, respectively. The orientation of the buildings θ_b is uniformly distributed on $[0, \pi]$.

IRSs are deployed optimally[1] to just one of the four facades of a building with the ratio μ. Hence, by the independent p-thinning of HPPP, the buildings containing an IRS follow an HPPP Φ_{IRS} with density $\lambda_b\mu$. UEs are distributed as a stationary PP independent of the BSs and the buildings on the plane, and the TUE is assumed to be located at the origin. Since the UEs are distributed independently and follow a stationary PP, the DL SNR experienced by the TUE has the same distribution as the aggregate ones [14].

We assume that the communication is done through LoS links, in other words, waves cannot penetrate buildings and the LoS component is dominant in the channel. The LoS probability in an SG based network is derived in [45], which is $p(r) = \exp(-\beta r)$ where $\beta = 2\lambda_b/\pi(\mathbb{E}[L] + \mathbb{E}[W])$ for the outdoor UEs.

The TUE can only be associated with one BS. This connection can be made through either with a direct LoS-link or an indirect LoS-link. The direct LoS-link is the link between the LoS BS and the TUE. The indirect LoS-link is created with two independent LoS links, which are the link between the TUE and the LoS IRS, and the link between the IRS and the LoS BS. These possible connections can be seen from Fig 4.1. We assumed that the

[1]We assume that the IRS is deployed on the facade of the buildings which can be reached from the TUE (it applies to all buildings, e.g. it includes LoS buildings and also the NLoS buildings). Otherwise, if the IRSs are deployed onto the buildings randomly, we just need to multiply the ratio of feasible BSs (given in the sequel) with 1/4.

TUE can be associated with either the nearest LoS BS, which constructs the direct LoS link, or the nearest LoS IRS. Then, the IRS can be associated with the nearest LoS BS so that this UE-IRS-BS link forms the indirect LoS link. Throughout the thesis, we will call the link between TUE and the nearest LoS BS as UE-BS link, the link between the TUE and the nearest LoS IRS as UE-IRS link, and the link between the IRS and nearest LoS BS as IRS-BS link. For example, in Fig 4.1, the UE-BS link (direct link) is the link between BS4 and TUE because the nearest LoS BS to the TUE is the BS4. On the other hand, the indirect LoS-link is the link between UE-IRS2-BS2, since the nearest LoS IRS to the origin is IRS2 and the nearest LoS BS to the IRS2 is the BS2. The TUE can only be associated with either BS4 or BS2, and this selection is made by comparing the PL of these two links. In other words, if the TUE sees both the direct LoS BS and the indirect LoS BS, then it decides which one to connect by comparing their PL values. However, if it sees only a direct LoS BS or an indirect LoS BS, then it connects to this available BS without any further comparison. We also assume that the indirect link can only be made through just one IRS, we do not consider the links using multiple IRSs.

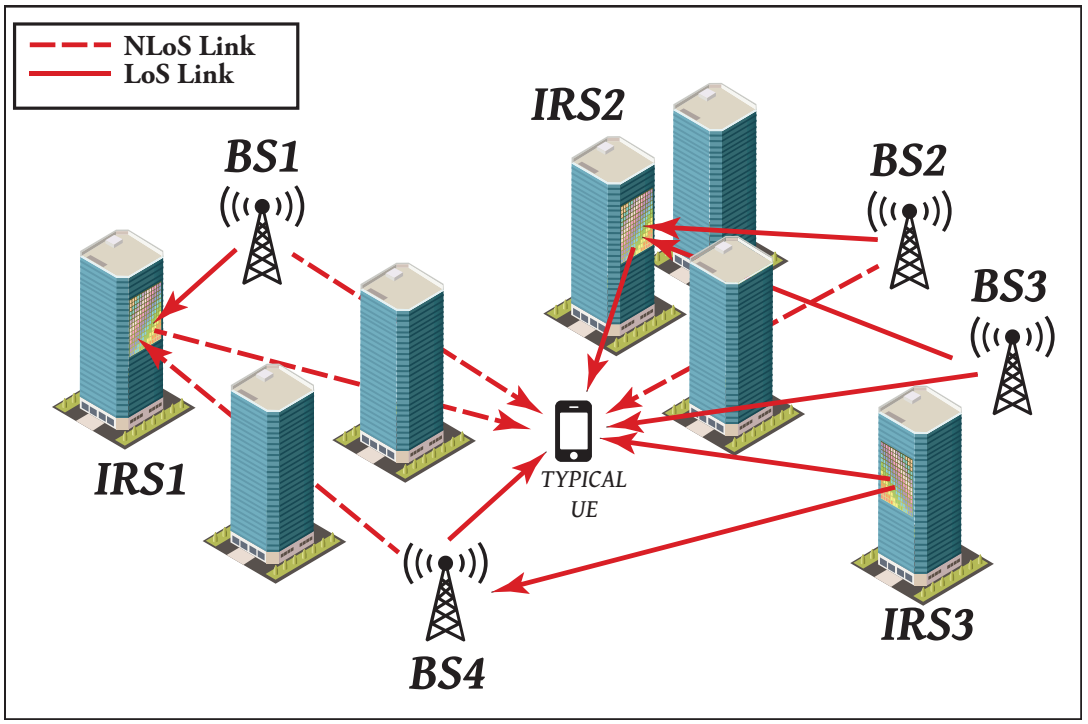

Figure 4.1 UE Association.

In the literature, there are two different PL expressions for the indirect link, which are the product-distance PL model and the sum-distance PL model [38]. The sum-distance PL

considers the IRS as a perfect electric conductor (PEC) but it is not practical. In [37], authors show experimentally that the product-distance PL is more suitable for far-field applications, and the sum-distance is only applicable to near-field scenarios. In [46], the authors derived the indirect link PL expression as given below, and we use this PL expression in our derivations.

$$\begin{aligned} PL_I(z,\theta_i) &= \frac{(4\pi)^2}{G_t G_r}\left(\frac{z}{N_a N_b}\right)^2\left(\frac{N_a}{a}\frac{N_b}{b}\frac{1}{cos(\theta_i)}\right)^2 \\ &\overset{(a)}{=} \left(\frac{z}{N}\right)^2 \frac{1}{C}\left(\frac{2}{\lambda cos\theta_i}\right)^2 \end{aligned} \tag{6}$$

where $z = d_{UI}d_{IB}$, d_{UI} and d_{IB} are the distances of the links UE-IRS, and IRS-BS, respectively. G_t and G_r are the transmit antenna gain, and receiver antenna gain, respectively. $\theta_i \in [0, \pi/2]$ is the angle between the normal vector of IRS and the incident wave. $N_a \times N_b$ is the number of elements in IRS, and we assume that all the IRSs have the same number of elements. $\frac{a}{N_a} \times \frac{b}{N_b}$ is the size of each element on IRS. Without loss of generality, we take $C = (\frac{\lambda\sqrt{G_t G_r}}{4\pi})^2$, $N_a = N_b$, $N_a N_b = N$, $a = b$, $\frac{a}{N_a} = \frac{b}{N_b} = 0.7071\ \lambda$, [2] ($\lambda$ is the wavelength) in the step (a).

And the PL expression for the direct link is,

$$\begin{aligned} PL_D(d_{UB}) &= \frac{(4\pi)^2}{G_t G_r \lambda^2} d_{UB}^2 \\ &= \frac{d_{UB}^2}{C} \end{aligned} \tag{7}$$

where the d_{UB} represents the distance of UE-BS link.

Finally, the received signals for direct link and indirect link given by

$$\begin{aligned} y_D &= \frac{1}{\sqrt{PL_D(d)}} h_D x\ + n, \\ y_I &= \frac{1}{\sqrt{PL_I(z)}} \frac{1}{N} (\mathbf{h_2}^T \mathbf{\Phi} \mathbf{h_1}) x\ + n \end{aligned}$$

[2] With the inter-element spacing's, the value of a/N_a will be greater than $\lambda/5$. We take the paper [8] as a reference for this value. They designed an IRS with the center to center distance of IRS elements being equal to 3.5mm which approximately equals to $0.7071\ \lambda$ at 60 GHz

where x is the normalized transmitted signal, n represents the additive white Gaussian noise with zero mean and variance σ_n^2, $\mathbf{\Phi} = diag\{[e^{j\phi_1}, e^{j\phi_2}, \cdots, e^{j\phi_N}]\}$ denotes the reflection coefficient matrix (RCM) where $\phi_i \in [0, 2\pi)$ is the phase shift of i-th element of the IRS, h_D denotes the UE-BS channel, $\mathbf{h_2}$ and $\mathbf{h_1}$ denote the UE-IRS and IRS-BS channels, respectively, and the scaling parameter $1/N$ comes from the array response vectors. Since we consider a LoS dependent network, all the channels are modeled by Rician fading, and they all have the same shape (K) and scale (Ω) parameters. We assumed perfect channel state information (CSI), optimal array response vectors, and optimal RCM design which has phase shifts perfectly aligned with the phase of cascaded channel. Hence the SNR[3] expression for the direct link is given by,

$$SNR_D = \frac{|h_D|^2}{PL_D(d)\ \sigma_n^2} \tag{8}$$

and for the indirect link,

$$SNR_I = \frac{\left(\frac{1}{N}\sum_{n=1}^{N} |h_{1,n}|\ |h_{2,n}|\right)^2}{PL_I(z,\theta_i)\ \sigma_n^2} \tag{9}$$

where $h_{1,n}$ and $h_{2,n}$ denote the independent[4] channels between UE and n-th element of LoS IRS, and n-th element of IRS and LoS BS, respectively.

4.2. Method

The main purpose of this thesis is to give a closed-form expression for the following coverage probability as

$$P_c(T) = \mathbb{P}(SNR > T) \tag{10}$$

where T denotes the SNR threshold.

[3]In this thesis, our main goal is to compare the IRS-aided network with the network without IRS, and analyze the coverage enhancement. Also, since the IRS introduced a new concept called smart radio environment [47], we leave the interference analysis to future works.

[4]In the literature most of the works regarding OP analysis in IRS-assisted networks consider independent channels for different IRS elements ([48], [49], [50]). Hence, we leave the OP analysis of IRS-assisted MIMO systems with Rician fading and correlated IRS elements' channels to future works.

Since there are four different cases for the TUE to connect to a BS, we examined the coverage probability with four mutually exclusive events. First of all, the TUE can connect a direct LoS BS or an indirect LoS BS. These events can be split into two events such that the TUE cannot reach any direct LoS BS or indirect BS, and it connects to the direct LoS BS or indirect LoS BS, respectively. The other scenario is that the TUE sees both a direct LoS BS and an indirect LoS BS, in that case, it connects to a BS that has a lower PL value. Hence, the coverage probability in (10) can be expressed as follows,

$$\begin{aligned}
P_c(T) =& \mathbb{P}(SNR > T) \\
=& \mathbb{P}(A_D)P_{c,D}(T) + \mathbb{P}(A_I)P_{c,I}(T) \\
=& \mathbb{P}(A_{D1}) \int_0^\infty \mathbb{P}(SNR_D(x) > T \,|x) f_D(x|A_{D1})dx + \\
& \mathbb{P}(A_{D2}) \int_0^\infty \mathbb{P}(SNR_D(x) > T \,|x) f_D(x|A_{D2})dx + \\
& \mathbb{P}(A_{I1}) \int_0^\infty \mathbb{P}(SNR_I(z) > T \,|z) f_I(z|A_{I1})dz + \\
& \mathbb{P}(A_{I2}) \int_0^\infty \mathbb{P}(SNR_I(z) > T \,|z) f_I(z|A_{I2})dz
\end{aligned} \tag{11}$$

where

$A_{D1} = \{PL_D < PL_I\} \cap \{$There is at least one direct LoS-link$\} \cap$
$\{$There is at least one indirect LoS BS$\}$, indicates the event that TUE has both direct LoS-link and indirect LoS-link available, and it connects to the direct LoS BS, since the PL of the direct link is less than the indirect link,

$A_{D2} = \{$There is at least one direct LoS-link$\} \cap \{$There are not any indirect LoS BS$\}$, indicates the event that the TUE can only reach the direct LoS BS. Hence it connects to the direct LoS BS,

$A_{I1} = \{PL_I < PL_D\} \cap \{$There is at least one direct LoS-link$\} \cap$
$\{$There is at least one indirect LoS-BS link$\}$, indicates the event that the TUE has both direct LoS-link and indirect LoS-link available, and it connects to the indirect LoS BS, since the PL of indirect link is less than the direct link,

A_{I2} = {There is at least one indirect LoS-link} $\cap$ {There are not any direct LoS BS}, indicates the event that the TUE can only reach the indirect LoS BS, and it connects to the indirect LoS BS,

$f_D(x)$ is the pdf of the UE-BS link's distance given that the TUE can communicate with at least one direct LoS BS

$f_I(z)$, is the pdf of multiplication of the distances of the UE-IRS link, and the IRS-BS link given that the TUE sees at least one LoS IRS and the IRS can reach at least one LoS BS.

4.2.1. Distributions of the Distances

In an SG-based network with PPP distributed nodes and rectangular Boolean scheme of blockages, the distance between the nearest LoS node and the origin is dependent on the intensity of nodes under examination [14]. For the direct LoS link, the intensity of LoS BSs is $\lambda_{BS}\, p(r)$ by independent thinning. Hence, the distribution of the nearest LoS BS's distance given that the UE sees at least one LoS BS is

$$f_{d_{UB}}(x) = \frac{1}{B_{UB}} 2\pi\lambda_{BS} x \, \exp(-\beta x - \frac{2\pi\lambda_{BS}}{\beta^2}(1-(\beta x+1)e^{-\beta x})) \tag{12}$$

where:

B_{UB} = $\int_0^\infty 2\pi\lambda_{BS} x \, \exp(-\beta x - \frac{2\pi\lambda_{BS}}{\beta^2}(1-(\beta x+1)e^{-\beta x}))dx$

For the UE-IRS link, the intensity of LoS IRSs is $\lambda_b \mu \; p(r)$. Hence, the distribution of the distance of UE-IRS link given that the TUE can reach at least one LoS IRS is given by,

$$f_{d_{UI}}(x) = \frac{1}{B_{UI}} 2\pi\lambda_b \mu \, x \, \exp(-\beta x - \frac{2\pi\lambda_b \mu}{\beta^2}(1-(\beta x+1)e^{-\beta x})) \tag{13}$$

where:

B_{UI} = $\int_0^\infty 2\pi\lambda_b \mu \, x \, \exp(-\beta x - \frac{2\pi\lambda_b \mu}{\beta^2}(1-(\beta x+1)e^{-\beta x}))dx$

The probability that a BS is feasible is ξ (more detailed information will be given in Section 4.2.3.). Hence, the intensity of feasible BSs will be $\xi\ \lambda_{BS}\ p(r)$, and the pdf of the distance of IRS-BS link given that the IRS sees at least one LoS BS is given by,

$$f_{d_{IB}}(x) = \frac{1}{B_{IB}}\ 2\pi\xi\lambda_{BS}x\ \exp(-\beta x - \frac{2\pi\xi\lambda_{BS}}{\beta^2}(1-(\beta x+1)e^{-\beta x})) \tag{14}$$

where:

B_{IB} = $\int_0^\infty 2\pi\xi\lambda_{BS}x\ \exp(-\beta x - \frac{2\pi\xi\lambda_{BS}}{\beta^2}(1-(\beta x+1)e^{-\beta x}))dx$

Let $d_{UI} = Y \sim f_{d_{UI}}(y)$ and $d_{IB} = X \sim f_{d_{IB}}(x)$, where $X, Y > 0$ are independent[5] random variables represent the length of UE-IRS link and IRS-BS link, respectively. Hence, the distribution of the product-distance $f_I(z)$ can be found by the transformation of random variables such that $Z = XY$ as follows,

$$\begin{aligned} F_I(z) &= \mathbb{P}(Z \le z) = \mathbb{P}(XY \le z) \\ &\overset{\text{(a)}}{=} \mathbb{P}(Y \le \frac{Z}{X}) \\ &= \int_0^\infty f_X(x) \int_0^{Z/X} f_Y(y)dydx \\ \frac{\mathrm{d}F_I(z)}{\mathrm{d}z} &= f_I(z) \\ &\overset{\text{(b)}}{=} \int_0^\infty f_X(x) f_Y(\frac{z}{x})\frac{1}{x}dx \end{aligned} \tag{15}$$

where we used the fact that $X > 0$ in (a), and the Leibniz rule in (b). The expression in (15) is called as "multiplicative convolution".

Lemma 0.1 (Multiplicative Convolution [51])**.** *For the functions Z_1 and Z_2, the multiplicative convolution is defined by*

$$Z_1 \vee Z_2 \equiv \int_0^\infty Z_1(\nu')\ Z_2(\frac{\nu}{\nu'})\ \frac{d\nu'}{\nu'} \tag{16}$$

[5]By the Slivnyak's theorem, conditioning on a point does not change the distribution of the rest of the process.

If we substitute (14) and (13) into (15), we get

$$f_I(z) = \frac{1}{B_{UI}B_{IB}} G_1 z \int_0^\infty e^{-\beta(x+\frac{z}{x})} \exp(G_2(x\beta+1)e^{-x\beta} + G_3(\frac{z\beta}{x}+1)e^{-z\beta/x})\frac{1}{x}dx \quad (17)$$

where:

$G_1 = G_2 G_3 \beta^4 \exp(-G_2 - G_3),\ G_2 = 2\pi\xi\lambda_{BS}/\beta^2,\ G_3 = 2\pi\lambda_b\mu/\beta^2$

The above distributions (17) and (12) are too cumbersome for analytical calculations. Therefore, we proposed to approximate the pdf's of individual links [(12), (13), and (14)] with gamma distribution.

4.2.2. Gamma Approximation of The Nearest-LoS Neighbor Distance Distributions

First of all, we will give the general result of the gamma approximation of the distribution of the nearest LoS node with intensity $G/(2\pi)\ p(r)$. Then, we will give the approximate distribution of $f_{d_{UB}}(x)$, $f_{d_{UI}}(x)$, and $f_{d_{IB}}(x)$. Consider the distribution given below,

$$f_X(x) = \frac{1}{B} G x exp(-\beta x - G\frac{1}{\beta^2}(1-(\beta x+1)e^{-\beta x})) \quad (18)$$

where:

$B = \int_0^\infty Gx\ \exp(-\beta x - G\frac{1}{\beta^2}(1-(\beta x+1)e^{-\beta x}))dx$, and X denotes the distance to the nearest LoS node to the origin with the nodes distributed as PPP with intensity $G/(2\pi)\ p(r)$. To approximate the distribution $f_X(x)$ with gamma pdf $\Gamma(k,\theta)$, we need to find the shape k and scale parameters θ of gamma distribution. We use moment matching approach to find these parameters. Let $Y \sim \Gamma(k,\theta)$ and $X \sim f_X(x)$,

$$\begin{aligned}
\mathbb{E}[X] &= \mathbb{E}[Y] = k\theta \\
var(X) &= var(Y) = \mathbb{E}[Y^2] - \mathbb{E}[Y]^2 \\
&= \theta^2\frac{\Gamma(k+2)}{\Gamma(k)} - k^2\theta^2 \\
&= k(k+1)\theta^2 - k^2\theta^2 \\
k &= \frac{\mathbb{E}[X]^2}{var(X)} \quad (19)
\end{aligned}$$

$$\theta = \frac{var(X)}{\mathbb{E}[X]} \tag{20}$$

Hence, we need to find the mean value and the variance of X.

$$\begin{aligned}
\mathbb{E}[X] &= \int_0^\infty x\, \frac{1}{B} Gx\, \exp(-\beta x - G\frac{1}{\beta^2}(1-(\beta x+1)e^{-\beta x}))\, dx \\
&= \frac{G}{B}\int_0^\infty x^2 \exp(-\frac{G}{\beta^2}) \exp(-\beta x + \frac{G}{\beta^2}(\beta x+1)e^{-\beta x})\, dx \\
&= \frac{G}{B}\exp(-G/\beta^2)\int_0^\infty x^2 \exp(-\beta x + \frac{G}{\beta^2}(\beta x+1)e^{-\beta x})\, dx \\
&= \frac{\beta^2\gamma e^{-\gamma}}{B}\int_0^\infty x^2 \exp(-\beta x + \gamma(\beta x+1)e^{-\beta x})\, dx \\
&\overset{\text{(a)}}{=} \frac{\beta^2\gamma e^{-\gamma}}{B}\int_1^0 \frac{(\ln(u))^2}{\beta^2}\exp(\ln(u) + \gamma(-\ln(u)+1)u))\, \frac{-1}{\beta u}\, du \\
&= \frac{\gamma e^{-\gamma}}{B}\int_1^0 (\ln(u))^2 \exp(-\gamma u\ln(u) + \gamma u)\, \frac{-1}{\beta u}\, du \\
&= \frac{\gamma e^{-\gamma}}{\beta B}\int_0^1 (\ln(u))^2 \exp(-\gamma u\ln(u) + \gamma u)\, du
\end{aligned} \tag{21}$$

where $\gamma = \frac{G}{\beta^2}$, and in step (a) we employed a change of variables $u = e^{-\beta x}$

The integral in (21) cannot be reduced to closed form directly. Hence, we use Maclaurin expansion of $\exp(-\gamma u\ln(u) + \gamma u)$. Since the integral is defined between 0 and 1, this approximation gives us a proper result. Comparison of this approximation with the original function can be seen in Fig(4.2) (for $G = 2\pi\lambda_{BS}$, $\mathbb{E}[L] = 55$, $\mathbb{E}[W] = 52$, $\lambda_b = 9.3\times10^{-5}$, $\lambda_{BS} = 7.5\times10^{-6}$, and maximum value for k=100).

$$\exp(-\gamma x\ln(x) + \gamma x) \approx \sum_{k=0}^{\infty} \frac{(-\gamma x(\ln(x)-1))^k}{k!} \tag{22}$$

Now substitute (22) to (21),

$$\begin{aligned}
\mathbb{E}[X] &= \frac{\gamma e^{-\gamma}}{\beta B}\int_0^1 (\ln(x))^2 \exp(-\gamma x\ln(x) + \gamma x)\, dx \\
&\approx \zeta \int_0^1 (\ln(x))^2 \sum_{k=0}^{\infty}(-1)^k \frac{\gamma^k x^k(\ln(x)-1)^k}{k!}\, dx \\
&= \zeta \sum_{k=0}^{\infty}\gamma^k \frac{(-1)^k}{k!}\int_0^1 (\ln(x))^2 x^k(\ln(x)-1)^k\, dx
\end{aligned}$$

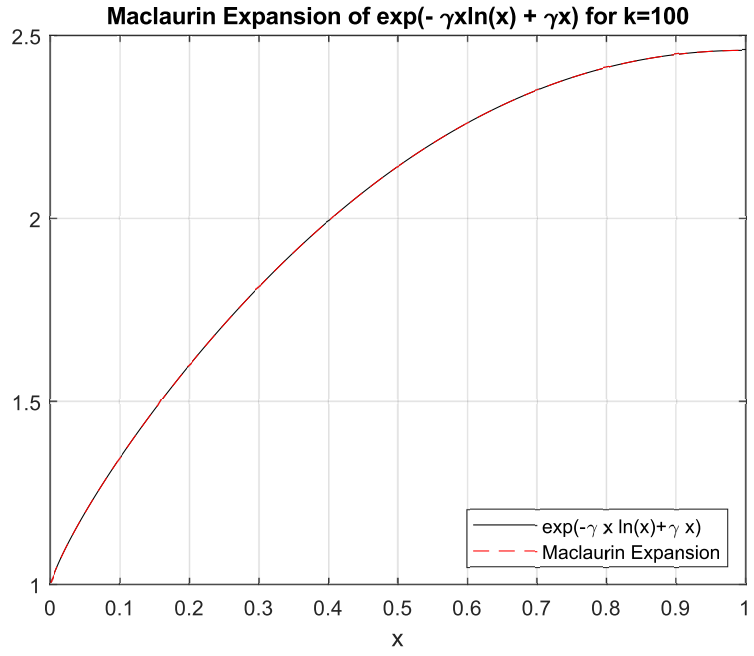

Figure 4.2 Maclaurin expansion, eqn.(22).

$$
\begin{aligned}
&\overset{(a)}{=} \zeta \sum_{k=0}^{\infty} \gamma^k \frac{(-1)^k}{k!} \int_{-\infty}^{-1} (\tau+1)^2 (e^{\tau+1})^k \tau^k e^{\tau+1}\, d\tau \\
&= \zeta \sum_{k=0}^{\infty} \gamma^k \frac{(-1)^k}{k!} \int_{-\infty}^{-1} (\tau+1)^2 \tau^k e^{(\tau+1)(k+1)}\, \tau \\
&\overset{(b)}{=} \zeta \sum_{k=0}^{\infty} \gamma^k \frac{(-1)^k}{k!} \int_{\infty}^{k+1} \left(\frac{-m}{k+1}+1\right)^2 \left(\frac{-m}{k+1}\right)^k e^{-m} e^{k+1} \left(\frac{-dm}{k+1}\right) \\
&= \zeta \sum_{k=0}^{\infty} \gamma^k \frac{(-1)^{k+1}}{k!} \int_{k+1}^{\infty} \left(\frac{k+1-m}{k+1}\right)^2 (-1)^k \frac{m^k}{(k+1)^k} e^{-m} e^{k+1} \left(\frac{-dm}{k+1}\right) \\
&= \zeta \sum_{k=0}^{\infty} \gamma^k \frac{\cancel{((-1)^{2k+2})}^{1}}{k!} \frac{1}{(k+1)^{k+3}} e^{k+1} \int_{k+1}^{\infty} (k+1-m)^2 m^k e^{-m}\, dm \\
&= \zeta \sum_{k=0}^{\infty} \frac{\gamma^k}{k!} \frac{e^{k+1}}{(k+1)^{k+3}} \int_{k+1}^{\infty} \left((k+1)^2 - 2m(k+1) + m^2\right) m^k e^{-m}\, dm \\
&= \zeta \sum_{k=0}^{\infty} \frac{\gamma^k}{k!} \frac{e^{k+1}}{(k+1)^{k+3}} \left(\int_{k+1}^{\infty} (k+1)^2 m^k e^{-m}\, dm - \right. \\
&\qquad \left. 2(k+1) \int_{k+1}^{\infty} m^{k+1} e^{-m}\, dm + \int_{k+1}^{\infty} m^{k+2} e^{-m}\, dm \right) \\
&= \zeta \sum_{k=0}^{\infty} \frac{\gamma^k}{k!} \frac{e^{k+1}}{(k+1)^{k+3}} \Big((k+1)^2\, \Gamma(k+1, k+1) - \\
&\qquad 2(k+1)\, \Gamma(k+2, k+1) + \Gamma(k+3, k+1) \Big)
\end{aligned}
$$

$$\stackrel{(c)}{=} \zeta \sum_{k=0}^{\infty} \frac{\gamma^k}{k!} \frac{e^{k+1}}{(k+1)^{k+3}} (k+1) e^{-(k+1)} \left(e^{k+1}\, \Gamma(k+1, k+1) + (k+1)^k \right)$$

$$= \zeta \sum_{k=0}^{\infty} \frac{\gamma^k}{k!} (k+1)^{-(k+2)} \left(e^{k+1}\, \Gamma(k+1, k+1) + (k+1)^k \right) \tag{23}$$

where $\zeta = \frac{\gamma e^{-\gamma}}{\beta B}$, and $\Gamma(s,x) = \int_x^{\infty} t^{s-1} e^{-t}\, dt$ is the upper incomplete gamma function. In the step (a) and (b) we employed a change of variables $\ln(x) - 1 = \tau$ and $-\tau(k+1) = m$, respectively. In the step (c), we used the fact that $\Gamma(s+1, x) = s\, \Gamma(s,x) + x^s e^{-x}$.

To find $var(X)$, we need to find $\mathbb{E}[X^2]$, first.

$$\mathbb{E}[X^2] = \frac{-\gamma e^{-\gamma}}{\beta^2 B} \int_0^1 (\ln(u))^3\, \exp(-u\gamma(\ln(u) - 1))\, du$$

$$\approx \frac{-\zeta}{\beta} \int_0^1 (\ln(x))^3 \sum_{k=0}^{\infty} \frac{(-\gamma\, x(\ln(x) - 1)^k}{k!}\, dx$$

$$= \frac{-\zeta}{\beta} \sum_{k=0}^{\infty} (-1)^k \frac{\gamma^k}{k!} \int_0^1 (\ln(x))^3 x^k (\ln(x) - 1)^k\, dx$$

$$\stackrel{(a)}{=} \frac{-\zeta}{\beta} \sum_{k=0}^{\infty} (-1)^k \frac{\gamma^k}{k!} \int_{-\infty}^{-1} (\tau + 1)^3\, e^{k(\tau+1)}\, \tau^k e^{\tau+1}\, d\tau$$

$$= \frac{-\zeta}{\beta} \sum_{k=0}^{\infty} (-1)^k \frac{\gamma^k}{k!} \int_{-\infty}^{-1} (\tau + 1)^3\, \tau^k e^{(\tau+1)(k+1)}\, d\tau$$

$$\stackrel{(b)}{=} \frac{-\zeta}{\beta} \sum_{k=0}^{\infty} (-1)^k \frac{\gamma^k}{k!} \int_{\infty}^{k+1} \left(1 - \frac{m}{k+1}\right)^3 \left(\frac{-m}{k+1}\right)^k e^{-m+k+1}\, \frac{dm}{-(k+1)}$$

$$= \frac{-\zeta}{\beta} \sum_{k=0}^{\infty} (-1)^k \frac{\gamma^k}{k!} \int_{k+1}^{\infty} (-1) \frac{(k+1-m)^3}{(k+1)^3} (-1)^k \frac{m^k}{(k+1)^k} e^{-m} e^{k+1} \frac{(-1)}{(k+1)}\, dm$$

$$= \frac{-\zeta}{\beta} \sum_{k=0}^{\infty} \cancel{((-1)^{2k+2})}^{\,1}\, \frac{\gamma^k}{k!} \frac{e^{k+1}}{(k+1)^{k+4}} \int_{k+1}^{\infty} (k+1-m)^3 m^k e^{-m}\, dm$$

$$= \frac{-\zeta}{\beta} \sum_{k=0}^{\infty} \frac{\gamma^k}{k!} \frac{e^{k+1}}{(k+1)^{k+4}} \int_{k+1}^{\infty} \left[(k+1)^3 - 3(k+1)^2 m + 3(k+1)m^2 - m^3\right] m^k e^{-m}\, dm$$

$$= \frac{-\zeta}{\beta} \sum_{k=0}^{\infty} \frac{\gamma^k}{k!} \frac{e^{k+1}}{(k+1)^{k+4}} \left[\int_{k+1}^{\infty} (k+1)^3 m^k e^{-m}\, dm \; - 3 \int_{k+1}^{\infty} (k+1)^2 m^{k+1} e^{-m}\, dm + \right.$$

$$\left. 3 \int_{k+1}^{\infty} (k+1) m^{2+k} e^{-m}\, dm \; - \int_{k+1}^{\infty} m^{3+k} e^{-m}\, dm \right]$$

$$= \frac{-\zeta}{\beta} \sum_{k=0}^{\infty} \frac{\gamma^k}{k!} \frac{e^{k+1}}{(k+1)^{k+4}} \left[(k+1)^3 \int_{k+1}^{\infty} m^k e^{-m}\, dm \; - 3(k+1)^2 \int_{k+1}^{\infty} m^{k+1} e^{-m}\, dm + \right.$$

$$\left. 3(k+1) \int_{k+1}^{\infty} m^{2+k} e^{-m}\, dm \; - \int_{k+1}^{\infty} m^{3+k} e^{-m}\, dm \right]$$

$$= \frac{-\zeta}{\beta} \sum_{k=0}^{\infty} \frac{\gamma^k}{k!} \frac{e^{k+1}}{(k+1)^{k+4}} \Big[(k+1)^3 \, \Gamma(k+1, k+1) \; - 3(k+1)^2 \, \Gamma(k+2, k+1) +$$

$$3(k+1) \, \Gamma(k+3, k+1) \; - \; \Gamma(k+4, k+1) \Big]$$

$$\stackrel{\text{(c)}}{=} \frac{-\zeta}{\beta} \sum_{k=0}^{\infty} \frac{\gamma^k}{k!} \frac{e^{k+1}}{(k+1)^{k+4}} (-1) \, 2(k+1) \; \Big(\Gamma(k+1, k+1) \; + \; (k+2) \, e^{-(k+1)} \, (k+1)^k \Big)$$

$$= \frac{2\zeta}{\beta} \sum_{k=0}^{\infty} \frac{\gamma^k}{k!} (k+1)^{-(k+3)} \Big(e^{k+1} \, \Gamma(k+1, k+1) \; + \; (k+2) \, (k+1)^k \Big)$$

where $\Gamma(s, x) \; = \; \int_x^{\infty} t^{s-1} e^{-t} \, dt$ is the upper incomplete gamma function. We employed change of variables $\ln(x) - 1 = \tau$ in (a), and $-\tau(k+1) = m$ in (b), and in the step (c), we used the fact that $\Gamma(s+1, x) = s \, \Gamma(s, x) + x^s e^{-x}$.

Hence, the shape and scale parameters of the gamma approximation of $f_X(x)$, eqn.(18), are as follows,

$$k = \frac{\mathbb{E}[X]^2}{var(X)}, \quad \theta = \frac{var(X)}{\mathbb{E}[X]},$$

where

$$\begin{aligned}
& var(X) = \mathbb{E}[X^2] - \mathbb{E}[X]^2 \\
& \mathbb{E}[X] = \zeta \sum_{k=0}^{\infty} \frac{\gamma^k}{k!} (k+1)^{-(k+2)} \Big(e^{k+1} \, \Gamma(k+1, k+1) + (k+1)^k \Big), \\
& \mathbb{E}[X^2] = \frac{2\zeta}{\beta} \sum_{k=0}^{\infty} \frac{\gamma^k}{k!} (k+1)^{-(k+3)} \Big(e^{k+1} \, \Gamma(k+1, k+1) \; + \; (k+2) \, (k+1)^k \Big), \\
& \zeta = \frac{\gamma \, e^{-\gamma}}{\beta B}, \text{ and } \quad \gamma = \frac{G}{\beta^2}
\end{aligned} \tag{24}$$

If we apply this approximation to our nearest distance distributions, we have to replace just the parameter G. For the distribution of the distance of UE-BS link (12), the parameter G will be given below.

$$G_{UB} = 2\pi\lambda_{BS} \tag{25}$$

For the gamma approximation of pdf of UE-IRS (13) and IRS-BS distances (14), the parameter G in (24) will be as follows,

$$G_{UI} = 2\pi\lambda_b\mu \tag{26}$$

$$G_{IB} = 2\pi\xi\lambda_{BS} \tag{27}$$

Hence, the approximate forms of all the distances are given by,

$$f_{d_{UB}} \approx \tilde{f}_{d_{UB}} \sim \Gamma_X(x; k_d, \theta_d) = \frac{x^{k_d-1}e^{-x/\theta_d}}{\theta_d^{k_d}\Gamma(k_d)} \tag{28}$$

$$f_{d_{UI}} \approx \tilde{f}_{d_{UI}} \sim \Gamma_X(x; k_1, \theta_1) = \frac{x^{k_1-1}e^{-x/\theta_1}}{\theta_1^{k_1}\Gamma(k_1)} \tag{29}$$

$$f_{d_{IB}} \approx \tilde{f}_{d_{IB}} \sim \Gamma_X(x; k_2, \theta_2) = \frac{x^{k_2-1}e^{-x/\theta_2}}{\theta_2^{k_2}\Gamma(k_2)} \tag{30}$$

In order to understand the accuracy of these approximations, we investigated the Kullback–Leibler divergence of the distributions with respect to ρ[6] and μ in Fig.(4.3), (4.4), and (4.5). The sample functions for the values ρ and μ which result in the maximum divergence can be seen in Fig.(4.6), (4.7), and (4.8).

[6]The value ρ indicates the ratio of area covered by buildings, $\rho = \lambda_b\mathbb{E}[L]\mathbb{E}[W]$. For instance, $\rho = 0.25$ means that the buildings cover the quarter of the map area. More details can be found in the Section 5.

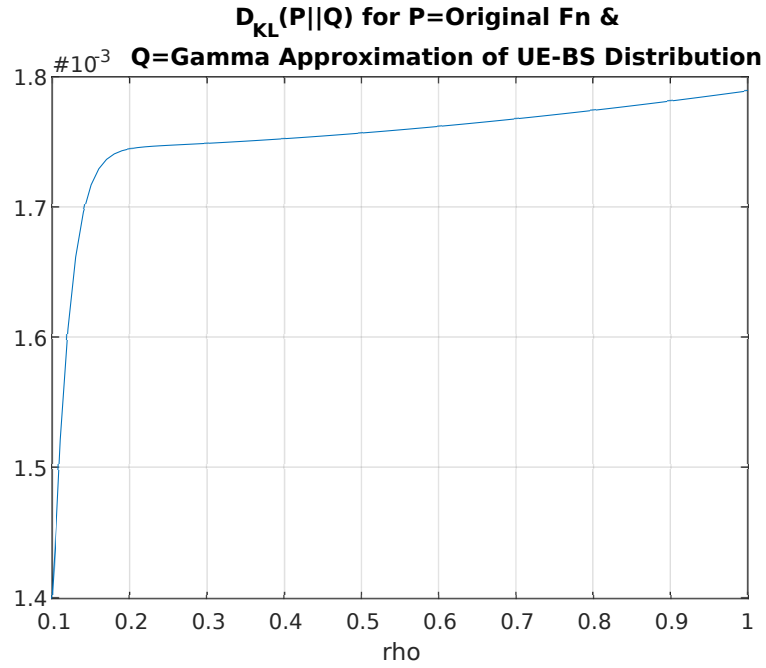

Figure 4.3 Kullback–Leibler divergence of (12) and (18) with (25).

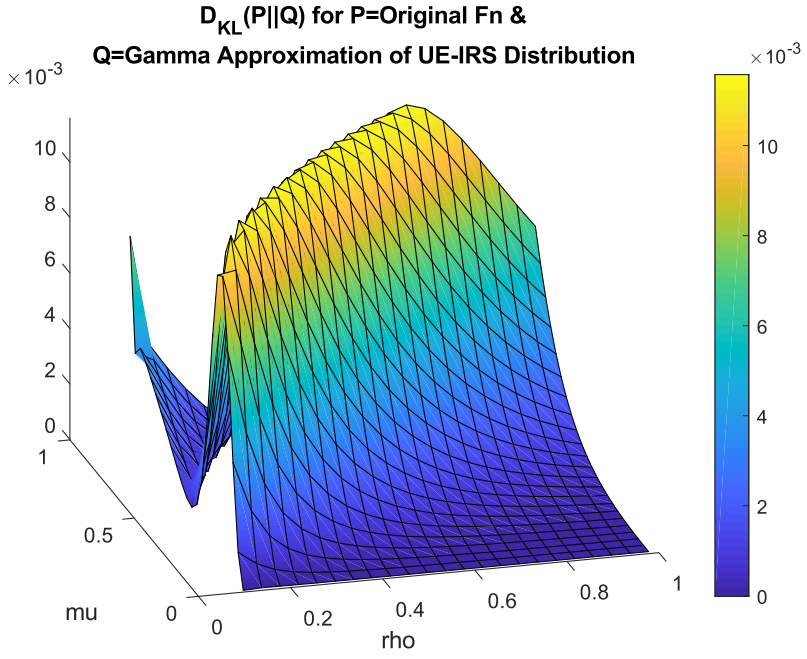

Figure 4.4 Kullback–Leibler divergence of (13) and (18) with (26).

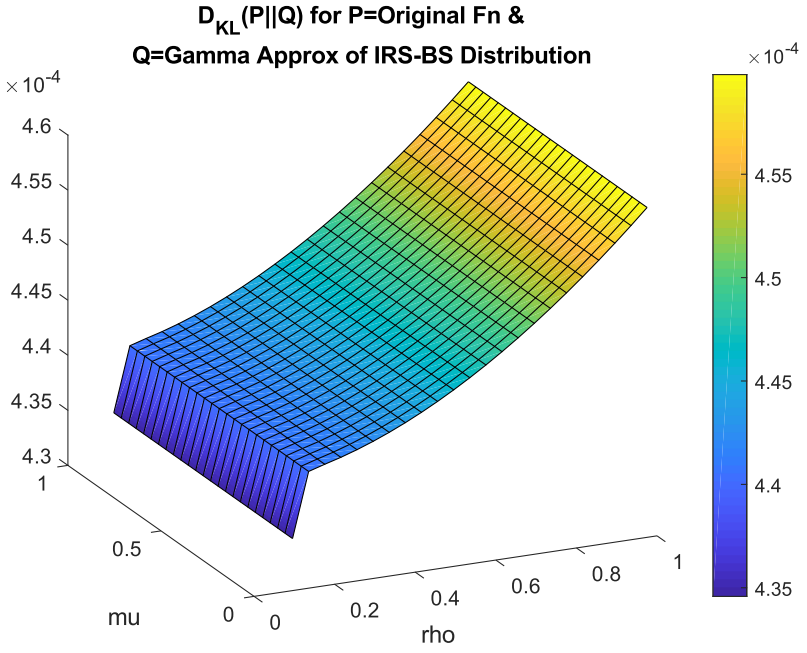

Figure 4.5 Kullback–Leibler divergence of (14) and (18) with (27).

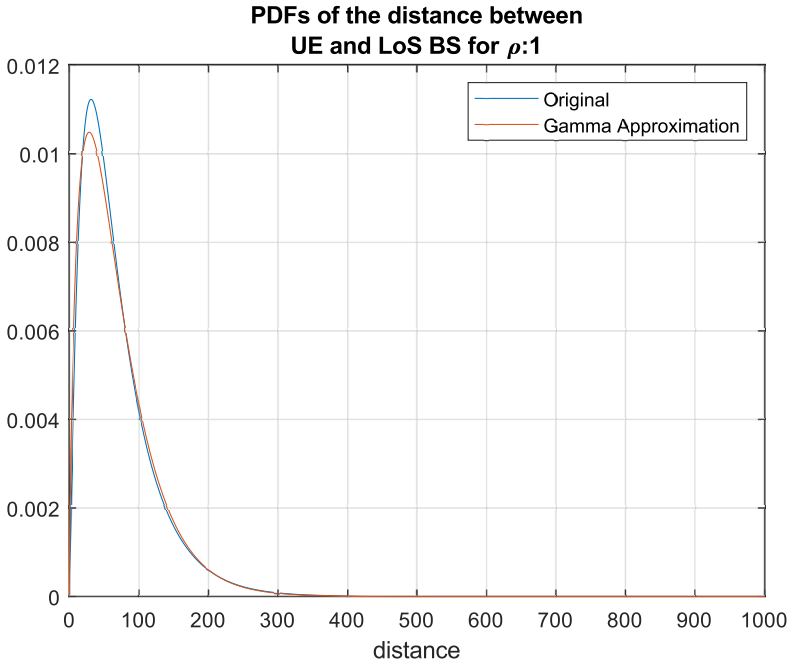

Figure 4.6 PDFs of (12) and (18) with (25) for ρ=1.

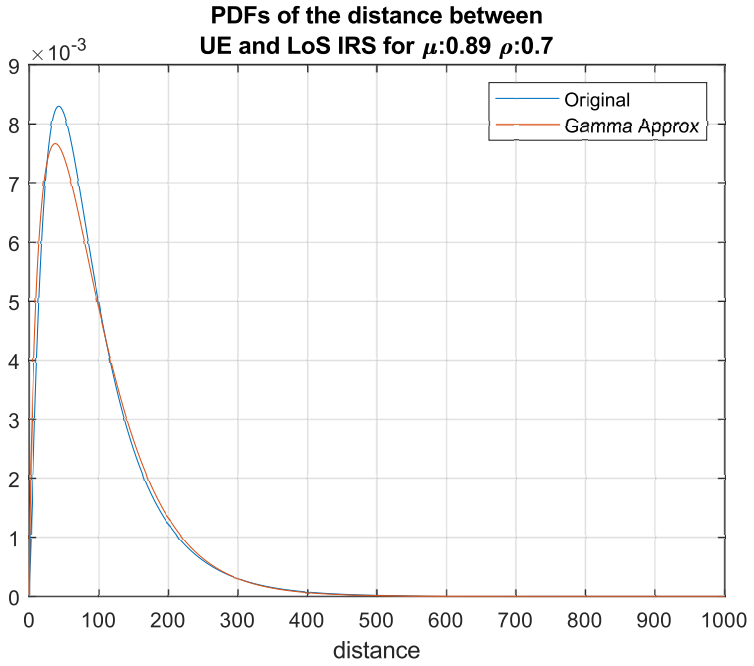

Figure 4.7 PDFs of (13) and (18) with (26) for $\mu = 0.89$ and $\rho = 0.7$.

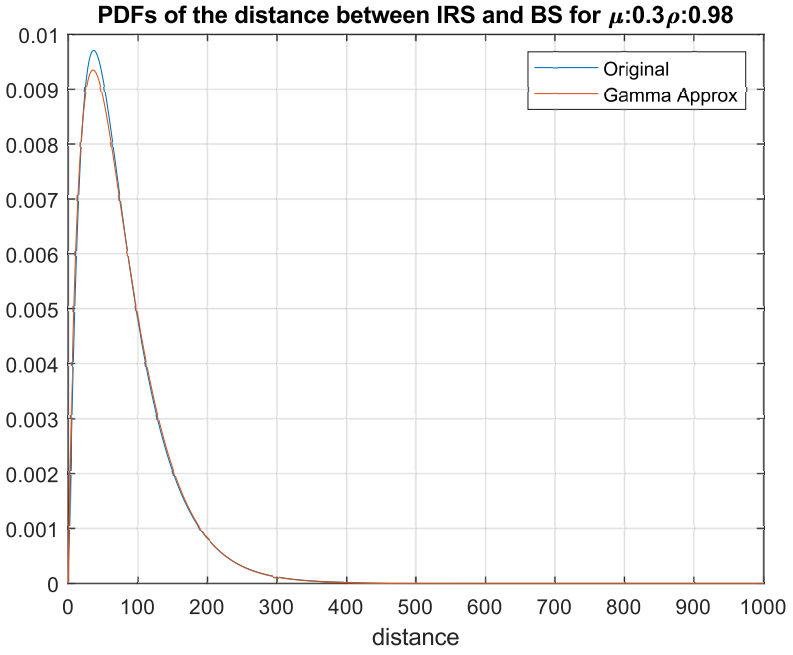

Figure 4.8 PDFs of (14) and (18) with (27) for $\mu = 0.3$ and $\rho = 0.98$.

In [14], the authors propose a LoS ball approximation to the nearest-LoS neighbor distribution. They suggest that the LoS probability equals one for a specific distance R_B, then it is zero for all the values greater than R_B. In other words, they assume that the LoS probability is a step function whose value equals one for a distance R_B. They found this

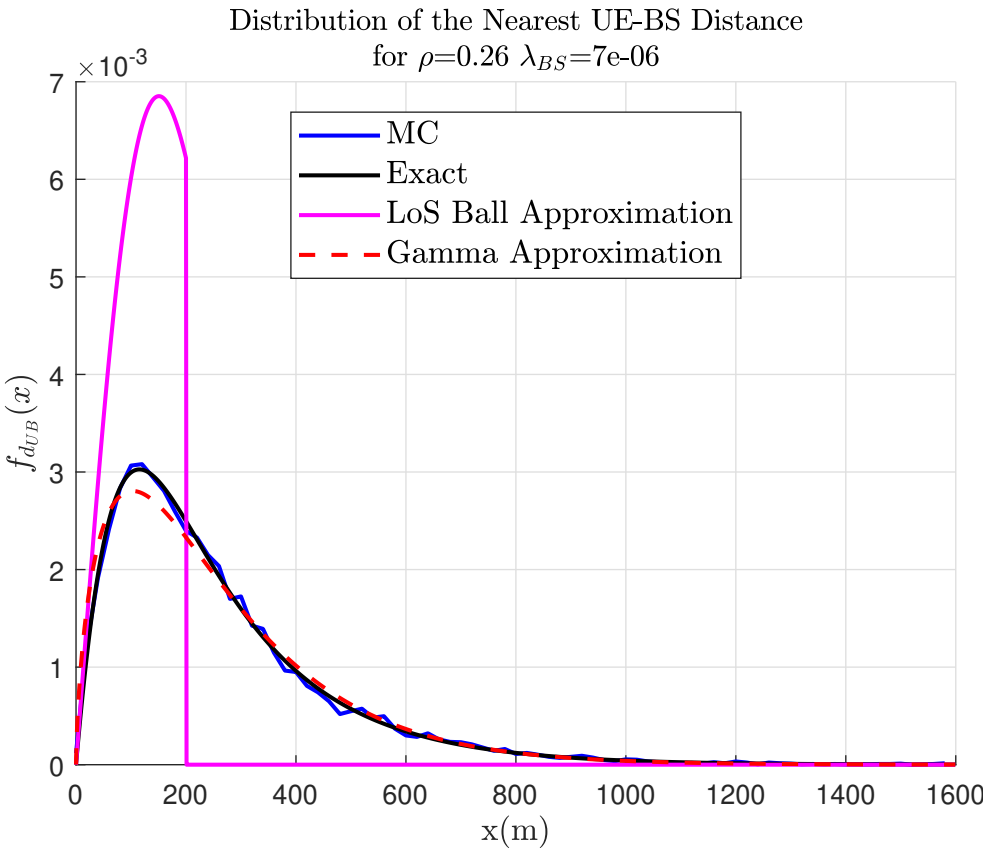

Figure 4.9 Comparing the performance of the LoS ball approximation [14] with our model.

radius as $R_B = (2\int_0^\infty p(t)tdt)^{0.5}$. They call this circle with the center of (0,0) and radius of R_B as LoS ball. We illustrate the performance of this approximation and the comparison with our method in Fig. 4.9. As can be observed, the nearest-LoS neighbor distance equals zero for values greater than R_B (in our case, it is around 200 m). Hence it considerably deviates from the exact distribution for the values lower than 200 and it is not a good fit for exact distribution. On the other hand, our approximation gives quite a close fit to the exact one. Moreover, the figure also shows that the simulation result (MC) also fits both the exact and approximate forms.

4.2.3. Feasible BSs

An indirect link can be created if and only if the TUE and the BS (both are LoS to the IRS) see the same facade of the building in which the IRS is deployed. We call this link as a feasible link, and the BSs satisfy this condition as feasible BSs (in other words, BSs cannot

be located in the region that falls back of the nearest building). Now, we will propose a method to derive the ratio of feasible BSs in a given area.

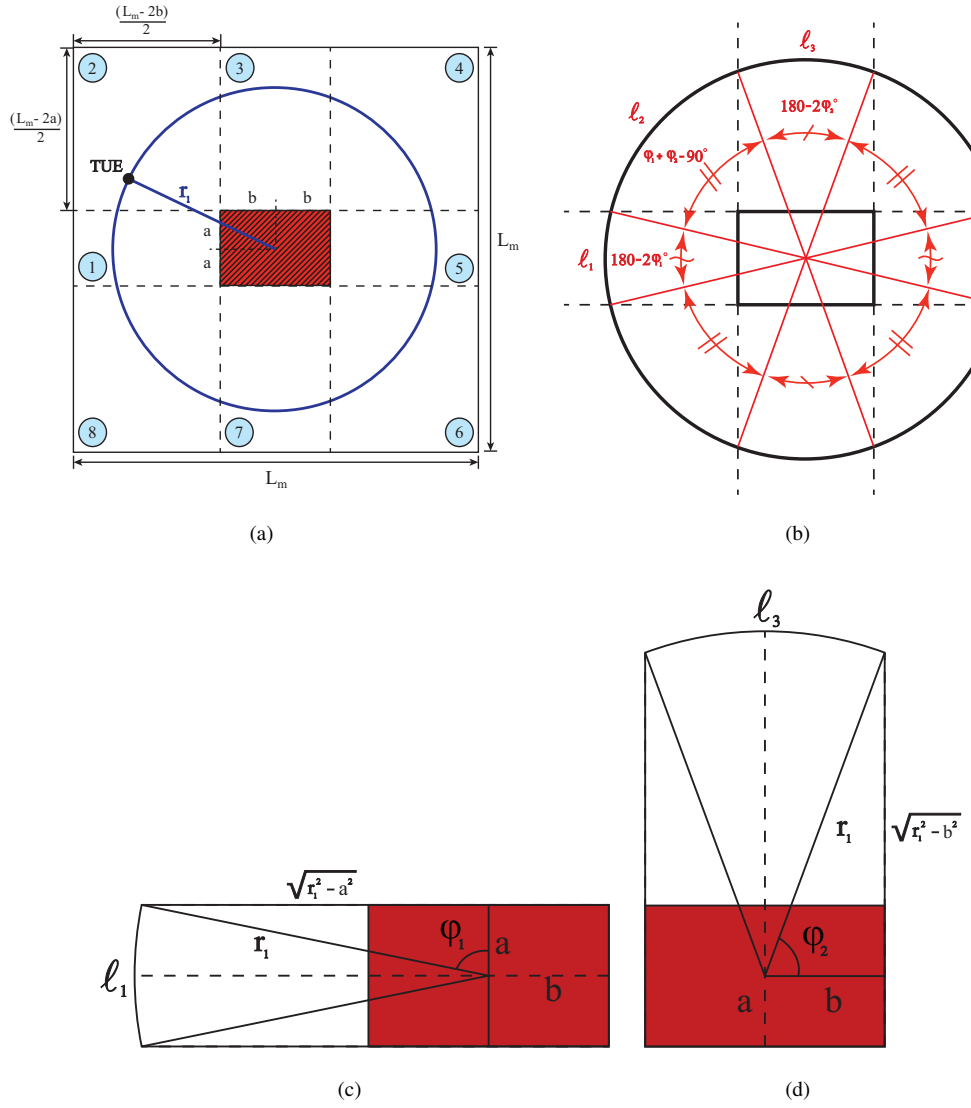

Figure 4.10 Auxiliary figures for the analysis of feasible BSs: (a) The map, the circle which the TUE is located, and 8 different regions which the TUE and BSs can be located. (b) Angle of the regions and related arc lengths. (c) The angle φ_1 for the region 1. (d) The angle φ_2 for the region 3.

Let's consider a square region (in the simulations we take a square map) with its length equal to L_m. We assume that the TUE is connected to the nearest IRS, and we take the center of the building IRS deployed as a reference. In other words, we assume that the building is fixed and TUE can be located anywhere around the circle with the radius r_1 as illustrated in Fig. 4.10 (a) [7]. Since the rotation and placement of the buildings are totally random.

[7]This approximation is better for large values of map length.

Let D : {feasible link} represents the event that a feasible link can be created properly, B_k : {TUE is located on the arc in the k$^{\text{th}}$ region (k$^{\text{th}}$ arc)} is the event that the TUE lies on the arc of the circle with radius r_1 in the k$^{\text{th}}$ region. These arcs, their lengths and related angles can be seen in the Fig. 4.10 (b), and C : {BSs are located in the k$^{\text{th}}$ region} is the event that the BSs are located in the region k of the map, for instance the region-1 has the dimensions of $(2a) \times (L_m - 2b)/2$. For the dimensions of the building, we consider mean values, e.g. $a = \mathbb{E}[W]/2$, and $b = \mathbb{E}[L]/2$. The radius r_1 is the length of the UE-IRS link. Hence, it is distributed with $f_{R_1}(r_1) \sim \tilde{f}_{d_{UI}}(x)$. Now, let's examine the probabilities of these events.

Assume that the r_1 is given. For the probability of the TUE is located on the 1$^{\text{st}}$ arc, we need to find the length of this arc ℓ_1, see the Fig. 4.10 (c). As we can observe,

$$\cos(\varphi_1) = \frac{a}{r_1}$$

$$\varphi_1 = \cos^{-1}\left(\frac{a}{r_1}\right) \tag{31}$$

$$\ell_1 = \frac{\pi - 2\varphi_1}{2\pi}\, 2\pi r_1$$

$$= (\pi - 2\varphi_1) r_1 \tag{32}$$

With the same approach the, we can find the lengths ℓ_2 (from the Fig. 4.10 (d)) and ℓ_3 in the Fig. 4.10 (b). The arc length ℓ_3 is given by

$$\varphi_2 = \cos^{-1}\left(\frac{b}{r_1}\right) \tag{33}$$

$$\ell_3 = \frac{\pi - 2\varphi_2}{2\pi}\, 2\pi r_1$$

$$= (\pi - 2\varphi_2) r_1 \tag{34}$$

and the ℓ_2 can be found by using ℓ_1 and ℓ_2

$$\begin{aligned}
\ell_2 &= \frac{2\pi r_1}{4} - \frac{\ell_1}{2} - \frac{\ell_3}{2} \\
&= \frac{\pi r_1}{2} - \frac{1}{2}((\pi - 2\varphi_2) r_1 + (\pi - 2\varphi_1) r_1) \\
&= \frac{r_1}{2}(\pi - (\pi - 2\varphi_2 + \pi - 2\varphi_1))
\end{aligned}$$

$$= \frac{r_1\pi}{2} - r_1(\pi - \varphi_1 - \varphi_2) \tag{35}$$

Hence, the probability of the events B_k can be found by dividing (32), (35), and (34) by $2\pi r_1$. Since some of the arcs are equal to each other as shown in the Fig. 4.10 (b), we need just three expression as the followings,

$$\mathbb{P}(B_k|r_1) = \begin{cases} \frac{1}{2} - \frac{\varphi_1}{\pi} & , k \in \{1,5\} \\ \frac{1}{4} - \frac{1}{2\pi}(\pi - \varphi_1 - \varphi_2) & , k \in \{2,4,6,9\} \\ \frac{1}{2} - \frac{\varphi_2}{\pi} & , k \in \{3,7\} \end{cases} \tag{36}$$

where $\varphi_1 = \cos^{-1}(a/r_1)$, and $\varphi_2 = \cos^{-1}(b/r_1)$.

Now, let's have a look at the probabilities that the BSs lie in the k[th] region given that the map length L_m. Since the regions are well defined with a,b, and L_m, these probabilities can be found by just using the areas of the rectangular regions. Formally,

$$\mathbb{P}(C_k|L_m) = \begin{cases} \frac{a(L_m-2b)}{L_m^2} & , k \in \{1,5\} \\ \frac{(L_m-2b)}{2}\frac{(L_m-2a)}{2}\frac{1}{L_m^2} & , k \in \{2,4,6,9\} \\ \frac{b(L_m-2a)}{L_m^2} & , k \in \{3,7\} \end{cases} \tag{37}$$

where these events are mutually exclusive.

If the TUE is located on the 1[st] arc, the feasbile link can be created if and only if the BSs lie in the regions 1,2, and 8. Hence the probability of a BS is a feasible BS given that the TUE is in region 1 is given by,

$$\begin{aligned} \mathbb{P}(D|B_1, L_m) &= \mathbb{P}(C_1|L_m) + \mathbb{P}(C_2|L_m) + \mathbb{P}(C_8|L_m) \\ &= \mathbb{P}(C_1|L_m) + 2\mathbb{P}(C_2|L_m) \end{aligned}$$

If the TUE is located in the 2nd arc, BSs have to be in the regions 1,2,3,4, and 8. If it lies in the 3rd arc, then BSs have to be in the regions 2,3, and 4. Hence the probability of feasible BSs given the TUE lies in the kth arc can be stated as

$$\mathbb{P}(D|B_k, L_m) = \begin{cases} \mathbb{P}(C_1|L_m) + 2\mathbb{P}(C_2|L_m) & , k \in \{1, 5\} \\ \mathbb{P}(C_1|L_m) + 3\mathbb{P}(C_2|L_m) + \mathbb{P}(C_3|L_m) & , k \in \{2, 4, 6, 9\} \\ 2\mathbb{P}(C_2|L_m) + 2\mathbb{P}(C_3|L_m) & , k \in \{3, 7\} \end{cases} \tag{38}$$

Hence the probability that a BS is a feasible BS given that the map length as follows,

$$\begin{aligned} \mathbb{P}(D|L_m) &= \sum_{k=1}^{8} \mathbb{P}(D|B_k, L_m)\, \mathbb{P}(B_k|L_m) \\ &= \sum_{k=1}^{8} \mathbb{P}(D|B_k, L_m) \int_0^\infty \mathbb{P}(B_k|L_m, r_1)\, f_{R_1}(r_1)\, dr_1 \\ &= 2\mathbb{P}(D|B_1, L_m) \int_0^\infty \mathbb{P}(B_1|L_m, r_1)\, f_{R_1}(r_1)\, dr_1 + \\ &\quad 4\mathbb{P}(D|B_2, L_m) \int_0^\infty \mathbb{P}(B_2|L_m, r_1)\, f_{R_1}(r_1)\, dr_1 + \\ &\quad 2\mathbb{P}(D|B_3, L_m) \int_0^\infty \mathbb{P}(B_3|L_m, r_1)\, f_{R_1}(r_1)\, dr_1 \\ &= \xi \end{aligned} \tag{39}$$

Since all components of (39) are given, it can be computed numerically and we call this number as ξ.

4.2.4. Indirect LoS link's Product-Distance Distribution

As we mentioned before, we can find the distribution of the product distance by multiplicative convolution. However, the expression in 15 is too complicated to reduce to a closed-form. In the Section 4.2.2., we derive the gamma approximation of pdfs of individual links'. Hence, by using these approximate forms, we can get a closed-form expression for the product

distance distribution. To do that, we will use the multiplicative convolution property of Mellin Transform (MT) as given below.

Theorem 0.2 ([51])**.** *The Mellin Transform of the multiplicative convolution of functions Z_1 and Z_2 is equal to the product of their Mellin transforms (MTs):*

$$\mathcal{M}[Z_1 \vee Z_2](s) = \mathcal{M}[Z_1](s)\mathcal{M}[Z_2](s) \tag{40}$$

where $\mathcal{M}[f](s) = \int_0^\infty x^{s-1} f(x)\, dx$, denotes the MT.

Now, let's use the theorem 0.2 to derive $f_I(z)$.

$$\begin{aligned}
f_I(z) \approx \tilde{f}_I(z) &= \int_0^\infty \tilde{f}_{d_{UI}}(x)\tilde{f}_{d_{IB}}\left(\frac{1}{x}\right)\frac{1}{x}\, dx \\
&= \tilde{f}_{d_{UI}}(x) \vee \tilde{f}_{d_{IB}}(x) \\
\mathcal{M}[\tilde{f}_{d_{UI}}(x) \vee \tilde{f}_{d_{IB}}(x)](s) &= \mathcal{M}[\tilde{f}_{d_{UI}}(x)](s)\, \mathcal{M}[\tilde{f}_{d_{IB}}(x)](s) \\
\tilde{f}_I(z) &= \mathcal{M}^{-1}[\mathcal{M}[\tilde{f}_I(z)]] \\
&= \mathcal{M}^{-1}[\mathcal{M}[\tilde{f}_{d_{UI}}(x) \vee \tilde{f}_{d_{IB}}(x)]] \\
&= \mathcal{M}^{-1}[\mathcal{M}[\tilde{f}_{d_{UI}}(x)]\, \mathcal{M}[\tilde{f}_{d_{IB}}(x)]]]
\end{aligned} \tag{41}$$

where $\mathcal{M}^{-1}$ denotes inverse MT (IMT).

To derive the closed-form equation of (41), we need to find the the MT of UE-IRS and IRS-BS links' distributions, then the IMT of multiplication of these transforms gives us the product distance distribution.

$$\begin{aligned}
\mathcal{M}[\tilde{f}_{d_{UI}}(x)](w) &= \int_0^\infty x^{w-1} \frac{x^{k_1-1}\, e^{-x/\theta_1}}{\theta_1^{k-1}\, \Gamma(k_1)}\, dx \\
&= \frac{1}{\theta_1^{k_1}\, \Gamma(k_1)} \int_0^\infty x^{w+k_1-2}\, e^{-x/\theta_1}\, dx \\
&\overset{(a)}{=} \frac{1}{\theta_1^{k_1}\, \Gamma(k_1)} \int_0^\infty (\theta_1\, u)^{w+k_1-2}\ \ e^{-u}\, \theta_1\, du \\
&= \frac{\theta_1^{w+k_1-2}\theta_1}{\theta_1^{k_1}\, \Gamma(k_1)} \int_0^\infty u^{w+k_1-2} e^{-u}\, du \\
&= \frac{\theta_1^{w-1}}{\Gamma(k_1)}\, \Gamma(w + k_1 - 1)
\end{aligned}$$

$$= \frac{\theta_1^{-1}}{\Gamma(k_1)}\,\theta_1^w \Gamma(w+k_1-1) \tag{42}$$

where we employed change of variable $x = u\,\theta_1$ in (a). In the same manner,

$$\mathcal{M}[\tilde{f}_{d_{IB}}(x)](w) = \frac{\theta_2^{-1}}{\Gamma(k_2)}\,\theta_2^w\,\Gamma(w+k_2-1) \tag{43}$$

If we substitute (42) and (43) into (41), we get,

$$\begin{aligned}
\tilde{f}_I(z) &= \mathcal{M}^{-1}\left[\frac{(\theta_1\,\theta_2)^{-1}}{\Gamma(k_1)\,\Gamma(k_2)}(\theta_1\,\theta_2)^w\,\Gamma(w+k_2-1)\,\Gamma(w+k_1-1)\right] \\
&= \frac{(\theta_1\,\theta_2)^{-1}}{\Gamma(k_1)\,\Gamma(k_2)}\mathcal{M}^{-1}[(\theta_1\,\theta_2)^w\,\Gamma(w+k_2-1)\,\Gamma(w+k_1-1)] \\
&= \frac{\theta_m^{-1}}{\Gamma(k_1)\,\Gamma(k_2)}\mathcal{M}^{-1}[\theta_m^w\,\Gamma(w-\alpha_1)\,\Gamma(w-\alpha_2)]
\end{aligned}$$

where $\theta_m = \theta_1\,\theta_2$, $\alpha_1 = 1-k_1$, and $\alpha_2 = 1-k_2$.

Let $\Phi(w) = \Gamma(w-\alpha_1)\,\Gamma(w-\alpha_2)$, and $\Phi(z) = \mathcal{M}^{-1}[\Phi(w)]$,

$$\begin{aligned}
\tilde{f}_I(z) &= \frac{\theta_m^{-1}}{\Gamma(k_1)\,\Gamma(k_2)}\mathcal{M}^{-1}\left[(\frac{1}{\theta_m})^{-w}\,\Phi(w)\right] \\
&\overset{\text{(a)}}{=} \frac{\theta_m^{-1}}{\Gamma(k_1)\,\Gamma(k_2)}\Phi\left(\frac{z}{\theta_m}\right) \\
&\overset{\text{(b)}}{=} \frac{\theta_m^{-1}}{\Gamma(k_1)\,\Gamma(k_2)}\,2\left(\frac{z}{\theta_m}\right)^{-\frac{(\alpha_1+\alpha_2)}{2}} K_{\alpha_2-\alpha_1}\left(2\sqrt{\frac{z}{\theta_m}}\right) \\
&= \frac{2\,\theta_m^{-k_t}}{\Gamma(k_1)\,\Gamma(k_2)}z^{k_t-1}\,K_{k_1-k_2}\left(2\sqrt{\frac{z}{\theta_m}}\right)
\end{aligned} \tag{44}$$

where, $k_t = (k_1+k_2)/2$, and in step (a), we used the fact that $\mathcal{M}^{-1}[a^{-w}\Phi(w)] = \Phi(az)$ ([52], p.163), and in the step (b) $\mathcal{M}^{-1}[\Gamma(\alpha+w)\,\Gamma(\beta+w)] = 2z^{\frac{(\alpha+\beta)}{2}}K_{\alpha-\beta}(2\sqrt{z})$([52], p.196) as follows,

$$\mathcal{M}^{-1}\left[(\frac{1}{\theta_m})^{-w}\,\Phi(w)\right] = \Phi\left(\frac{z}{\theta_m}\right)$$

$$\Phi(z) = \mathcal{M}^{-1}[\Gamma(w-\alpha_1)\,\Gamma(w-\alpha_2)]$$

$$= 2\ z^{\frac{1}{2}(-\alpha_1-\alpha_2)}\ K_{-\alpha_1+\alpha_2}(2\sqrt{z})$$

$$\mathcal{M}^{-1}\left[(\frac{1}{\theta_m})^{-w}\ \Phi(w)\right] = 2\ \left(\frac{z}{\theta_m}\right)^{\frac{1}{2}(-\alpha_1-\alpha_2)}\ K_{-\alpha_1+\alpha_2}\left(2\sqrt{\frac{z}{\theta_m}}\right)$$

where $K(z) = \frac{\pi}{2}\frac{I_{-n}(z)-I_n(z)}{sin(n\pi)}$, is the modified Bessel function of second kind, and $I_\nu(z) = (\frac{z}{2})^\nu\ \sum_{k=0}^{\infty}\frac{(z^2/4)^k}{k!\ \Gamma(\nu+k+1)}$ is the modified Bessel function of first kind. If we substitute the series expansion of Bessel functions into the (44), we get,

$$\begin{aligned}
\tilde{f}_I(z) &= \frac{2\theta_m^{-k_t}}{\Gamma(k_1)\ \Gamma(k_2)}\ z^{k_t-1}\ K_{k_1-k_2}\left(2\sqrt{\frac{z}{\theta_m}}\right) \\
&= \frac{2\theta_m^{k_t}}{\Gamma(k_1)\ \Gamma(k_2)}\ z^{k_t-1}\left[\frac{\pi}{2sin(n\pi)}\left(\left(2\sqrt{\frac{z}{\theta_m}}\frac{1}{2}\right)^{-n}\sum_{k=0}^{\infty}\frac{(\frac{4z}{4\theta_m})^k}{k!\ \Gamma(-n+k+1)} - \right.\right. \\
&\qquad \left.\left.\left(2\sqrt{\frac{z}{\theta_m}}\frac{1}{2}\right)^{n}\sum_{k=0}^{\infty}\frac{(\frac{4z}{4\theta_m})^k}{k!\ \Gamma(n+k+1)}\right)\right] \\
&= \frac{2\theta_m^{k_t}}{\Gamma(k_1)\ \Gamma(k_2)}\ z^{k_t-1}\ \frac{\pi}{2sin(n\pi)}\left[\left(\frac{z}{\theta_m}\right)^{-n/2}\sum_{k=0}^{\infty}\frac{(z/\theta_m)^k}{k!\ \Gamma(-n+k+1)} - \right. \\
&\qquad \left.\left(\frac{z}{\theta_m}\right)^{n/2}\sum_{k=0}^{\infty}\frac{(z/\theta_m)^k}{k!\ \Gamma(n+k+1)}\ \right] \\
&= \Lambda_1\ z^{k_t-1}\ \left[\left(\frac{z}{\theta_m}\right)^{-n/2}\sum_{k=0}^{\infty}\frac{(z/\theta_m)^k}{k!\ \Gamma(-n+k+1)} - \left(\frac{z}{\theta_m}\right)^{n/2}\sum_{k=0}^{\infty}\frac{(z/\theta_m)^k}{k!\ \Gamma(n+k+1)}\ \right]
\end{aligned} \tag{45}$$

where $\Lambda_1 = \frac{\theta_m^{-k_t}\pi}{\Gamma(k_1)\ \Gamma(k_2)\ sin(\pi n)}$, and $n = k_1 - k_2$.

Now, let's investigate how the gamma approximation of $f_I(z)$ is close to the exact form (eqn.(17) and (45)) in figure (4.11),

4.2.5. Conditional Distribution of Nearest Distances

In the beginning of the section, we mentioned that the coverage analysis is investigated with four different events (11). In this section, we will give the conditional distribution of nearest distances but first let's examine the probability of these four events. Let,

$$\mathbb{P}(A_{D,PL}) = \mathbb{P}\{PL_D \leq PL_I\}, \tag{46}$$

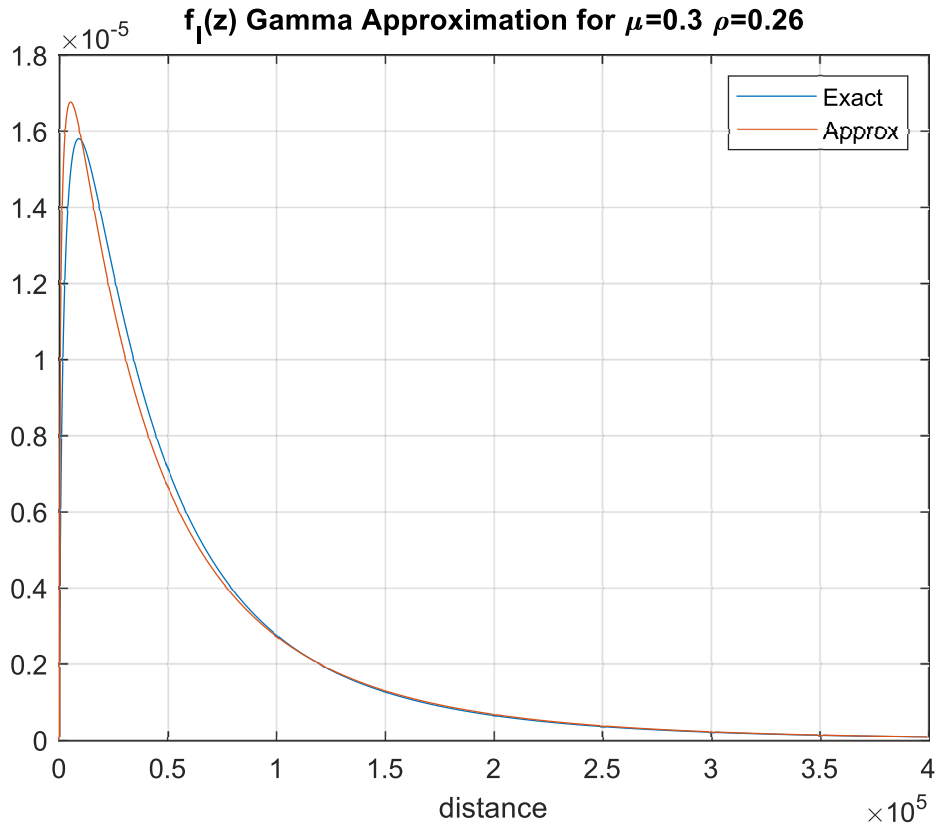

Figure 4.11 Comparison of (17) and (45) for $\mu = 0.3$ and $\rho = 0.26$.

$$\mathbb{P}(A_{I,PL}) = \mathbb{P}\{PL_I < PL_D\}, \tag{47}$$

$$\begin{aligned}\mathbb{P}(A_D^{'}) &= \mathbb{P}\{\textit{TUE cannot reach any direct LoS BS}\},\\ &\overset{(a)}{=} \exp(-\int_0^{2\pi}\int_0^{\infty} \lambda_{BS}\, p(r) r\, dr\, d\theta),\\ &= \exp(-2\pi\lambda_{BS}/\beta^2)\end{aligned} \tag{48}$$

$$\begin{aligned}\mathbb{P}(A_I^{'}) &= \mathbb{P}\{\textit{TUE cannot reach any LoS IRS}\}\\ &\overset{(b)}{=} \exp(-2\pi\lambda_b\mu/\beta^2),\end{aligned} \tag{49}$$

$$\begin{aligned}\mathbb{P}(A_I^{''}) &= \mathbb{P}\{\textit{The IRS cannot reach any LoS BS}\}\\ &\overset{(c)}{=} \exp(-2\pi\xi\lambda_{BS}/\beta^2)\end{aligned} \tag{50}$$

where we used the null (or void) probability of a PPP [15] in the steps (a), (b), and (c). Hence,

$$\begin{aligned}\mathbb{P}(\hat{A}_I) &= \mathbb{P}\{\textit{TUE cannot reach any indirect LoS BS}\} \\ &= \mathbb{P}(A_I^{'} \cup A_I^{''}) \\ &= \mathbb{P}(A_I^{'}) + \mathbb{P}(A_I^{''}) - \mathbb{P}(A_I^{'}) \cdot \mathbb{P}(A_I^{''})\end{aligned} \tag{51}$$

Note that the events $A_I^{'}$ and $A_I^{''}$ are not mutually exclusive. By using the definitions in (46) - (50), and (51),

$$\begin{aligned}\mathbb{P}(A_{D1}) &= \mathbb{P}(A_{D,PL} \cap \overline{A_D^{'}} \cap \overline{\hat{A}_I}) \\ &= \mathbb{P}(A_{D,PL})\, \mathbb{P}(\overline{A_D^{'}})\, \mathbb{P}(\overline{\hat{A}_I}) \qquad (52) \\ \mathbb{P}(A_{D2}) &= \mathbb{P}(\overline{A_D^{'}} \cap \hat{A}_I) \\ &= \mathbb{P}(\overline{A_D^{'}})\, \mathbb{P}(\hat{A}_I) \qquad (53) \\ \mathbb{P}(A_{I1}) &= \mathbb{P}(A_{I,PL} \cap \overline{A_D^{'}} \cap \overline{\hat{A}_I}) \\ &= \mathbb{P}(A_{I,PL})\, \mathbb{P}(\overline{A_D^{'}})\, \mathbb{P}(\overline{\hat{A}_I}) \qquad (54) \\ \mathbb{P}(A_{I2}) &= \mathbb{P}(A_D^{'} \cap \overline{\hat{A}_I}) \\ &= \mathbb{P}(A_D^{'})\, \mathbb{P}(\overline{\hat{A}_I}) \qquad (55)\end{aligned}$$

where $\overline{(\cdot)}$, indicates the complement of an event(e.g. $\mathbb{P}(\overline{A}) = 1 - \mathbb{P}(A)$).

Now, we can derive the conditional distributions of nearest distances. For the events A_{D2} and A_{I2} (only the direct link, and only the indirect link), conditional distributions $f_D(x|A_{D2})$ and $f_I(z|A_{I2})$ will be equal to the unconditional ones. We can observe this from the Bayesian expansion.

$$\begin{aligned}f_D(x|A_{D2}) &= \frac{\mathbb{P}(A_{D2}\,|x)\; f_{d_{UB}}(x)}{\int_0^\infty \mathbb{P}(A_{D2}\,|x)\; f_{d_{UB}}(x)\, dx} \qquad (56) \\ &= \frac{\mathbb{P}(\overline{A_D^{'}}\,|x)\, \mathbb{P}(\hat{A}_I\,|x)\; f_{d_{UB}}(x)}{\int_0^\infty \mathbb{P}(\overline{A_D^{'}}\,|x)\, \mathbb{P}(\hat{A}_I\,|x)\; f_{d_{UB}}(x)\, dx} \\ &= \frac{\mathbb{P}(\overline{A_D^{'}})\, \mathbb{P}(\hat{A}_I)\; f_{d_{UB}}(x)}{\mathbb{P}(\overline{A_D^{'}})\, \mathbb{P}(\hat{A}_I)\; \int_0^\infty f_{d_{UB}}(x)\, dx} \\ &= f_{d_{UB}}(x) \\ &\approx \tilde{f}_{d_{UB}}(x) \qquad (57)\end{aligned}$$

The variable x in (56) represents the nearest LoS BS distance. Since the probability that the UE sees just direct LoS BSs is independent of the nearest LoS BSs distance, $f_D(x|A_{D2})$ will be equal to $f_{d_{UB}}(x)$. In the same way, $f_I(z|A_{I2}) = f_I(z) \approx \tilde{f}_I(z)$. For the rest of the two conditional distributions for A_{D1} and A_{I1}, we will use Bayes theorem.

$$\begin{aligned}
f_D(x|A_{D1}) &= \frac{\mathbb{P}(A_{D1}\,|x)\; f_{d_{UB}}(x)}{\int_0^\infty \mathbb{P}(A_{D1}\,|x)\; f_{d_{UB}}(x)\, dx} \\
&= \frac{\mathbb{P}(A_{D,PL}\,|x)\; \mathbb{P}(\overline{A'_D}\,|x)\; \mathbb{P}(\overline{\hat{A}_I}\,|x)\; f_{d_{UB}}(x)}{\int_0^\infty \mathbb{P}(A_{D,PL}\,|x)\; \mathbb{P}(\overline{A'_D}\,|x)\; \mathbb{P}(\overline{\hat{A}_I}\,|x)\; f_{d_{UB}}(x)\, dx} \\
&= \frac{\mathbb{P}(PL_D(x) \leq PL_I\,|x)\; \mathbb{P}(\overline{A'_D})\; \mathbb{P}(\overline{\hat{A}_I})\; f_{d_{UB}}(x)}{\mathbb{P}(\overline{A'_D})\; \mathbb{P}(\overline{\hat{A}_I})\; \int_0^\infty \mathbb{P}(PL_D(x) \leq PL_I\,|x)\; f_{d_{UB}}(x)\, dx} \\
&= \frac{\mathbb{P}(PL_D(x) \leq PL_I\,|x)\; f_{d_{UB}}(x)}{\int_0^\infty \mathbb{P}(PL_D(x) \leq PL_I\,|x)\; f_{d_{UB}}(x)\, dx} \\
&\approx \frac{\mathbb{P}(PL_D(x) \leq PL_I\,|x)\; \tilde{f}_{d_{UB}}(x)}{\int_0^\infty \mathbb{P}(PL_D(x) \leq PL_I\,|x)\; \tilde{f}_{d_{UB}}(x)\, dx}
\end{aligned} \tag{58}$$

With the same approach,

$$\begin{aligned}
f_I(z|A_{I1}) &= \frac{\mathbb{P}(PL_I(z) < PL_D\,|z)\; f_I(z)}{\int_0^\infty \mathbb{P}(PL_I(z) < PL_D\,|z)\; f_I(z)\, dz} \\
&\approx \frac{\mathbb{P}(PL_I(z) < PL_D\,|z)\; \tilde{f}_I(z)}{\int_0^\infty \mathbb{P}(PL_I(z) < PL_D\,|z)\; \tilde{f}_I(z)\, dz}
\end{aligned} \tag{59}$$

Now, we need find the conditional probabilities in (58) and (59) but first, we need to find the CDFs of nearest direct link distance and the product distance. Since we approximate the pdf in (12) with a gamma pdf (28), the CDF of the nearest direct LoS BS distance will be,

$$\tilde{F}_{d_{UB}}(x\,|k_d, \theta_D) = \frac{1}{\Gamma(k_D)} \gamma(k_D, \frac{x}{\theta_D}) \tag{60}$$

where $\gamma(s, x) = \int_0^x t^{s-1}\; e^{-t}$, is the lower incomplete gamma function.

For the CDF of nearest indirect link distance, we use (45)

$$\begin{aligned}
\tilde{F}_I(z) &= \int_0^z \tilde{f}_I(\tau)\, d\tau \\
&= \int_0^z \Lambda_1\; \tau^{k_t - 1} \left[\left(\frac{\tau}{\theta_m} \right)^{-n/2} \sum_{k=0}^{\infty} \frac{(\tau/\theta_m)^k}{k!\; \Gamma(-n + k + 1)} - \right.
\end{aligned}$$

$$\left(\frac{\tau}{\theta_m}\right)^{n/2} \sum_{k=0}^{\infty} \frac{(\tau/\theta_m)^k}{k!\,\Gamma(n+k+1)} \Bigg] d\tau$$

$$= \Lambda_1 \Bigg[\theta_m^{n/2} \sum_{k=0}^{\infty} \frac{\theta_m^{-k}}{k!\,\Gamma(-n+k+1)} \int_0^z \tau^{k-n/2+k_t-1}\, d\tau - \theta_m^{-n/2} \sum_{k=0}^{\infty} \frac{\theta_m^{-k}}{k!\,\Gamma(n+k+1)} \int_0^z \tau^{k+n/2+k_t-1}\, d\tau \Bigg]$$

$$= \Lambda_1 \Bigg[\theta_m^{n/2} \sum_{k=0}^{\infty} \frac{\theta_m^{-k}}{k!\,\Gamma(-n+k+1)} \frac{z^{k+k_2}}{(k+k_2)} - \theta_m^{-n/2} \sum_{k=0}^{\infty} \frac{\theta_m^{-k}}{k!\,\Gamma(n+k+1)} \frac{z^{k+k_1}}{(k+k_1)} \Bigg] \tag{61}$$

where $\Lambda_1 = \frac{\theta_m^{-k_t}\pi}{\Gamma(k_1)\ \Gamma(k_2)\ sin(\pi n)}$, and $n = k_1 - k_2$, $k_t = \frac{k_1+k_2}{2}$, and $\theta_m = \theta_1\ \theta_2$.

Hence, the conditional probabilities in (58) and (59) can be found by using the following probabilities.

$$\begin{aligned}
\mathbb{P}(PL_D(x) \le PL_I\ |x) &= \mathbb{P}\left(\frac{x^2}{C} \le \frac{1}{C} \left(\frac{2Z}{N\lambda\ \cos\theta_i} \right)^2 \ \Big| x \right) \\
&= \mathbb{P}(Z^2 \ge (x\ N\lambda\ \cos\theta_i/2)^2\ |x) \\
&= \mathbb{P}(Z^2 \ge \Psi^2(x,\theta_i)\ |x) \\
&= \mathbb{P}\left(|Z| \ge |\Psi(x,\theta_i)|\ |x\right) \\
&\overset{(a)}{=} \mathbb{P}\left(Z \ge \Psi(x,\theta_i)\ |x\right) \\
&= \int_0^{\pi/2} \mathbb{P}(Z \ge \Psi(x,\theta_i)\ |x,\theta_i)\ \frac{2}{\pi}\, d\theta_i \\
&\overset{(b)}{=} \int_0^{\pi/2} \left(1 - \tilde{F}_I(\Psi(x,\theta_i))\right)\ \frac{2}{\pi}\, d\theta_i \\
&= 1 - \int_0^{\pi/2} \tilde{F}_I(\Psi(x,\theta_i))\ \frac{2}{\pi}\, d\theta_i \\
&= 1 - \int_0^{\pi/2} \Lambda_1 \Bigg[\theta_m^{n/2} \sum_{k=0}^{\infty} \frac{\theta_m^{-k}}{k!\,\Gamma(-n+k+1)} \frac{\left(\Psi(x,\theta_i)\right)^{k+k_2}}{k+k_2} - \\
&\qquad \theta_m^{-n/2} \sum_{k=0}^{\infty} \frac{\theta_m^{-k}}{k!\,\Gamma(n+k+1)} \frac{\left(\Psi(x,\theta_i)\right)^{k+k_1}}{k+k_1} \Bigg]\ \frac{2}{\pi}\, d\theta_i \\
&= 1 - \frac{2\Lambda_1}{\pi} \Bigg[\theta_m^{n/2} \sum_{k=0}^{\infty} \frac{\theta_m^{-k}}{k!\,\Gamma(-n+k+1)\ (k+k_2)}
\end{aligned}$$

$$
\begin{aligned}
&\int_0^{\pi/2} (xN\lambda\ \cos\theta_i/2)^{k+k_2}\, d\theta_i - \\
&\theta_m^{-n/2} \sum_{k=0}^{\infty} \frac{\theta_m^{-k}}{k!\,\Gamma(n+k+1)\,(k+k_1)} \\
&\int_0^{\pi/2} (xN\lambda\ \cos\theta_i/2)^{k+k_1}\, d\theta_i \Bigg] \\
= 1 - \frac{2\Lambda_1}{\pi} &\Bigg[\theta_m^{n/2} \sum_{k=0}^{\infty} \frac{\theta_m^{-k}\,(xN\lambda\,/2)^{k+k_2}}{k!\,\Gamma(-n+k+1)\,(k+k_2)} \\
&\int_0^{\pi/2} \cos^{k+k_2}(\theta_i)\, d\theta_i - \\
&\theta_m^{-n/2} \sum_{k=0}^{\infty} \frac{\theta_m^{-k}\,(xN\lambda\,/2)^{k+k_1}}{k!\,\Gamma(n+k+1)\,(k+k_1)} \\
&\int_0^{\pi/2} \cos^{k+k_1}(\theta_i)\, d\theta_i \Bigg] \\
\overset{(c)}{=} 1 - \frac{2\Lambda_1}{\pi} &\Bigg[\theta_m^{n/2} \sum_{k=0}^{\infty} \frac{\theta_m^{-k}\,(xN\lambda\,/2)^{k+k_2}}{k!\,\Gamma(-n+k+1)\,(k+k_2)} \frac{\sqrt{\pi}}{2} \\
&\frac{\Gamma\left(\frac{k+k_2+1}{2}\right)}{\Gamma\left(\frac{k+k_2}{2}+1\right)} - \\
&\theta_m^{-n/2} \sum_{k=0}^{\infty} \frac{\theta_m^{-k}\,(xN\lambda\,/2)^{k+k_1}}{k!\,\Gamma(n+k+1)\,(k+k_1)} \frac{\sqrt{\pi}}{2} \frac{\Gamma\left(\frac{k+k_1+1}{2})\right)}{\Gamma\left(\frac{k+k_1}{2}+1\right)}\Bigg] \\
= 1 - \frac{\Lambda_1}{\sqrt{\pi}} &\Bigg[\sum_{k=0}^{\infty} \frac{\theta_m^{-k+n/2}\,(xN\lambda\,/2)^{k+k_2}}{k!\,\Gamma(-n+k+1)\,(k+k_2)} \frac{\Gamma\left(\frac{k+k_2+1}{2}\right)}{\Gamma\left(\frac{k+k_2}{2}+1\right)} - \\
&\sum_{k=0}^{\infty} \frac{\theta_m^{-(k+n/2)}\,(xN\lambda\,/2)^{k+k_1}}{k!\,\Gamma(n+k+1)\,(k+k_1)} \frac{\Gamma\left(\frac{k+k_1+1}{2})\right)}{\Gamma\left(\frac{k+k_1}{2}+1\right)}\Bigg] \\
= 1 - \frac{\Lambda_1}{\sqrt{\pi}} &\sum_{k=0}^{\infty} \Bigg[\frac{\theta_m^{-k+n/2}\,(xN\lambda\,/2)^{k+k_2}}{k!\,\Gamma(-n+k+1)\,(k+k_2)} \frac{\Gamma\left(\frac{k+k_2+1}{2}\right)}{\Gamma\left(\frac{k+k_2}{2}+1\right)} - \\
&\frac{\theta_m^{-(k+n/2)}\,(xN\lambda\,/2)^{k+k_1}}{k!\,\Gamma(n+k+1)\,(k+k_1)} \frac{\Gamma\left(\frac{k+k_1+1}{2})\right)}{\Gamma\left(\frac{k+k_1}{2}+1\right)}\Bigg]
\end{aligned} \tag{62}
$$

where $\Psi(x,\theta_i) = xN\cos\theta_i\ \lambda/2$, in step (a), we used the fact that $z, \Psi(x,\theta_i) \geq 0, \forall\ z, x, \theta_i$, step (b) follows from the fact that $1 - F_I(z) = \mathbb{P}(Z\ > z)$, and in the step (c) we used $\int_0^{\pi/2} \cos^z(x)\, dx = \frac{\sqrt{\pi}}{2}\frac{\Gamma(\frac{z+1}{2})}{\Gamma(\frac{z}{2}+1)}$, $\forall\ \Re\{z\} > -1$.

$$
\begin{aligned}
\mathbb{P}(PL_I(z) < PL_D \,|z) &= \mathbb{P}\left(\frac{1}{C}\left(\frac{2z}{N\lambda\,\cos\theta_i}\right)^2 < \frac{D^2}{C}\,\Big|z\right) \\
&= \mathbb{P}\left(D^2 > \left(\frac{2z}{N\lambda\,\cos\theta_i}\right)^2\,\Big|z\right) \\
&= \mathbb{P}(|D| > |\chi(z,\theta_i)|\big|z) \\
&\overset{\text{(a)}}{=} \mathbb{P}(D > \chi(z,\theta_i)\,\big|z) \\
&= \int_0^{\pi/2} \mathbb{P}\big(D > \chi(z,\theta_i)\,\big|z,\theta_i\big)\,\frac{2}{\pi}\,d\theta_i \\
&= \int_0^{\pi/2} \Big(1 - \tilde{F}_{d_{UB}}\big(\chi(z,\theta_i)\big)\Big)\,\frac{2}{\pi}\,d\theta_i \\
&= 1 - \int_0^{\pi/2} \frac{1}{\Gamma(k_D)}\,\gamma\left(k_D, \frac{\chi(z,\theta_i)}{\theta_D}\right)\,\frac{2}{\pi}\,d\theta_i \\
&\overset{\text{(b)}}{=} 1 - \frac{2}{\pi\,\Gamma(k_D)} \int_0^{\pi/2} \sum_{k=0}^{\infty} \frac{(-1)^k\,\left(\frac{\chi(z,\theta_i)}{\theta_D}\right)^{k_D+k}}{k!\,(k_D+k)}\,d\theta_i \\
&= 1 - \frac{2}{\pi\,\Gamma(k_D)} \sum_{k=0}^{\infty} \frac{(-1)^k}{k!\,(k_D+k)} \int_0^{\pi/2} \left(\frac{2z}{N\lambda\,(\cos\theta_i)\theta_D}\right)^{k_D+k}\,d\theta_i \\
&= 1 - \\
&\frac{2}{\pi\,\Gamma(k_D)} \sum_{k=0}^{\infty} \frac{(-1)^k}{k!\,(k_D+k)} \left(\frac{2z}{N\lambda\,\theta_D}\right)^{k_D+k} \int_0^{\pi/2} (\cos\theta_i)^{-(k_D+k)}\,d\theta_i \\
&= 1 - \frac{2}{\pi\,\Gamma(k_D)} \sum_{k=0}^{\infty} \frac{(-1)^k}{k!\,(k_D+k)} \omega^{k_D+k}\,z^{k_D+k}\,\Upsilon(k,k_D) \qquad (63)
\end{aligned}
$$

where $\chi(z,\theta_i) = 2z/(N\lambda\cos\theta_i)$, $\omega = \frac{2}{N\lambda\,\theta_D}$, $\Upsilon(k,k_D) = \int_0^{\pi/2}(\cos\theta_i)^{-(k_D+k)}\,d\theta_i$, the step (a) follows from the fact that $D \geq 0$, $\chi(z,\theta_i) \geq 0$, and in the step (b) we used the series expansion of lower incomplete gamma function given by ([52], 8.354),

$$
\gamma(\alpha,x) = \sum_{n=0}^{\infty} \frac{(-1)^n\,x^{\alpha+n}}{n!\,(\alpha+n)} \qquad (64)
$$

Now, let's find (46), and (47), using total probability theorem.

$$
\mathbb{P}(A_{D,PL}) = \mathbb{P}(PL_D \leq PL_I)
$$

$$
\begin{aligned}
&= \int_0^\infty \mathbb{P}(PL_D(x) \leq PL_I \,|x)\; \tilde{f}_{d_{UB}}(x)\; dx \\
&= \int_0^\infty \left(1 - \frac{\Lambda_1}{\sqrt{\pi}} \sum_{k=0}^{\infty} \left[\frac{\theta_m^{-k+n/2}}{k!} \frac{(xN\lambda\,/2)^{k+k_2}}{(k+k_2)\,\Gamma(-n+k+1)} \frac{\Gamma(\frac{k+k_2+1}{2})}{\Gamma(\frac{k+k_2}{2}+1)} - \right.\right. \\
&\quad \left.\left. \frac{\theta_m^{-(k+n/2)}}{k!} \frac{(xN\lambda\,/2)^{k+k_1}}{(k+k_1)\,\Gamma(n+k+1)} \frac{\Gamma(\frac{k+k_1+1}{2})}{\Gamma(\frac{k+k_1}{2}+1)} \right] \right) \frac{x^{k_D-1}\, e^{-x/\theta_D}}{\theta_D^{k_D}\,\Gamma(k_D)}\; dx \\
&= \int_0^\infty \frac{x^{k_D-1}\, e^{-x/\theta_D}}{\theta_D^{k_D}\,\Gamma(k_D)}\; dx - \\
&\frac{\Lambda_1/\sqrt{\pi}}{\theta_D^{k_D}\,\Gamma(k_D)} \sum_{k=0}^{\infty} \left[\frac{\theta_m^{-k+n/2}}{k!} \frac{(N\lambda\,/2)^{k+k_2}}{(k+k_2)\,\Gamma(-n+k+1)} \frac{\Gamma(\frac{k+k_2+1}{2})}{\Gamma(\frac{k+k_2}{2}+1)} \right. \\
&\qquad \int_0^\infty x^{k+k_2}\, x^{k_D-1}\, e^{-x/\theta_D}\; dx - \\
&\quad \frac{\theta_m^{-(k+n/2)}}{k!} \frac{(N\lambda\,/2)^{k+k_1}}{(k+k_1)\,\Gamma(n+k+1)} \frac{\Gamma(\frac{k+k_1+1}{2})}{\Gamma(\frac{k+k_1}{2}+1)} \\
&\quad \left. \int_0^\infty x^{k+k_1}\, x^{k_D-1}\, e^{-x/\theta_D}\; dx \right] \\
&\overset{(a)}{=} 1 - \frac{\Lambda_1/\sqrt{\pi}}{\theta_D^{k_D}\,\Gamma(k_D)} \sum_{k=0}^{\infty} \left[\frac{\theta_m^{-k+n/2}}{k!} \frac{(N\lambda\,/2)^{k+k_2}}{(k+k_2)\,\Gamma(-n+k+1)} \frac{\Gamma(\frac{k+k_2+1}{2})}{\Gamma(\frac{k+k_2}{2}+1)} \right. \\
&\quad \int_0^\infty (\theta_D\tau)^{k+k_2+k_D-1}\, e^{-\tau}\, \theta_D\; d\tau - \\
&\quad \frac{\theta_m^{-(k+n/2)}}{k!} \frac{(N\lambda\,/2)^{k+k_1}}{(k+k_1)\,\Gamma(n+k+1)} \frac{\Gamma(\frac{k+k_1+1}{2})}{\Gamma(\frac{k+k_1}{2}+1)} \\
&\quad \left. \int_0^\infty (\theta_D\tau)^{k+k_1+k_D-1}\, e^{-\tau}\, \theta_D\; d\tau \right] \\
&= 1 - \frac{\Lambda_1/\sqrt{\pi}}{\theta_D^{k_D}\,\Gamma(k_D)} \sum_{k=0}^{\infty} \left[\frac{\theta_m^{-k+n/2}}{k!} \frac{(N\lambda\,/2)^{k+k_2}}{(k+k_2)\,\Gamma(-n+k+1)} \frac{\Gamma(\frac{k+k_2+1}{2})}{\Gamma(\frac{k+k_2}{2}+1)} \theta_D^{k+k_2+k_D} \right. \\
&\quad \int_0^\infty \tau^{(k+k_2+k_D)-1}\, e^{-\tau}\; d\tau - \\
&\quad \frac{\theta_m^{-(k+n/2)}}{k!} \frac{(N\lambda\,/2)^{k+k_1}}{(k+k_1)\,\Gamma(n+k+1)} \frac{\Gamma(\frac{k+k_1+1}{2})}{\Gamma(\frac{k+k_1}{2}+1)} \theta_D^{k+k_1+k_D} \\
&\quad \left. \int_0^\infty \tau^{(k+k_1+k_D)-1}\, e^{-\tau}\; d\tau \right] \\
&= 1 - \frac{\Lambda_1/\sqrt{\pi}}{\theta_D^{k_D}\,\Gamma(k_D)} \sum_{k=0}^{\infty} \left[\frac{\theta_m^{-k+n/2}}{k!} \frac{(N\lambda\,/2)^{k+k_2}}{(k+k_2)\,\Gamma(-n+k+1)} \frac{\Gamma(\frac{k+k_2+1}{2})}{\Gamma(\frac{k+k_2}{2}+1)} \right. \\
&\quad \left. \theta_D^{k+k_2+k_D}\,\Gamma(k+k_2+k_D) - \right.
\end{aligned}
$$

$$\left.\frac{\theta_m^{-(k+n/2)}}{k!}\frac{(N\lambda\,/2)^{k+k_1}}{(k+k_1)\,\Gamma(n+k+1)}\,\frac{\Gamma(\frac{k+k_1+1}{2})}{\Gamma(\frac{k+k_1}{2}+1)}\theta_D^{k+k_1+k_D}\,\Gamma(k+k_1+k_D)\right] \tag{65}$$

where in the step (a), we employed change of variable $x/\theta_D = \tau$ and

$$\mathbb{P}(A_{I,PL}) = 1 - \mathbb{P}(A_{D,PL}) \tag{66}$$

Note that the expression in (65) gives a constant number.

4.2.6. Conditional SNR Coverage Probabilities

In this section we will investigate the SNR coverage probabilities in (11).

$$\begin{aligned}\mathbb{P}(SNR_D(x) > T\,|x) &= \mathbb{P}(\frac{|h_D|^2}{PL_D(x)\,\sigma_n^2} > T\,|x)\\ &= \mathbb{P}(|h_D|^2 > \sigma_n^2\,PL_D(x)T\,|x)\\ &= \mathbb{P}(|h_D| > \sqrt{\sigma_n^2\,PL_D(x)T}\,|x)\\ &= Q_1\left(\frac{\nu_k}{\sigma_k}, \frac{\mathcal{T}_{\mathcal{D}}(T,x)}{\sigma_k}\right)\end{aligned} \tag{67}$$

where $\mathcal{T}_{\mathcal{D}}(T,x) = \sqrt{\sigma_n^2\,PL_D(x)T}$, and $Q_1(a,b)$ is the Marcum Q-function with $\nu_k = \sqrt{\frac{K\Omega}{1+K}}$ and $\sigma_k = \sqrt{\frac{\Omega}{2(1+K)}}$

The SNR coverage probability for the indirect link can be derived as follows,

$$\begin{aligned}\mathbb{P}(SNR_I(z,\theta_i) > T\,|z,\theta_i) &= \mathbb{P}\left(\frac{\left(\frac{1}{N}\sum_{n=1}^{N}|h_{1,n}|\,|h_{2,n}|\right)^2}{PL_I(z,\theta_i)\,\sigma_n^2} > T\,\middle|\,z,\theta_i\right)\\ &= \mathbb{P}\left(\left(\sum_{n=1}^{N}|h_{1,n}|\,|h_{2,n}|\right) > \sqrt{N^2\sigma_n^2\,TPL_I(z,\theta_i)}\,\middle|\,z,\theta_i\right)\end{aligned} \tag{68}$$

Let's define $u = \sum_{n=1}^{N} |h_{1,n}| \; |h_{2,n}|$. To get the closed-form expression for (68), we need to find the distribution of u. If the N is large enough, we can use the central limit theorem (CLT). Hence, the random variable u can be modeled with the Gaussian distribution $\mathcal{U} \sim \mathcal{N}(m_u, \sigma_u^2)$. Let,

$$|h_{1,n}|, |h_{2,n}| \sim f_H(x) = \frac{2(K+1)\,x}{\Omega} \exp\left(-K - \frac{(K+1)\,x^2}{\Omega}\right) \; I_0\left(2x\sqrt{\frac{K(K+1)}{\Omega}}\right)$$

and

$$Y = |h_{1,n}||h_{2,n}| \sim f_Y(y) = \int_0^\infty \frac{1}{x} f_H(x) \; f_H(y/x) \; dx$$

Hence,

$$\begin{aligned}
f_Y(y) = \int_0^\infty & \frac{1}{x} \frac{2(K+1)\,x}{\Omega} \exp\left(-K - \frac{(K+1)\,x^2}{\Omega}\right) \; I_0\left(2x\sqrt{\frac{K(K+1)}{\Omega}}\right) \\
& \frac{2(K+1)\,y/x}{\Omega} \exp\left(-K - \frac{(K+1)\,(y/x)^2}{\Omega}\right) \; I_0\left(2(y/x)\sqrt{\frac{K(K+1)}{\Omega}}\right) \; dx \\
= & \frac{4(K+1)^2}{\Omega^2} y \int_0^\infty \frac{1}{x} \exp\left(-2K - \frac{(K+1)}{\Omega}\left(x^2 + \frac{y^2}{x^2}\right)\right) \\
& I_0\left(2x\sqrt{\frac{K(K+1)}{\Omega}}\right) \; I_0\left(2(y/x)\sqrt{\frac{K(K+1)}{\Omega}}\right) \; dx \\
= & \; 4\Lambda_2^2 \; \exp(-2K) \; y \int_0^\infty \frac{1}{x} \; \exp\left(-\Lambda_2\left(x^2 + \frac{y^2}{x^2}\right)\right) \\
& I_0\left(2x\sqrt{K\Lambda_2}\right) \; I_0\left(2(y/x)\sqrt{K\Lambda_2}\right) \; dx \\
\overset{(a)}{=} & \; 4\Lambda_2^2 \; \exp(-2K) \; y \int_0^\infty \frac{1}{x} \; \exp\left(-\Lambda_2\left(x^2 + \frac{y^2}{x^2}\right)\right) \\
& \sum_{k=0}^{\infty} \frac{(4x^2 K\Lambda_2/4)^k}{k!\,\Gamma(k+1)} \sum_{m=0}^{\infty} \frac{(4y^2 K\Lambda_2/(4x^2))^m}{m!\,\Gamma(m+1)} \; dx \\
= & \; 4\Lambda_2^2 \; \exp(-2K) \; y \sum_{k=0}^{\infty} \sum_{m=0}^{\infty} \frac{(K\Lambda_2)^{k+m}}{k!\;m!\;\Gamma(k+1)\;\Gamma(m+1)} \; y^{2m} \\
& \int_0^\infty x^{2k-2m-1} \; \exp\left(-\Lambda_2\left(x^2 + \frac{y^2}{x^2}\right)\right) \; dx \\
\overset{(b)}{=} & \; 4\Lambda_2^2 \; \exp(-2K) \; \sum_{k=0}^{\infty} \sum_{m=0}^{\infty} \left(\frac{(K\Lambda_2)^{k+m}}{k!\;m!\;\Gamma(k+1)\;\Gamma(m+1)}\right.
\end{aligned}$$

$$y^{2m+1}\ (y^2)^{\frac{k-m}{2}}\ K_{k-m}(2\sqrt{\Lambda_2^2\ y^2})\Big)$$
$$= 4\Lambda_2^2\ \exp(-2K)\ \sum_{k=0}^{\infty}\sum_{m=0}^{\infty}\frac{(K\Lambda_2)^{k+m}}{k!\ m!\ \Gamma(k+1)\ \Gamma(m+1)}\ y^{m+k+1}\ K_{k-m}(2\Lambda_2\ y)$$

where $\Lambda_2 = \frac{K+1}{\Omega}$, in the step (a) we used the series expansion of the 0^{th} order modified Bessel function of 1^{st} kind given by,

$$I_0(z) = \sum_{k=0}^{\infty}\frac{(z^2/4)^k}{k!\ \Gamma(k+1)}$$

and in the step (b) we used the fact that ([52], p.370),

$$\int_0^{\infty} x^{\nu-1}\ \exp(-\beta x^p - \gamma x^{-p})\ dx = \frac{2}{p}\left(\frac{\gamma}{\beta}\right)^{\frac{\nu}{2p}}\ K_{\nu/p}(2\sqrt{\beta\ \gamma}), \qquad [\Re\{\beta\} > 0, \Re\{\gamma\} > 0]$$

Now, we can find the mean value and the variance of u using the above distribution.

$$\begin{aligned}
m_u &= N\ \mathbb{E}[Y] \\
&= N\ \int_0^{\infty} y\ 4\Lambda_2^2\ \exp(-2K)\ \sum_{k=0}^{\infty}\sum_{m=0}^{\infty}\Bigg(\frac{(K\Lambda_2)^{k+m}}{k!\ m!\ \Gamma(k+1)\ \Gamma(m+1)} \\
&\qquad y^{m+k+1}\ K_{k-m}(2\Lambda_2\ y)\ dy\Bigg) \\
&= N\ 4\Lambda_2^2\ \exp(-2K)\ \sum_{k=0}^{\infty}\sum_{m=0}^{\infty}\frac{(K\Lambda_2)^{k+m}}{k!\ m!\ \Gamma(k+1)\ \Gamma(m+1)}\int_0^{\infty} y^{k+m+2}K_{k-m}(2y\ \Lambda_2)\ dy \\
&\overset{\text{(a)}}{=} N\ 4\Lambda_2^2\ \exp(-2K)\ \sum_{k=0}^{\infty}\sum_{m=0}^{\infty}\frac{(K\Lambda_2)^{k+m}}{k!\ m!\ \Gamma(k+1)\ \Gamma(m+1)} \\
&\qquad \left(2^{k+m+1}\ (2\Lambda_2)^{-k-m-3}\ \Gamma\left(\frac{2k+3}{2}\right)\ \Gamma\left(\frac{2m+3}{2}\right)\right) \\
&= N\ \Lambda_2^2\ \exp(-2K)\ \sum_{k=0}^{\infty}\sum_{m=0}^{\infty}\frac{K^{k+m}\ \Lambda_2^{-3}}{k!\ m!\ \Gamma(k+1)\ \Gamma(m+1)} \\
&\qquad \left(\Gamma\left(\frac{2k+3}{2}\right)\ \Gamma\left(\frac{2m+3}{2}\right)\right) \\
&= N\ \Lambda_2^{-1}\ \exp(-2K)\ \sum_{k=0}^{\infty}\sum_{m=0}^{\infty}\frac{K^{k+m}}{k!\ m!}\ \frac{\Gamma(k+3/2)\ \Gamma(m+3/2)}{\Gamma(k+1)\ \Gamma(m+1)}
\end{aligned} \tag{69}$$

where in the step (a) we used the solution of the integral given below ([52], p.676),

$$\int_0^\infty x^\mu \, K_\nu(ax) \, dx = 2^{\mu-1} \, a^{-\mu-1} \, \Gamma\left(\frac{1+\mu+\nu}{2}\right) \Gamma\left(\frac{1+\mu-\nu}{2}\right),$$
$$[\Re\{\mu+1\pm\nu\} > 0, \, \Re\{a\} > 0]$$

$$\begin{aligned}
\mathbb{E}[Y^2] &= \int_0^\infty y^2 \, 4\Lambda_2^2 \, \exp(-2K) \\
&\quad \left(\sum_{k=0}^\infty \sum_{m=0}^\infty \frac{(K\Lambda_2)^{k+m}}{k! \, m! \, \Gamma(k+1) \, \Gamma(m+1)} \, y^{m+k+1} \, K_{k-m}(2\Lambda_2 \, y) \, dy \right) \\
&= 4\Lambda_2^2 \, \exp(-2K) \, \sum_{k=0}^\infty \sum_{m=0}^\infty \frac{(K\Lambda_2)^{k+m}}{k! \, m! \, \Gamma(k+1) \, \Gamma(m+1)} \\
&\quad \int_0^\infty y^{k+m+3} K_{k-m}(2y \, \Lambda_2) \, dy \\
&= 4\Lambda_2^2 \, \exp(-2K) \, \sum_{k=0}^\infty \sum_{m=0}^\infty \frac{(K\Lambda_2)^{k+m}}{k! \, m! \, \Gamma(k+1) \, \Gamma(m+1)} \\
&\quad (2^{k+m+2} \, (2\Lambda_2)^{-k-m-4} \, \Gamma(k+2) \, \Gamma(m+2)) \\
&= \Lambda_2^2 \, \exp(-2K) \, \sum_{k=0}^\infty \sum_{m=0}^\infty \frac{K^{k+m} \, \Lambda_2^{-4}}{k! \, m! \, \Gamma(k+1) \, \Gamma(m+1)} (\Gamma(k+2) \, \Gamma(m+2)) \\
&= \Lambda_2^{-2} \, \exp(-2K) \, \sum_{k=0}^\infty \sum_{m=0}^\infty \frac{K^{k+m}}{k! \, m!} \, \frac{\Gamma(k+2) \, \Gamma(m+2)}{\Gamma(k+1) \, \Gamma(m+1)} \\
&= \Lambda_2^{-2} \, \exp(-2K) \, \sum_{k=0}^\infty \sum_{m=0}^\infty \frac{K^{k+m}}{k! \, m!} \, (k+1) \, (m+1) \qquad (70)
\end{aligned}$$

Hence, we can find σ_u^2 by using (69) and (70),

$$\begin{aligned}
\sigma_y^2 &= \mathbb{E}[Y^2] - (m_u/N)^2 \\
\sigma_u^2 &= N \, \sigma_y^2 \qquad (71)
\end{aligned}$$

Since we have the distribution of u, we can find the closed-form solution of (68) with the Gaussian CDF,

$$\begin{aligned}\mathbb{P}(SNR_I(z,\theta_i) > T \,|z,\theta_i) &= \mathbb{P}\left(U > \sqrt{N^2\sigma_n^2\, TPL_I(z,\theta_i)}\right) \\ &= Q\left(\frac{\mathcal{T}_{\mathcal{I}}(T,z,\theta_i) - m_u}{\sigma_u}\right) \end{aligned} \tag{72}$$

where $\mathcal{T}_{\mathcal{I}}(T,z,\theta_i) = \sqrt{N^2\sigma_n^2\, TPL_I(z,\theta_i)}$, and $Q(x) = \frac{1}{\sqrt{2\pi}}\int_x^\infty \exp\left(-\frac{u^2}{2}\right)\, du$, is the Q-function. Note that we need the SNR probability depends on just the variable z. Hence we should apply the total probability theorem to (72) given by

$$\mathbb{P}(SNR_I(z) > T|z) = \int_0^{\pi/2} Q\left(\frac{\mathcal{T}_{\mathcal{I}}(T,z,\theta_i) - m_u}{\sigma_u}\right)\frac{2}{\pi}\, d\theta_i \tag{73}$$

To conclude, the SNR coverage probability can be obtained by substituting (28), (44), (52)-(55), (58), (59), (67), and (73) into (11).

5. NUMERICAL RESULTS

In this section, we will provide some key simulation results to understand the impact of IRSs on the mmWave networks from the coverage perspective. There are 4 main parameters in our simulations, which are λ_{BS}, μ, ρ, and L_I. The definitions of the first two parameters are given in the Section 4.1. The parameter ρ determines what percentage of the map area is covered by the buildings, e.g. $\rho = \lambda_b E[L]E[W]$, and L_I is the length of the one side of the IRS in meters, $L_I = 0.7071\ \lambda\sqrt{N}$. The values of the system parameters we used in our simulations are given in Table 5.1. We take the value of ρ as 0.26 in some of our simulations because it is the value surveyed in the paper [14]. They measure the area covered by buildings on a region of the UT Austin campus and they found the value of 0.26. Moreover, we compare our method with the case that the network lack of IRSs, we call this event as 'No IRS', and formally it can be given by,

$$P_C(T|\{\text{No IRS}\}) = \mathbb{P}(\overline{A_D'})\int_0^\infty \mathbb{P}(SNR_D(x) > T|x)\ \tilde{f}_{d_{UB}}(x)\, dx \tag{74}$$

Variable	Description	Value
G_t	Transmit Antenna Gain	20 dBi
G_r	Receiver Antenna Gain	10 dBi
σ_n^2	Noise Power	-203 dB/Hz
BW	Bandwidth	100 MHz
c	The speed of light	3×10^8
f_c	Operating frequency	60 GHz
$\mathbb{E}[W]$	Expected width of buildings	52
$\mathbb{E}[L]$	Expected length of buildings	55
K	Rician K-factor	1
$\mathbb{E}\{\lvert h_D \rvert\}$	Mean value for small scale fading	1
L_m	Map length	7 km

Table 5.1 Simulation parameters

According to Rényi's Theorem, simple point processes are completely characterized by their void probabilities. Simple PPs are the PPs have a finite intensity function for any Borel set. Hence, we should investigate the null probabilities of the simulation and the proposed model. In Fig. 5.1, we show the null probabilities of the UE-BS link, Indirect link, and their joint probability for consecutive repetitions. For instance, the null probability of the UE-BS link for repetition one shows the ratio that the TUE cannot reach any direct BS for 4000 iterations. To be specific, for the rate of around 0.32, TUE cannot see any direct BS for the given system parameters in 5.1. On the other hand, for the indirect link ($\hat{A}_I$), TUE cannot reach any indirect BS for the rate of around 0.5. Note that the simulations coincide with the analytical expression given in the black line. However, for the joint probability (Fig 5.1 (c)), there is a small difference between them. No matter how small the difference is, it indicates that there is a dependence between direct and indirect links. In our derivations, we assume that these links are independent. Since the difference is quite small, the assumption of independence does not result in a large gap between the simulation and analytical results.

In Fig.5.2, we show the performance of the Monte-Carlo simulation (MCS) and a sample of the contribution of IRS to the network coverage. The difference in the MCS and the analytical plot resulted from the aforementioned dependence but as we can observe, MCS follows the general shape of our analytical result which is given with the solid plots. The upper blue curve indicates the total coverage probability (CP), and the below green one and red one

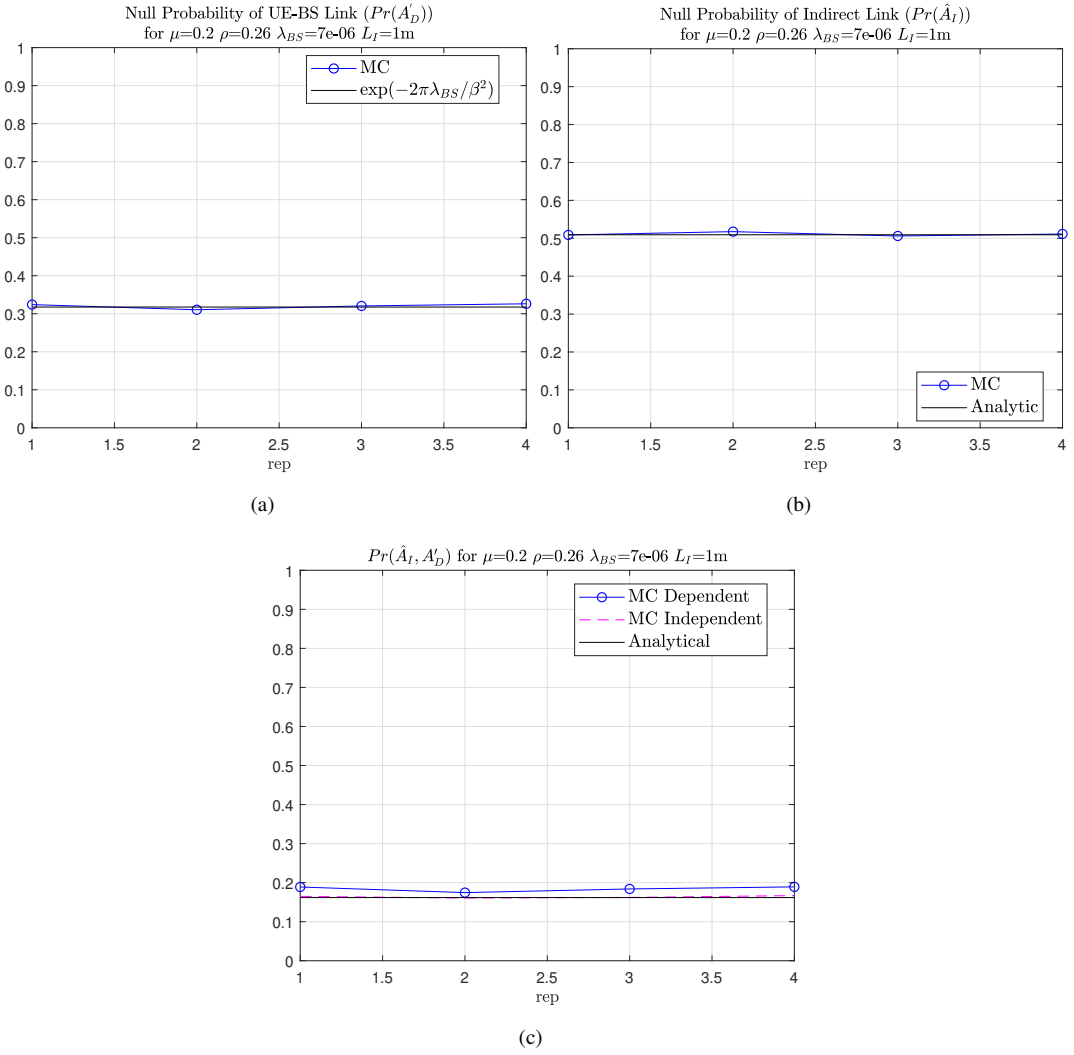

Figure 5.1 Null probabilities for (a) UE-BS link, (b) Indirect link, (c) Joint UE-BS and Indirect link.

show the CP of No IRS case and just direct links, respectively. Hence, the difference in the blue and green curves demonstrates the advantage of using IRS in the mmWave networks. The reason why the CP of just direct link is lower than the CP without IRS is that the 1x1m IRS can compete with the direct link. In other words, in some situations, even if the TUE sees a direct BS, it does not connect to direct BS because the PL value of the indirect link will be smaller. The four different components of coverage mentioned in (11) is illustrated in Fig. 5.3.

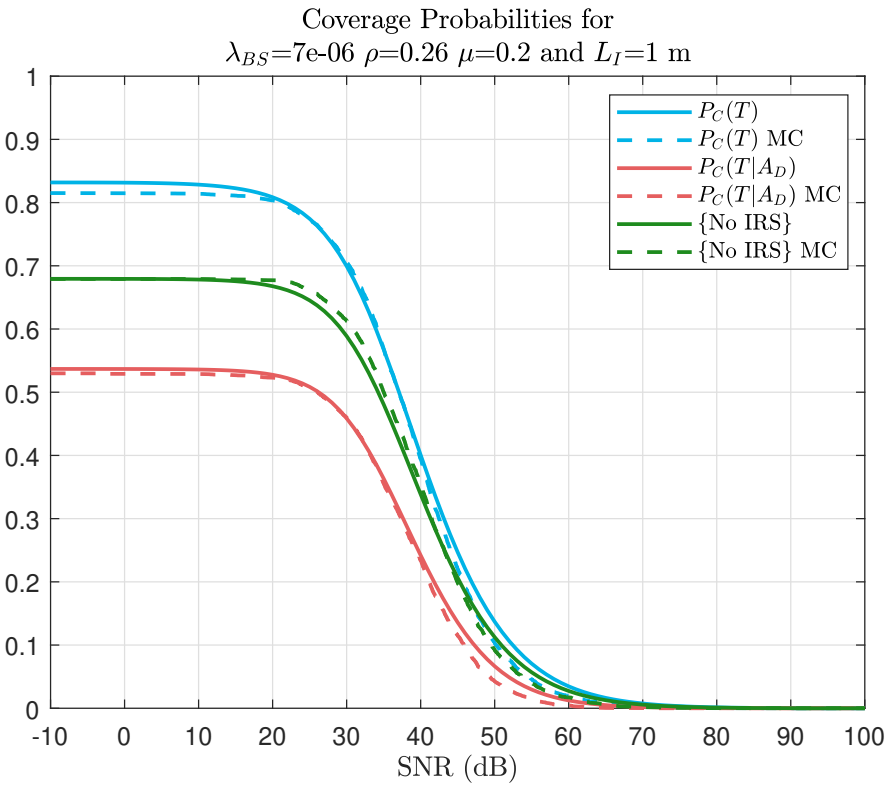

Figure 5.2 Performance of the simulation with λ_{BS} = 7/km^2, ρ = 0.26, μ = 0.2, and $L_I = 1\ m$.

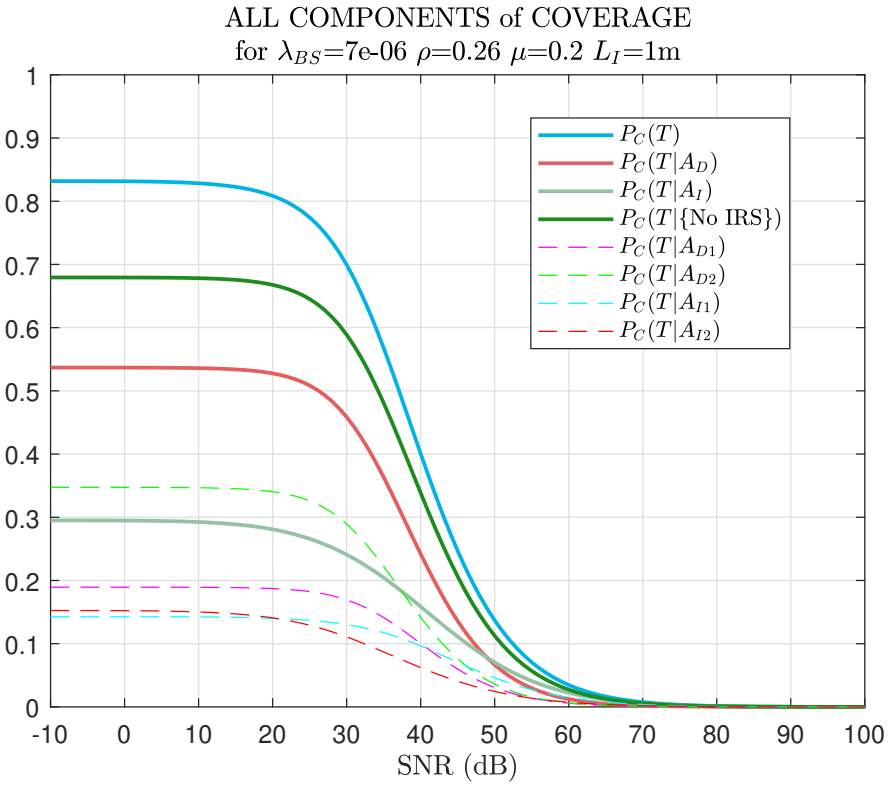

Figure 5.3 All components of the coverage for λ_{BS} = 7/km^2, ρ = 0.26 μ = 0.2, and $L_I = 1\ m$.

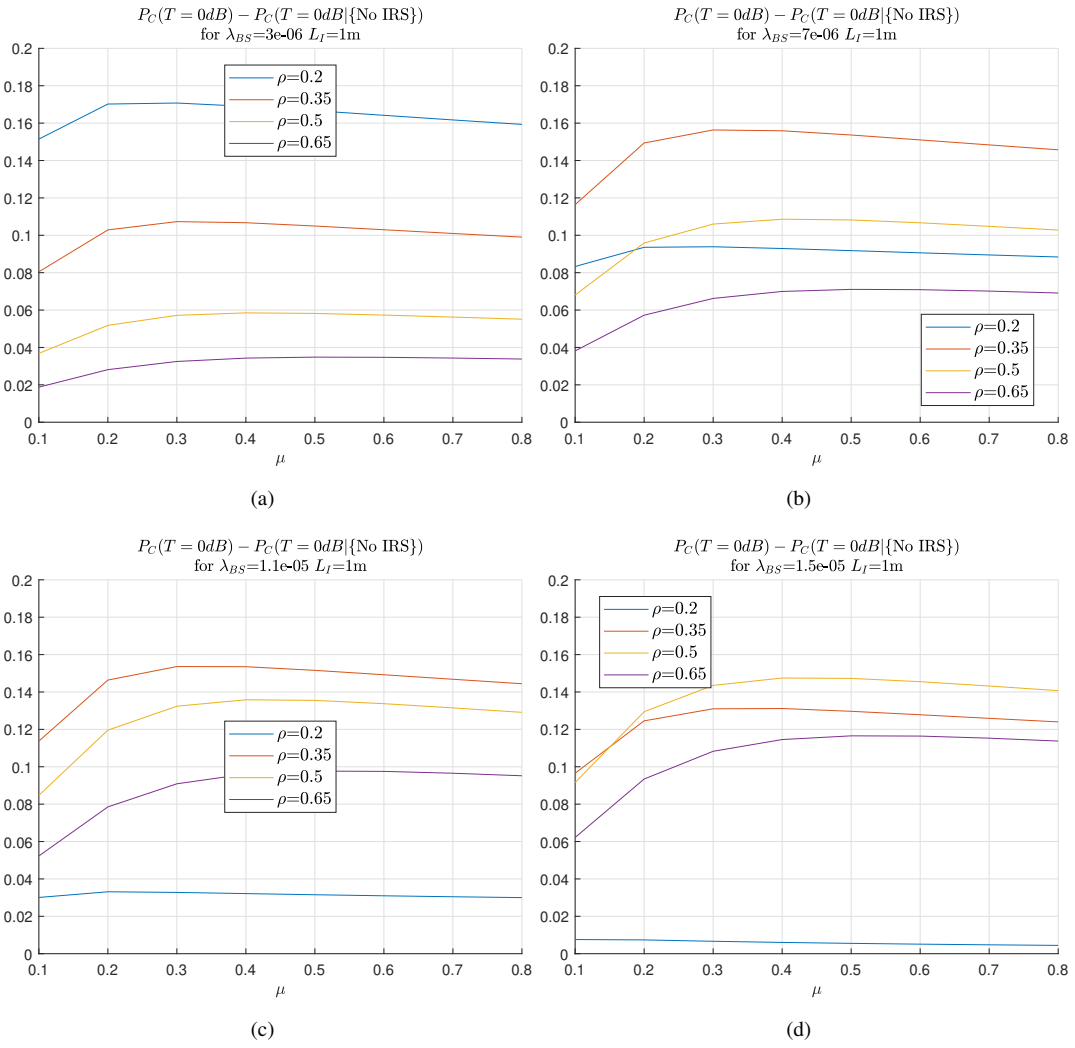

Figure 5.4 The difference between the values of coverage probabilities with and without IRS at $SNR = 0\ dB$ for $L_I = 1\ m$, varying ρ, μ, and (a) λ_{BS} = 3/km^2, (b) λ_{BS} = 7/km^2, (c) λ_{BS} = 11/km^2, (d) λ_{BS} = 15/km^2.

As we can observe from Fig. 5.3, the maximum coverage is obtained with the case that the TUE sees only a direct BS. If the TUE can reach both the direct BS and the indirect BS, it chooses the direct BS with a rate around 0.2, and it chooses the indirect BS at 0.15 rates. The latter value can also be seen in the difference between CPs of No IRS and just the direct link ($P_C(T|\{\text{No IRS}\})$, $P_C(T|A_D)$).

The impact of the IRS on network coverage varies with the BS density. To observe this, we plot four different figures with four different BS densities in Fig. 5.4, $\lambda_{BS} \in [3, 7, 11, 15] \times 10^{-6}$, indicating the difference between the total CP and the CP without IRS at $SNR = 0$dB for increasing IRS deployment ratio μ and various values of ρ. As can be seen, the value of

the maximum difference is almost the same for all BS densities but the building ratio that gives this maximum value increases with increasing BS density. On the other hand, the IRS deployment ratio makes no difference in the CP for values greater than 0.3. This is because the TUE can reach a limited number of LoS IRS, in other words, if we think that all the LoS buildings lie inside a circle with radius r, no matter how we increase the IRS deployment ratio the radius stays the same. Hence, there is an optimal value for the IRS deployment ratio, which is around 0.3 in our case. For instance, for the BS density 11/km^2, the maximum boost is obtained for the building ratio of 0.35 and μ=0.3 for the IRS length of 1m, see Fig. 5.5. As we can observe, the only impact of IRSs on the network coverage is not limited to the low-SNR regimes, it also shifts the coverage plot to the right because there is a quadratic gain depending on the number of elements of IRS in the indirect link. Note that approximately 8×10^8 elements can be packed just to 1×1m IRS at 60 GHz. The effect of IRS length on the coverage is illustrated in Fig. 5.6.

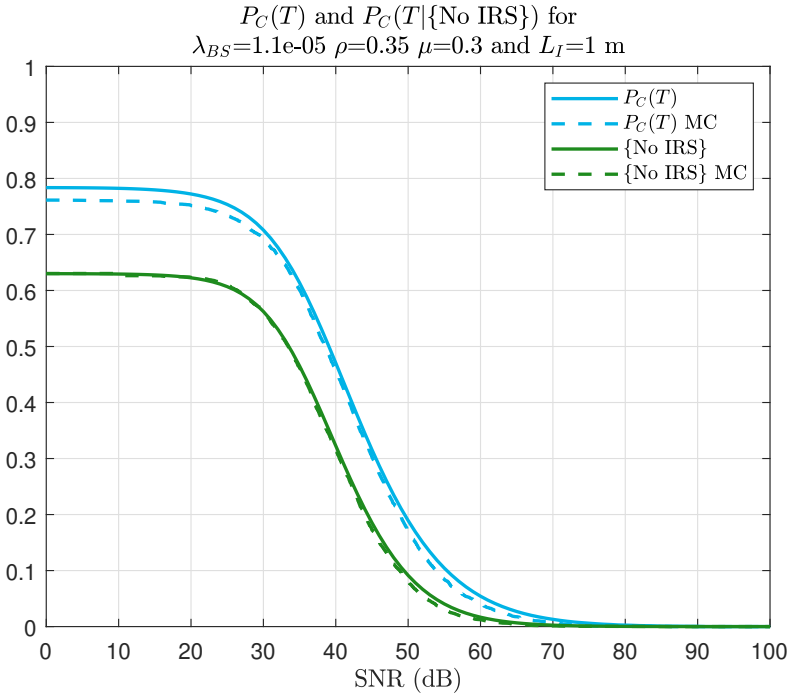

Figure 5.5 The coverage probability for the parameters gives the maximum difference in Fig. 5.4 (c).

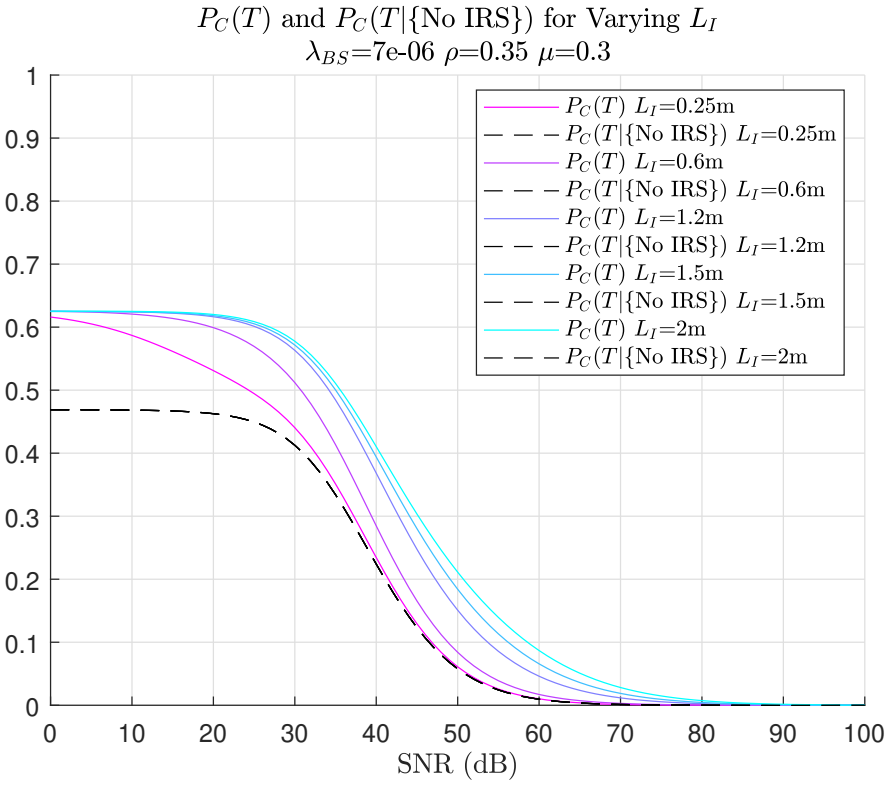

Figure 5.6 Coverage probabilities for various IRS lengths, λ_{BS} = 7/km^2, ρ = 0.35, and μ = 0.3.

We plot five different coverage plots for increasing IRS lengths L_I starting from 25 cm to 2 meters in Fig. 5.6. We also illustrated the coverage without IRS for all the IRS lengths. As can be predicted, CPs without IRS (given in dashed line) is the same for all IRS lengths but the difference increases for increasing L_I. In the low-SNR regime, the gain is almost the same for all IRS lengths but the difference is obvious in the high-SNR regime. However, for the values greater than 1.2m there is only a small gain in the very high-SNR regimes. Hence, it can be stated that the optimal value for the IRS length is around 1.2 m at 60GHz.

How much gain can be obtained with IRS relative to the gain without IRS is given in Fig. 5.7. As illustrated, the maximum ratio of the gain is higher than the maximum gain of difference (Fig. 5.4), since the total probability of densely built regions is much lower than the sparse ones. Nonetheless, the maximum ratio of coverage boost of IRSs varies between 45% and 40%. Additionally, the maximum values are obtained in densely built regions such as ρ=0.65. Note that it is a very high value for the building ratio. This is just the opposite with the gain of differences (Fig. 5.4). There, the highest values were obtained with lower blockage ratios.

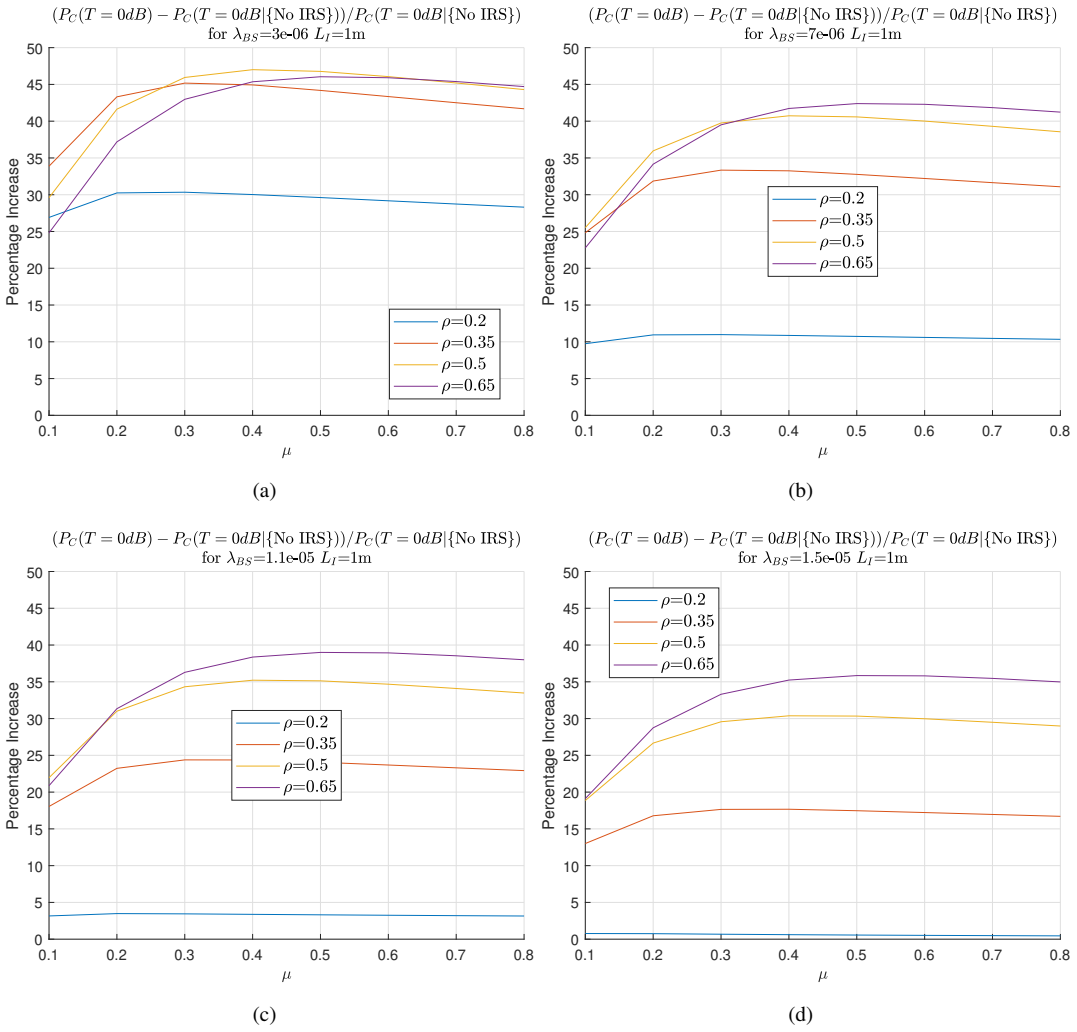

Figure 5.7 The ratio of the difference between coverage probabilities with and without IRS at $SNR = 0\ dB$ to the coverage probability without IRS at $SNR = 0\ dB$ for $L_I = 1\ m$, varying ρ, μ, and (a) λ_{BS} = 3/km^2, (b) λ_{BS} = 7/km^2, (c) λ_{BS} = 11/km^2, (d) λ_{BS} = 15/km^2.

Next, we will investigate the coverage performance of the network with the constant value for θ_i (the angle between the normal of an IRS and the incident wave). We take this value as uniformly distributed between 0 and π/2 in our derivations. In Fig. 5.8, we illustrated the CPs for different constant values of θ_i, and the one we use in our system model. As can be observed, as we get closer to π/2, the plot deviates markedly from our model, and for $\theta_i = 0.499\pi$ it is almost equal to the case without IRS. Since the $\theta_i = 0.499\pi$ means that the incident wave makes a $90°$ with the IRS normal vector. We can also observe that the optimal value is around 0.35π. Now, let's have a look at the coverage plots with $\theta_i \in [0, 0.15, 0.25, 0.35, 0.499]$ for various system parameters in Fig. 5.9. As can be seen, the CPs for $\theta_i = 0.35\pi$ is approximately the same as the one that has uniformly distributed θ_i.

Therefore, in the further studies regarding SNR analysis of IRS-aided networks, the value of the θ_i can be taken as 0.35π for the ease of derivations.

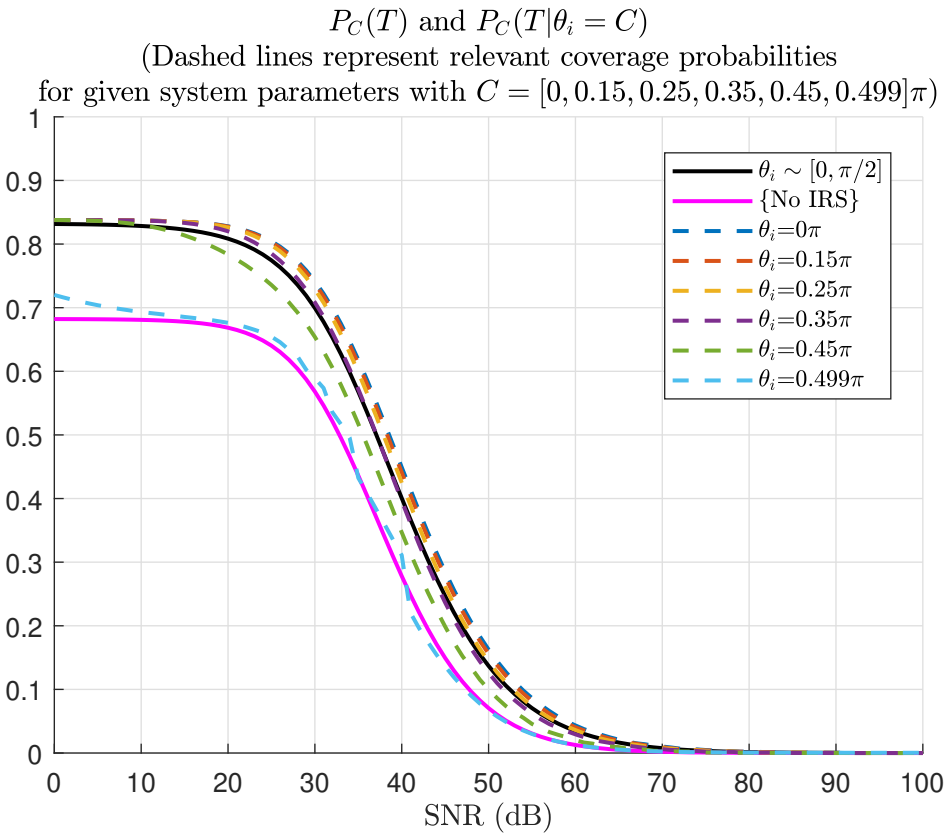

Figure 5.8 Coverage probabilities for various constant θ_i values, λ_{BS} = 7/km^2, ρ = 0.26, μ = 0.2, and $L_I = 1\ m$

We mentioned that in the literature, there are some works regarding the coverage analysis of IRS-aided SG-based networks in the Section 3. However, they consider the line Boolean model for buildings (takes buildings as lines) and the sum-distance PL model for the PL expression of the indirect link. Now, let's compare this method with our system model. First, we need to understand the parameter λ_b (blockage density) used in the Fig. 5.10. Since the line Boolean model considers buildings as lines, we cannot determine the parameter λ_b with the building ratio ρ. The blockage density would have to be so large to be equal to the ratio of the area of blockages. Hence, we take the value of λ_b with $\mathbb{E}[W] = 52$ ($\lambda_b = \rho/(55 \cdot 52) = 9.09 \times 10^{-}5$ for ρ = 0.26) for the analysis of the line Boolean model.

After deciding on the blockage density, we plot the line Boolean model for $\mathbb{E}[W] = 1$, random deployment of IRSs, and $PL_I \sim (d_{UI} + d_{IB})$ via our simulation, see Fig. 5.10. As can be observed, IRSs cannot contribute to the CP for the low-SNR regimes because the

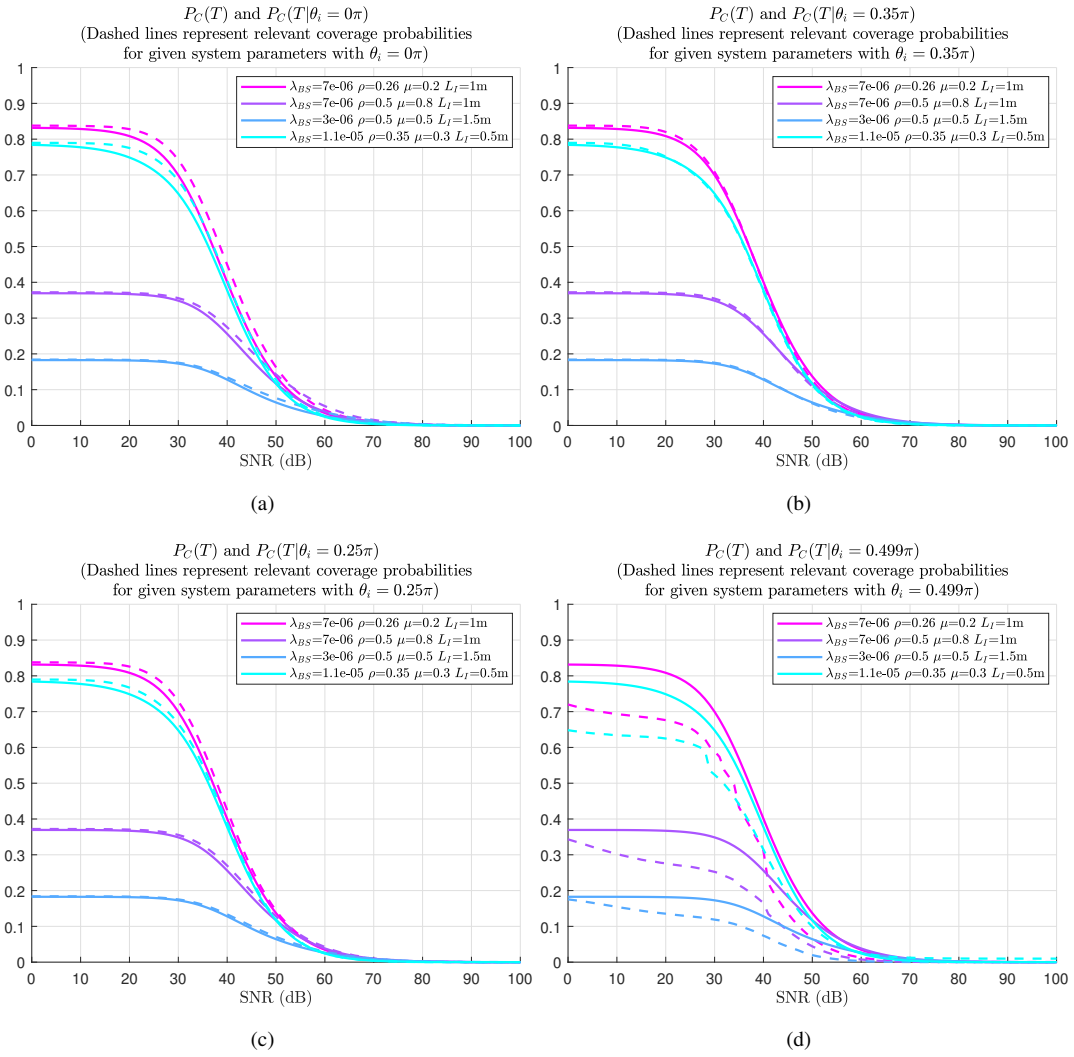

Figure 5.9 Sample coverage probabilities for different constant θ_i values showing the performance of coverage probabilities with fixed θ_i, best fit can be obtained with $\theta_i = 0.35\pi$.

buildings do not interfere very much with the direct links. In other words, the LoS range for the direct link of the line Boolean model is already too high. On the other hand, due to the sum-distance PL model, the PL of the indirect link becomes so small that the SNR values are much higher than expected in the high-SNR regime.

Finally, we illustrated the coverage performance of the proposed model with the random deployment of IRSs. To be more specific, if we place the IRSs randomly onto the buildings rather than placing them optimally, the variable ξ (the ratio of feasible BSs) is multiplied by 1/4. Hence, as can be expected, the contribution of the IRS to the network coverage would be smaller. In the Fig. 5.11 and 5.12, we illustrated the difference gain and the ratio gain of IRSs (the same approach used in the Fig. 5.4 and 5.7). In this case, the maximum difference

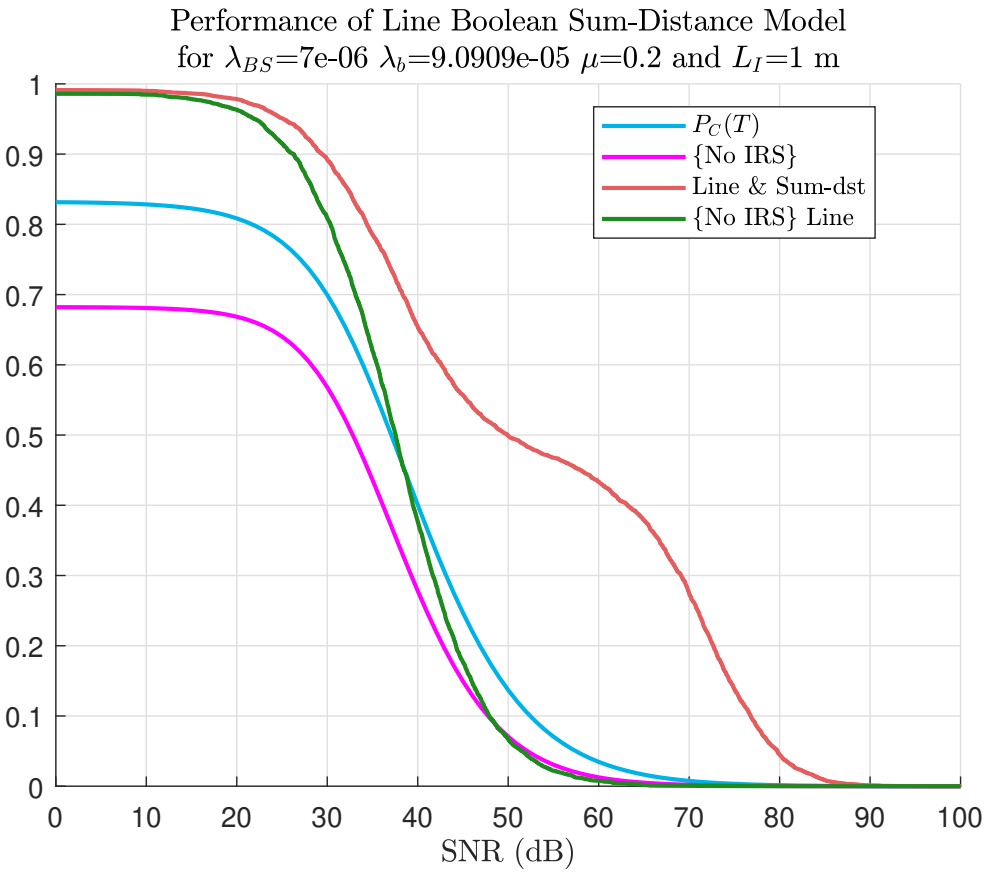

Figure 5.10 Comparing the model proposed in [15] and [16] (line Boolean scheme with sum-distance PL model for the indirect link) with the model proposed in this study (rectangular Boolean scheme with product-distance PL model).

that can be obtained with IRSs is about 0.05 which is quite low. However, the ratio is a bit higher which is around 10%.

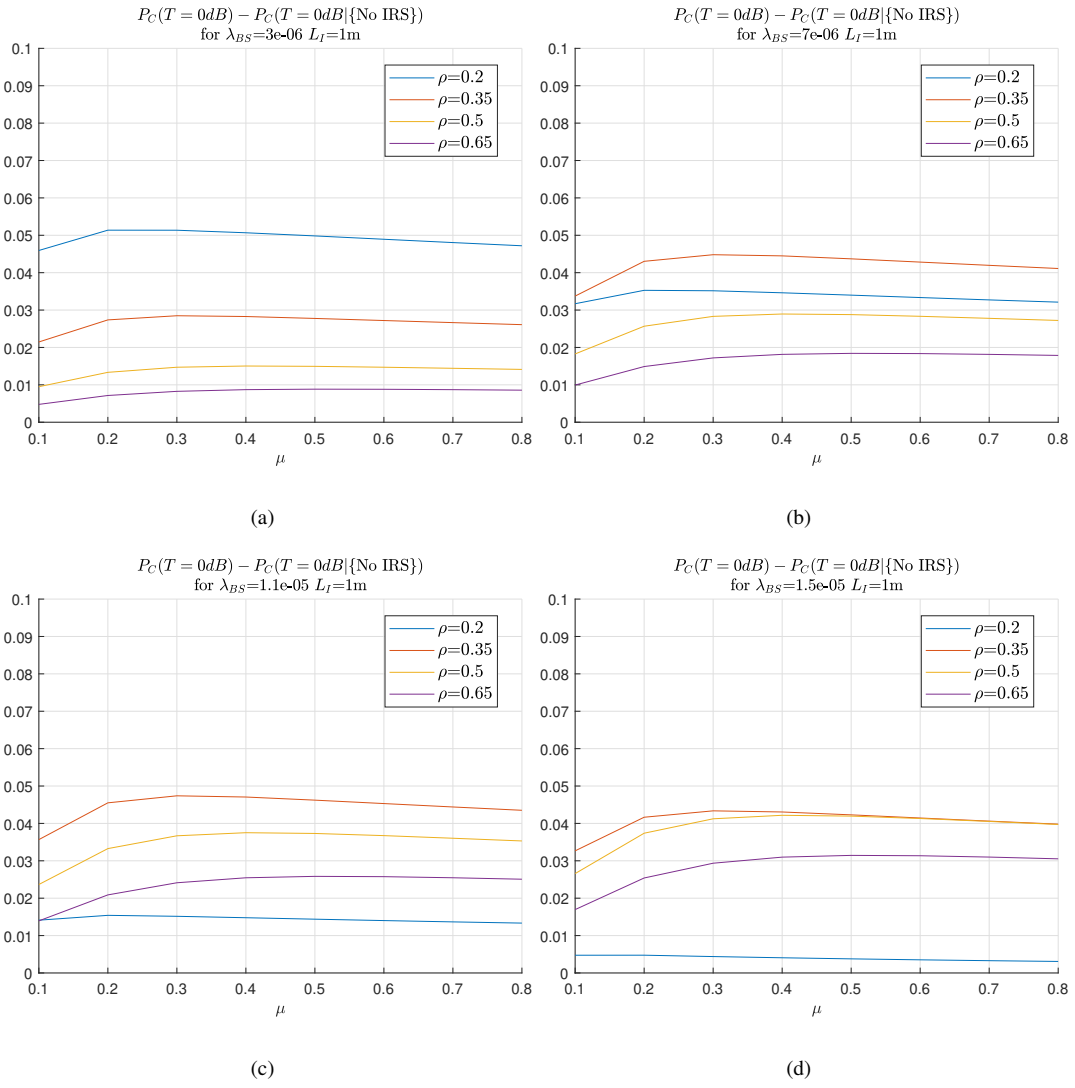

Figure 5.11 Performance analysis of the proposed model with the random deployment of IRSs into the one facade of buildings (difference between the total probability and the probability of No IRS case at $SNR = 0\ dB$).

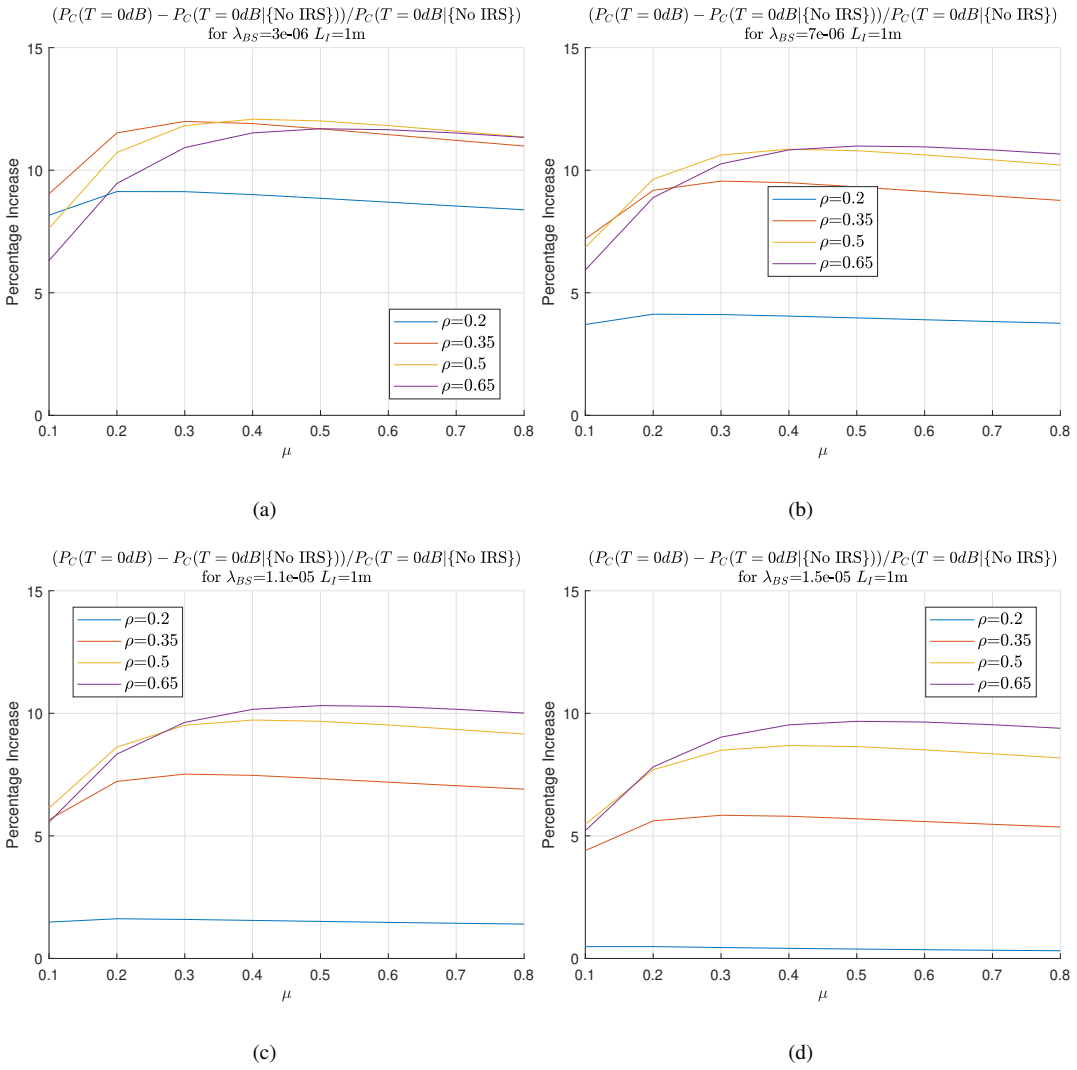

Figure 5.12 Performance analysis of the proposed model with the random deployment of IRSs into the one facade of buildings (ratio of the difference between the total probability and the probability of No IRS case to the CP without IRS at $SNR = 0\ dB$).

6. CONCLUSION

In this thesis, we propose a method to derive a closed-form expression for the coverage probability of IRS-aided SG-based networks with buildings that have a rectangular Boolean model and product-distance PL model for the indirect link. Since the distribution of the nearest-LoS neighbor distance is quite cumbersome for analytical tractability, we propose a gamma approximation for this distribution. Then we examine the coverage of IRS-aided networks for various aspects including varying IRS lengths, blockage and BS densities, and IRS deployment ratios. Then we compare our model with the one in the literature which is

the line Boolean sum-distance model. We show that our model is much more practical for the coverage analysis of IRS-aided networks.

In the literature, there is not much work done about the MIMO IRS-aided channels. As a future research direction, the MIMO channel model of IRS-aided indirect links can be examined. We assume a two-hop communication between the indirect BS and the TUE (means that a TUE can communicate through just one IRS), the optimal number of IRSs can be used in the indirect link communication can be investigated and the coverage probability for this multi-hop IRS-aided networks can be analyzed in the future works. We also assume the optimal IRS deployment in our derivations. In future works, the optimal placement of IRSs into to the facades of the buildings can also be investigated.

REFERENCES

[1] Hang Zhao, Rimma Mayzus, Shu Sun, Mathew Samimi, Jocelyn K Schulz, Yaniv Azar, Kevin Wang, George N Wong, Felix Gutierrez, and Theodore S Rappaport. 28 ghz millimeter wave cellular communication measurements for reflection and penetration loss in and around buildings in new york city. In *2013 IEEE international conference on communications (ICC)*, pages 5163–5167. IEEE, **2013**.

[2] Yunchou Xing and Theodore S Rappaport. Propagation measurements and path loss models for sub-thz in urban microcells. *arXiv preprint arXiv:2103.01151*, **2021**.

[3] Zhouyue Pi and Farooq Khan. An introduction to millimeter-wave mobile broadband systems. *IEEE communications magazine*, 49(6):101–107, **2011**.

[4] Wonbin Hong, Kwang-Hyun Baek, Youngju Lee, Yoongeon Kim, and Seung-Tae Ko. Study and prototyping of practically large-scale mmwave antenna systems for 5g cellular devices. *IEEE Communications Magazine*, 52(9):63–69, **2014**.

[5] Christos Liaskos, Shuai Nie, Ageliki Tsioliaridou, Andreas Pitsillides, Sotiris Ioannidis, and Ian Akyildiz. A new wireless communication paradigm

through software-controlled metasurfaces. *IEEE Communications Magazine*, 56(9):162–169, **2018**.

[6] Marco Di Renzo, Merouane Debbah, Dinh-Thuy Phan-Huy, Alessio Zappone, Mohamed-Slim Alouini, Chau Yuen, Vincenzo Sciancalepore, George C Alexandropoulos, Jakob Hoydis, Haris Gacanin, et al. Smart radio environments empowered by reconfigurable ai meta-surfaces: An idea whose time has come. *EURASIP Journal on Wireless Communications and Networking*, 2019(1):1–20, **2019**.

[7] Qingqing Wu and Rui Zhang. Towards smart and reconfigurable environment: Intelligent reflecting surface aided wireless network. *IEEE Communications Magazine*, 58(1):106–112, **2019**.

[8] Hirokazu Kamoda, Toru Iwasaki, Jun Tsumochi, Takao Kuki, and Osamu Hashimoto. 60-ghz electronically reconfigurable large reflectarray using single-bit phase shifters. *IEEE transactions on antennas and propagation*, 59(7):2524–2531, **2011**.

[9] Huanhuan Yang, Xiangyu Cao, Fan Yang, Jun Gao, Shenheng Xu, Maokun Li, Xibi Chen, Yi Zhao, Yuejun Zheng, and Sijia Li. A programmable metasurface with dynamic polarization, scattering and focusing control. *Scientific reports*, 6(1):1–11, **2016**.

[10] Xilong Pei, Haifan Yin, Li Tan, Lin Cao, Zhanpeng Li, Kai Wang, Kun Zhang, and Emil Björnson. Ris-aided wireless communications: Prototyping, adaptive beamforming, and indoor/outdoor field trials. *IEEE Transactions on Communications*, 69(12):8627–8640, **2021**.

[11] Tie Jun Cui, Mei Qing Qi, Xiang Wan, Jie Zhao, and Qiang Cheng. Coding metamaterials, digital metamaterials and programmable metamaterials. *Light: science & applications*, 3(10):e218–e218, **2014**.

[12] Jeffrey G Andrews, François Baccelli, and Radha Krishna Ganti. A tractable approach to coverage and rate in cellular networks. *IEEE Transactions on communications*, 59(11):3122–3134, **2011**.

[13] Yassine Hmamouche, Mustapha Benjillali, Samir Saoudi, Halim Yanikomeroglu, and Marco Di Renzo. New trends in stochastic geometry for wireless networks: A tutorial and survey. *Proceedings of the IEEE*, **2021**.

[14] Tianyang Bai and Robert W Heath. Coverage and rate analysis for millimeter-wave cellular networks. *IEEE Transactions on Wireless Communications*, 14(2):1100–1114, **2014**.

[15] Mustafa A Kishk and Mohamed-Slim Alouini. Exploiting randomly located blockages for large-scale deployment of intelligent surfaces. *IEEE Journal on Selected Areas in Communications*, 39(4):1043–1056, **2020**.

[16] Saeed Bagherinejad, Mahdi Bayanifar, Milad Sattari Maleki, and Behrouz Maham. Coverage probability of ris-assisted mmwave cellular networks under blockages: A stochastic geometric approach. *Physical Communication*, page 101740, **2022**.

[17] Ericsson mobility report november 2021. `https://www.ericsson.com/en/reports-and-papers/mobility-report/reports/november-2021`. Accessed: 2022-15-05.

[18] Zhengquan Zhang, Yue Xiao, Zheng Ma, Ming Xiao, Zhiguo Ding, Xianfu Lei, George K Karagiannidis, and Pingzhi Fan. 6g wireless networks: Vision, requirements, architecture, and key technologies. *IEEE Vehicular Technology Magazine*, 14(3):28–41, **2019**.

[19] Mansoor Shafi, Andreas F Molisch, Peter J Smith, Thomas Haustein, Peiying Zhu, Prasan De Silva, Fredrik Tufvesson, Anass Benjebbour, and Gerhard Wunder. 5g: A tutorial overview of standards, trials, challenges, deployment, and practice. *IEEE journal on selected areas in communications*, 35(6):1201–1221, **2017**.

[20] Wonil Roh, Ji-Yun Seol, Jeongho Park, Byunghwan Lee, Jaekon Lee, Yungsoo Kim, Jaeweon Cho, Kyungwhoon Cheun, and Farshid Aryanfar. Millimeter-wave beamforming as an enabling technology for 5g cellular communications:

Theoretical feasibility and prototype results. *IEEE communications magazine*, 52(2):106–113, **2014**.

[21] Anass Benjebbour, Masashi Iwabuchi, Yoshihisa Kishiyama, Wang Guangjian, Liang Gu, Yang Cui, and Terufumi Takada. Outdoor experimental trials of long range mobile communications using 39 ghz. In *2018 IEEE 87th Vehicular Technology Conference (VTC Spring)*, pages 1–5. IEEE, **2018**.

[22] Marco Di Renzo, Alessio Zappone, Merouane Debbah, Mohamed-Slim Alouini, Chau Yuen, Julien De Rosny, and Sergei Tretyakov. Smart radio environments empowered by reconfigurable intelligent surfaces: How it works, state of research, and the road ahead. *IEEE Journal on Selected Areas in Communications*, 38(11):2450–2525, **2020**.

[23] Faisal Tariq, Muhammad RA Khandaker, Kai-Kit Wong, Muhammad A Imran, Mehdi Bennis, and Merouane Debbah. A speculative study on 6g. *IEEE Wireless Communications*, 27(4):118–125, **2020**.

[24] Ian F Akyildiz, Chong Han, and Shuai Nie. Combating the distance problem in the millimeter wave and terahertz frequency bands. *IEEE Communications Magazine*, 56(6):102–108, **2018**.

[25] Jeffrey G Andrews, Tianyang Bai, Mandar N Kulkarni, Ahmed Alkhateeb, Abhishek K Gupta, and Robert W Heath. Modeling and analyzing millimeter wave cellular systems. *IEEE Transactions on Communications*, 65(1):403–430, **2016**.

[26] Shihao Ju and Theodore S Rappaport. 140 ghz urban microcell propagation measurements for spatial consistency modeling. In *ICC 2021-IEEE International Conference on Communications*, pages 1–6. IEEE, **2021**.

[27] Jinfeng Du, Dmitry Chizhik, Reinaldo A Valenzuela, Rodolfo Feick, Guillermo Castro, Mauricio Rodriguez, Tingjun Chen, Manav Kohli, and Gil Zussman. Directional measurements in urban street canyons from macro rooftop sites at 28 ghz for 90% outdoor coverage. *IEEE Transactions on Antennas and Propagation*, 69(6):3459–3469, **2020**.

[28] Yunchou Xing and Theodore S Rappaport. Millimeter wave and terahertz urban microcell propagation measurements and models. *IEEE Communications Letters*, 25(12):3755–3759, **2021**.

[29] Mathew K Samimi, George R MacCartney, Shu Sun, and Theodore S Rappaport. 28 ghz millimeter-wave ultrawideband small-scale fading models in wireless channels. In *2016 IEEE 83rd Vehicular Technology Conference (VTC Spring)*, pages 1–6. IEEE, **2016**.

[30] Ertugrul Basar, Marco Di Renzo, Julien De Rosny, Merouane Debbah, Mohamed-Slim Alouini, and Rui Zhang. Wireless communications through reconfigurable intelligent surfaces. *IEEE access*, 7:116753–116773, **2019**.

[31] Nanfang Yu, Patrice Genevet, Mikhail A Kats, Francesco Aieta, Jean-Philippe Tetienne, Federico Capasso, and Zeno Gaburro. Light propagation with phase discontinuities: generalized laws of reflection and refraction. *science*, 334(6054):333–337, **2011**.

[32] Dan Zhao, Hancheng Lu, Yazheng Wang, Huan Sun, and Yongqiang Gui. Joint power allocation and user association optimization for irs-assisted mmwave systems. *IEEE Transactions on Wireless Communications*, **2021**.

[33] Qi Gu, Dan Wu, Xin Su, Jing Jin, Yifei Yuan, and Jiangzhou Wang. Performance comparisons between reconfigurable intelligent surface and full/half-duplex relays. In *2021 IEEE 94th Vehicular Technology Conference (VTC2021-Fall)*, pages 01–06. IEEE, **2021**.

[34] Changsheng You, Beixiong Zheng, and Rui Zhang. Intelligent reflecting surface with discrete phase shifts: Channel estimation and passive beamforming. In *ICC 2020-2020 IEEE International Conference on Communications (ICC)*, pages 1–6. IEEE, **2020**.

[35] Qingqing Wu and Rui Zhang. Intelligent reflecting surface enhanced wireless network via joint active and passive beamforming. *IEEE Transactions on Wireless Communications*, 18(11):5394–5409, **2019**.

[36] Jian Wang, Jeng-Yuan Yang, Irfan M Fazal, Nisar Ahmed, Yan Yan, Hao Huang, Yongxiong Ren, Yang Yue, Samuel Dolinar, Moshe Tur, et al. Terabit free-space data transmission employing orbital angular momentum multiplexing. *Nature photonics*, 6(7):488–496, **2012**.

[37] Wankai Tang, Ming Zheng Chen, Xiangyu Chen, Jun Yan Dai, Yu Han, Marco Di Renzo, Yong Zeng, Shi Jin, Qiang Cheng, and Tie Jun Cui. Wireless communications with reconfigurable intelligent surface: Path loss modeling and experimental measurement. *IEEE Transactions on Wireless Communications*, 20(1):421–439, **2020**.

[38] Qingqing Wu, Shuowen Zhang, Beixiong Zheng, Changsheng You, and Rui Zhang. Intelligent reflecting surface-aided wireless communications: A tutorial. *IEEE Transactions on Communications*, 69(5):3313–3351, **2021**.

[39] Venkat Arun and Hari Balakrishnan. Rfocus: Practical beamforming for small devices. *arXiv preprint arXiv:1905.05130*, **2019**.

[40] Taniya Shafique, Hina Tabassum, and Ekram Hossain. Stochastic geometry analysis of irs-assisted downlink cellular networks. *IEEE Transactions on Communications*, 70(2):1442–1456, **2022**.

[41] Gourab Ghatak, Vikrant Malik, Sanket S Kalamkar, and Abhishek K Gupta. Where to deploy reconfigurable intelligent surfaces in the presence of blockages? In *2021 IEEE 32nd Annual International Symposium on Personal, Indoor and Mobile Radio Communications (PIMRC)*, pages 1419–1424. IEEE, **2021**.

[42] Mahyar Nemati, Jihong Park, and Jinho Choi. Ris-assisted coverage enhancement in millimeter-wave cellular networks. *IEEE Access*, 8:188171–188185, **2020**.

[43] Tianwei Hou, Yuanwei Liu, Zhengyu Song, Xin Sun, Yue Chen, and Lajos Hanzo. Mimo assisted networks relying on intelligent reflective surfaces: A stochastic geometry based analysis. *IEEE Transactions on Vehicular Technology*, 71(1):571–582, **2021**.

[44] Jiangbin Lyu and Rui Zhang. Hybrid active/passive wireless network aided by intelligent reflecting surface: System modeling and performance analysis. *IEEE Transactions on Wireless Communications*, 20(11):7196–7212, **2021**.

[45] Tianyang Bai, Rahul Vaze, and Robert W Heath. Analysis of blockage effects on urban cellular networks. *IEEE Transactions on Wireless Communications*, 13(9):5070–5083, **2014**.

[46] Özgecan Özdogan, Emil Björnson, and Erik G Larsson. Intelligent reflecting surfaces: Physics, propagation, and pathloss modeling. *IEEE Wireless Communications Letters*, 9(5):581–585, **2019**.

[47] Marco Di Renzo, Merouane Debbah, Dinh-Thuy Phan-Huy, Alessio Zappone, Mohamed-Slim Alouini, Chau Yuen, Vincenzo Sciancalepore, George C Alexandropoulos, Jakob Hoydis, Haris Gacanin, et al. Smart radio environments empowered by reconfigurable ai meta-surfaces: An idea whose time has come. *EURASIP Journal on Wireless Communications and Networking*, 2019(1):1–20, **2019**.

[48] Zheng Shi, Hong Wang, Yaru Fu, Guanghua Yang, Shaodan Ma, and Feifei Gao. Outage analysis of reconfigurable intelligent surface aided mimo communications with statistical csi. *IEEE Transactions on Wireless Communications*, **2021**.

[49] Qin Tao, Junwei Wang, and Caijun Zhong. Performance analysis of intelligent reflecting surface aided communication systems. *IEEE Communications Letters*, 24(11):2464–2468, **2020**.

[50] Liang Yang, Fanxu Meng, Jiayi Zhang, Mazen O Hasna, and Marco Di Renzo. On the performance of ris-assisted dual-hop uav communication systems. *IEEE Transactions on Vehicular Technology*, 69(9):10385–10390, **2020**.

[51] Jacqueline Bertrand, Pierre Bertrand, and Jean-Philippe Ovarlez. The mellin transform, **1995**.

[52] F Oberhettinger. Tables of mellin transforms springer-verlag berlin heidelberg new york. **1974**.